2016

SURFACE-INITIATED POLYMERIZATIONS FOR THE RAPID SORTING OF RARE CANCER CELLS

Jacob L. Lilly
University of Kentucky, jllilly19@gmail.com
Digital Object Identifier: http://dx.doi.org/10.13023/ETD.2016.270

STUDENT AGREEMENT:

I represent that my thesis or dissertation and abstract are my original work. Proper attribution has been given to all outside sources. I understand that I am solely responsible for obtaining any needed copyright permissions. I have obtained needed written permission statement(s) from the owner(s) of each third-party copyrighted matter to be included in my work, allowing electronic distribution (if such use is not permitted by the fair use doctrine) which will be submitted to UKnowledge as Additional File.

I hereby grant to The University of Kentucky and its agents the irrevocable, non-exclusive, and royalty-free license to archive and make accessible my work in whole or in part in all forms of media, now or hereafter known. I agree that the document mentioned above may be made available immediately for worldwide access unless an embargo applies.

I retain all other ownership rights to the copyright of my work. I also retain the right to use in future works (such as articles or books) all or part of my work. I understand that I am free to register the copyright to my work.

REVIEW, APPROVAL AND ACCEPTANCE

The document mentioned above has been reviewed and accepted by the student's advisor, on behalf of the advisory committee, and by the Director of Graduate Studies (DGS), on behalf of the program; we verify that this is the final, approved version of the student's thesis including all changes required by the advisory committee. The undersigned agree to abide by the statements above.

Jacob L. Lilly, Student

Dr. Brad Berron, Major Professor

Dr. Tom Dziubla, Director of Graduate Studies

SURFACE-INITIATED POLYMERIZATIONS FOR THE RAPID SORTING OF RARE CANCER CELLS

DISSERTATION

A dissertation submitted in partial fulfillment of the
Requirements for the degree of Doctor of Philosophy in the
College of Engineering at the
University of Kentucky

By

Jacob Louis Lilly

Lexington, Kentucky

Director: Dr. Brad J. Berron, Assistant Professor of Chemical Engineering

Lexington, Kentucky

2016

ABSTRACT OF DISSERTATION

SURFACE-INITIATED POLYMERIZATION FOR THE RAPID SORTING OF RARE CANCER CELLS

Cancer metastasis directly accounts for an estimated 90% of all cancer related deaths and is correlated with the presence of malignant tumor cells in systemic circulation. This observed relationship has prompted efforts to develop a fluid biopsy, with the goal of detecting these rare cells in patient peripheral blood as surrogate markers for metastatic disease as a partial replacement or supplement to invasive tissue biopsies. Numerous platforms have been designed, yet these have generally failed to support a reliable fluid biopsy assay due to poor performance parameters such as low throughput, low purity of enriched antigen positive cells, and insufficiently low detection thresholds to detect poor expressed surface markers of target cell populations. This work describes the development of a rapid cell sorting technology called Antigen Specific Lysis (ASL) based on photo-crosslinked polymer film encapsulation to isolate tumor cells in suspension.

In the first study, we characterize the chemical and structural properties of the surface-initiated polymer films formed directly on mammalian cell surfaces. Coated cell populations are shown to remain highly viable after coating formation. Biomolecular transport is examined though film coatings on cellular substrates using fluorescent, time-resolved confocal microscopy and diffusivity estimates are generated for these materials. In the next study, a lysis-based cell isolation platform is described in which marker positive cells can be specifically coated in a heterogeneous cell suspension. Anionic surfactants lyse virtually 100% of uncoated cells while fully encapsulated cells remain protected, and are then easily collected by centrifugation. We report that purified cells are released from polymeric coatings to yield viable and functional populations. We monitor cell response throughout the isolation process by multiple techniques, and report cell viability >80% after the sorting process. Lastly, we examine the response of process yield on the level of photoinitiator loading on target cell populations. Streptavidin-fluorochrome loading was quantitatively assessed on a panel of markers, both epithelial and mesenchymal, on representative model breast and lung cancer cells. We report that ASL is fundamentally capable of achieving 50-60% yield which is promising for fluid biopsy applications. Finally, both EpCAM and metastatic targeting strategies are then compared to covalently biotinylated samples to inform future robust targeting strategies.

KEYWORDS: cancer, cell sorting, photopolymerization, thin films, surface coatings, cell encapsulation

Jacob L. Lilly
Student Signature

April 29, 2016
Date

SURFACE-INITIATED POLYMERIZATIONS FOR THE RAPID SORTING OF RARE CANCER CELLS

By

Jacob Louis Lilly

Dr. Brad Berron
Director of Dissertation

Dr. Tom Dziubla
Director of Graduate Studies

April 29, 2016
Date

DEDICATION

To My Family

ACKNOWLEDGEMENTS

There are so many people that have helped me greatly along my path that I wish to thank. First and foremost, I would like to thank my parents for their support and guidance. They showed me at a young age the meaning and reward of hard work and to never settle for mediocrity. I would also like to thank my sister, Kristin, and my cousin, Dr. Lindsay Dillingham, for both setting an example of perseverance toward your goals even when things seemed impossibly difficult.

I would also like to thank in particular Molly Eickholt for putting up with me and always being there to listen, advise, encourage, and console. I could have not made it to this point without her love and supporting words, either in person or just a phone call away.

I of course wish to thank my advisor, Dr. Brad Berron, for his patience and enthusiasm for science, which allowed me to develop both confidence and passion in the field. I would like to thank my labmates Weijie, Leila, Ishan, Calvin, Paige, Landon, Naveed, Nate, and Katie for their assistance and friendship in the lab. Dr. Gabriela Romero in particular was instrumental in my learning and progress in research. All of these people contributed to establishing a lab culture that was productive yet highly enjoyable for which I am immeasurably grateful.

I'd like to acknowledge everyone involved with the Cancer Nanotechnology Training Center for financial support but also for the advice and experience I gained through that program, which was transformative for my education here at UK. Particularly, I'd like to thank Dr. Edward Hirschowitz for his inspiration and instruction in the field of metastatic cancer and Dr. Hainsworth Shin for the helpful and frequent advice in flow cytometry.

Finally, there are countless others outside of research that have made my time in graduate school enjoyable. I'd like to acknowledge Molly Eickholt, Dan Schlipf, Anastasia Kruse, Carolyn Jordan, Nathanael Stocke, Chris Millisor, Stephanie Pagano, Angela Gutiérrez, Jason Absher, Rob Wensing, Alfred Cotton, Nicole Staricek, Alicia Juncoz, along with many others. Thanks for all the good times outside of lab that kept me sane and made my time at UK a tremendously fun experience.

Table of Contents

List of Tables

List of Figures

Chapter 1: Introduction

Tumor metastasis plays a central role in the often fatal nature of cancer, and directly accounts for an estimated 90% of all cancer related deaths [3, 4]. Although the exact signaling cues and underlying mechanisms that drive the metastatic process remain an area of intense research, the link between metastasis and the presence of circulating tumor cells (CTCs) in peripheral blood has long been observed. Many have reported that the detection of high numbers of CTCs in cancer patients is correlated with poorer prognosis, particularly in breast, prostate and colorectal cancer types [5-9].

These findings have prompted much effort in developing technologies to detect, isolate, and characterize these CTCs in patient peripheral blood samples for clinical use as a "fluid biopsy", with the hope of establishing a reliable prognostic indicator. Ideally, this isolation modality could be implemented in a treatment regimen as a supplement or partial replacement for a traditional tissue biopsy. This would allow almost continual supervision of progression and response to treatment, while minimizing the trauma and bodily stress of a tissue biopsy. For decades, strategies have focused on simple enumeration of the rare epithelial-like cell in the bloodstream, and have shown limited success as a reliable, predictive assay. Critically, the poor performance in both sensitivity and specificity of CTC isolation strategies has prevented their incorporation into standard therapy practices and has not led to measurable improvements in clinical outcomes [10]. This has been due, in part, to the reliance of these isolation technologies on detecting cells based on the definitive epithelial marker, EpCAM, and the assumption that the tumor cell phenotype is static and unalterable [11-13]. Emerging evidence suggests there exists vastly complex biochemical signaling between tumor cells and their evolving

microenvironment that provoke and sustain metastasis [14]. This heterotypic signaling causes a certain subset of tumor primary cells to shed their epithelial phenotype and gain more stem-like properties that allow them to be particularly well suited for the subsequent phases of metastasis – migration, invasion, intravasation, circulation, and extravasation [1].

This process, known as epithelial-mesenchymal-transition (EMT), has been shown to causes a reversible and dynamic shift in the tumor cell phenotype as epithelial markers are downregulated, suggesting that CTC detection strategies based on recognition of epithelial markers may not "see" a large proportion of these highly metastatic stem-like CTCs [4, 15, 16]. We submit that mesenchymal cells represent significant false negative events in current detection approaches, contributing to poor assay sensitivity, specificity, and ultimately utility. Further, while this phenomenon has been well described in vitro and at the tumor primary, little is known about the marker expression profile of a CTC during transit in the bloodstream largely because currently available CTC isolation technologies are incapable of isolating these populations with the purity and quantity needed for analysis.

This dissertation focuses on the development of polymer thin film cell coatings to rapidly sort marker-positive cancer cells via lysis based negative depletion of all marker-negative cells. Here, we demonstrate that primary antibodies bind specifically to cancer cell surface markers, which through subsequent biotin/avidin interactions then direct the site-specific binding of visible-spectrum photoinitiator species. Irradiation in the presence of monomer and coinitiator is shown to crosslink a nanothin film around marker-positive cells that specifically protects and stabilizes these cells during surfactant lysis. Chapter 2

presents a more detailed background of cancer biology relevant to circulating tumor cells, and an overview of the current technologies designed to isolate and detect these rare cells. In Chapter 3, a background of the polymer materials is introduced as well as the specific photochemistry reactions utilized in this work. In chapters 4 through 7, the main projects of this work are presented. First, the chemical, structural, and selective permeability properties of our thin film materials on cell substrates are investigated. Next, a UV-photodegradable functionality is designed to allow for release of target cells after isolation, and sorting from heterogeneous cell suspensions confirms the specificity of our method. Due to the variability often seen in cancer phenotypes, we then offer a quantitative and comparative analysis of a panel of markers implicated in metastasis. Commonly studied breast and lung cancer lines are examined to provide reference and guidance as to the quantity, and moreover density, of cancer markers available for targeting. Lastly, we relate photoinitiator binding density to the yield of cells delivered and determine a loading threshold for isolation.

1.1 Specific Objectives

The overall objective of this work was to design and implement surface-initiated polymer coatings for protective isolation during lysis-based negative depletion. The specific objectives of the four experimental chapters presented in this dissertation are shown below:

1. Characterization of Molecular Transport in Ultrathin Hydrogel Coatings on Cellular Substrates for Engineered Selective Permeability
    a. Demonstrate successful and specific cell surface film coating
    b. Analyze and describe the chemical and structural properties of polymer coatings
    c. Investigate the cell toxicity effects of coating formation
    d. Develop Fickian model and determine macromolecular diffusivity within PEGDA film coatings
2. Design and Development of Protective Polymer Coatings for Rapid High-Purity Cancer Cell Isolation
    a. Synthesize UV-degradable macromers and confirm structure
    b. Demonstrate marker specific cell sorting in binary mixtures
    c. Determine sorted cell purity after ASL sorting
    d. Determine cell viability and capacity for proliferation of sorted populations
3. Quantitative Investigation of Surface Receptor Expression Density For The Isolation of Tumor Cells
    a. Identify cancer-associated markers implicated in metastasis for analysis

b. Describe non-small lung cancer and breast cancer cell morphology and calculate diameter.

c. Determine specific fluorescent probe loading for all marker targeting scenarios on cancer lines and normal human peripheral blood cells

d. Calculate loading densities for all marker targeting scenarios

4. The Role of Surface Receptor Density in Surface-Initiated Polymerizations for Cancer Cell Isolation

    a. Determine effect on isolated cell yield of incrementally varied photoinitiator loading on A549 cells covalently tagged with sulfo-NHS-biotin

    b. Compare isolation yield of covalent biotinylation to populations targeted via primary antibodies binding epithelial and stem markers

    c. Investigate gelation response in analogous protein microarrays

    d. Determine lower threshold photoinitiator loading density required for protective coating isolation

Chapter 2: Relationship of CTC Isolation Technologies to Metastatic Cancer Biology

2.1 Introduction

Recent evidence suggests a subpopulation of primary tumor cells acquire stem-like properties that permit the dissemination from the primary into the surrounding stroma and sets the stage for metastatic spread. In contrast, current CTC isolation methodologies are based on detecting cells based on the antigenic profiles found in the original primary, which are largely epithelial. This disconnect highlights the need for a greater appreciation of the biological drivers of metastasis in designing CTC detection technologies. This chapter focuses on metastatic cancer biology that determines CTC phenotype and provides perspective in light of the currently available CTC isolation technologies.

2.2 Role of Epithelial-Mesenchymal Transitions in Metastatic Cancer

Numerous studies have reported epithelial-mesenchymal transitions are a facilitator and driver of metastatic activity [17]. Recently, several underlying signaling networks have been revealed to be extremely intricate, and eventually generate a heterogeneous composition of cell phenotypes in the stromal environment and at distant metastases. Further, EMT is highly active at both the primary invasive front and during blood bourne metastasis where intervening treatment is perhaps most crucial for disease management [1, 18]. These findings have highlighted the need for greater appreciation of the biology in designing cell isolation methodology.

During tumor formation in a primary carcinoma, oncogenic changes in epithelial cells lead to excessive proliferation, as well as angiogenesis and cell recruitment to fuel

rapid growth [19]. During this initial stage of tumorigenesis, the malignant cells are thought to retain much of their epithelial characteristics, including cell-cell junctions, apical-basal polarity, and lack of motility [14]. However, as recruitment cytokines emanate from the primary, the stromal environment begins to evolve and diversify with the accumulation of support cells such as mesenchymal stem cells, endothelial progenitors, and macrophages [20, 21]. This complex signaling landscape is believed to play a prominent role in sparking aggressive and robust EMT programs in a certain subset of primary cells that drive the subsequent stages of cancer progression [22]. Growth factors exchanged at the tumor-stroma interface such as PDGF, EGF, HGF, and TGF-β have been shown to initiate pathways that induce transcription factors implicated in EMT [1, 23, 24]. Notably, induction of Snail, Slug, ZEB1/2, Twist, and the Wnt/β-catenin pathway previously associated with wound healing and embryogenesis models have all more recently been implicated in this cancer progression process [25, 26]. Epithelial surface proteins, particularly those involved in attachment to ECM are cell-junctions, are downregulated such E-cadherin, αβ-integrins, and EpCAM [27]. The marker E-cadherin especially has been widely studied in this context, and the functional loss of this epithelial marker has become a hallmark of the EMT program. Accompanying the repression of attachment proteins, mesenchymal traits begin to appear such as restructuring of the cytoskeleton to favor a more motile and invasive cell, as well as enhanced resistance to apoptosis, and loss of polarity [28]. Other stem-like molecular features also appear such as matrix metalloprotease and N-cadherin expression that allows for degradation of ECM and basement membranes and increased capacity for migration necessary to enter the vasculature [27].

Not surprisingly, evidence shows these stem-like tumor cells are highly enriched at the invasive front of many primary carcinomas as depicted in **Figure 2.1**. Further, these cells may even lead the way for intravasation of many other tumor cell phenotypes arising from the same primary that otherwise may not have had the required invasive attributes to accomplish the feat on their own [26, 29].

While we hypothesize that the mesenchymal transitioned tumor cells are the most relevant and potent for disease progression, this could perhaps reconcile the observed link between the detection of epithelial-like cells in circulation of metastatic patients and poor prognosis in several current CTC isolation technologies. Largely, once tumor cells spill into the bloodstream, little is known about the exact mechanisms that determine their phenotype while in free circulation. Some evidence supports that a CTC is never truly autonomous, but EMT signaling in the primary does stabilize the mesenchymal state for transit such that it constitutively remains until signals favoring an epithelial phenotype reverses the cell back to a more epithelial state, ostensibly at a secondary and distant site (i.e. metastatic focus) [15, 30]. Further complicating the characterization of these stem-like CTCs, the Stott group recently managed to collect a small number of CTCs from several metastatic breast cancer patients, and immunostained for both epithelial and mesenchymal markers. The results suggest these cells as highly variable from patient to patient, and even shows variable phenotypes within the same peripheral blood sample [31]. Many cells expressed significant levels of both epithelial and mesenchymal markers, suggesting an EMT phenotype in reality falls more on a continuum between the two extremes. Collectively, these findings relating EMT to surface expression on CTCs point toward the need for an isolation methodology capable of yielding viable and

functional cells for further analysis to elucidate the mechanisms that shift or sustain CTC phenotypes.

2.3 Current CTC Isolation Technologies

Given the significant progress made in revealing the underlying biological drivers governing metastasis, the isolation technology community has been compelled to reassess the fundamental bases and performance characteristics that will be needed to deliver a reliable CTC sorting approach [32-35]. While some groups have had moderate success is isolating CTCs based on physical properties such as size and membrane rigidity [36], the most promising approaches by far have isolated CTCs based on recognition of surface antigens. However, translating these for clinical use has remained challenging due to poor sensitivity and biological specificity, largely because they target epithelial antigens. Moreover, many assay protocols require fixation and often take an entire day of processing, which precludes further functional analysis of these multipotent EMT cells [9]. In the following sections, the current most common isolation methodologies will be detailed, with context given to the particular challenges of metastatic tumor cell targeting.

2.3.1 Magnetic-Activated Cell Sorting

Magnetically-activated cell sorting, or MACS, relies on tagging antigen-positive populations with magnetic particles by standard immunolabeling protocols [37]. Antibodies are conjugated to magnetic particles and incubated with a cell mixture where they bind to a particular surface marker of interest [38]. Magnetic sorting can achieve its highest throughput in a semi-batch mode, where after immunolabeling a cell mixture is passed through a magnetized disposable column. The sensitized antigen positive cells are retained by the column with varying affinity while all other cell populations not

sensitized by immunomagnetic labeling pass through the column readily and are discarded. The magnetic field is removed, and through subsequent rinsing steps the antigen-positive cells are removed and collected from the column [39]. The main advantages of MACS is in its high throughput capabilities and little sterilization requirements because the column is typically single-use. In evaluating the efficacy of MACS in circulating tumor cell detection applications, even advanced MACS systems only achieve ~50-75% purity [34], which is insufficient given the extreme rarity at which CTCs exist in circulation (~1 per million).

2.3.2 Fluorescence-Activated Cell Sorting

Fluorescence-activated cell sorting (FACS) has existed as a concept for cell analysis for several decades and is based on labeling antigen-positive cells with fluorophores conjugated to antibodies. Flow cytometry is used to measure the cell fluorescence due to antibody binding, size, and granularity, and thresholding is imposed to collect target cells based on marker expression [40]. Purities attained by FACS are often greater than 99%, but because microfluidics are used to hydrodynamically focus individual cells during sorting, this high purity comes at the cost of extremely slow sorting rates [41, 42]. Additionally, FACS has the capability of analyzing several fluorescent signals simultaneously with multiple-laser configurations, representing a key advantage in analyzing complex protein interactions. Flow sorters are also prohibitively costly (~$500,000) to many laboratories, and require lengthy sterilization procedures to flush contaminates from fluidic lines, and peristaltic pumps need to be routinely calibrated to ensure measurement accuracy. In all, due to its reliance on microfluidics,

FACS inherently cannot provide rapid and cost effective sorting for large-scale CTC detection and isolation.

2.3.3 CellSearch System

To date, only one CTC isolation technology is clinically validated by the FDA called CellSearch, designed by Veridex (Raritan, NJ), which involves enrichment with immunomagnetic beads against EpCAM followed by immunofluorescent labeling and analysis to further confirm the epithelial phenotype (DAPI+, CK+, CD45-) of the enriched population. Staining with DAPI ensures the detected event is a nucleated cell, while staining for cytoplasmic cytokeratins is a secondary measure for an epithelial cell. Finally, positive detection also requires the cell event to be negative for the leukocyte-common antigen CD45. Using this definition of a CTC, it was established that a count of ≥5 of cells per 7.5ml peripheral blood that met the thresholding criteria correlated with a statistically significant drop in prognosis in breast, prostate, and colon cancers [8, 9]. CellSearch systems have been the most commonly employed CTC isolation and enumeration methods, however have not incorporated into standard treatment regimens because of widely reported low sensitivity resulting in considerable false negatives in metastatic patients as well as low purity of isolated cells. As detailed above, it is suspected that the poor performance of CellSearch is due to variability in antigen expression from EMT processes, such that the most metastatic cells have little to no epithelial expression and therefore go unnoticed as false negatives when employing the CellSearch platform [4, 12]. Further, the FDA validated CellSearch protocol requires fixation and permeabilization of the cell samples, which presumably improves consistency and reproducibility, yet does not yield viable and functional cells post-

processing. We hypothesize that the isolation of biologically functional CTCs for downstream characterizations is critical for linking the observed EMT processes with the ultimate fate of a CTC, and for developing a fluid biopsy approach with greater prognostic capacity.

2.3.4 Microfluidic Approaches

More recently, groups have worked toward designing CTC isolation methods capable of delivering viable cells that use microfluidic channels to separate and capture CTCs [35]. For metastatic breast cancer, cell suspensions are flowed into microfluidic devices containing reservoirs that feature arrays of micro-posts covalently functionalized with antibodies cocktails – typically a combination of EpCAM, HER2, and EGFR [43-45]. These antigen-selective methods have exhibited moderate purity and capture efficiency. Later generations of these devices have begun to appreciate the dynamic and seemingly unpredictable nature of CTC phenotypes, and take a more unbiased and agnostic approach to enrichment by negatively depleting CD45+ cells by magnetic separation in microfluidic channels to yield cells unmolested by sorting methodology [46]. While these creative approaches have yielded intriguing results that will undoubtedly instruct future generations of isolation technology, they suffer critically from low throughput at approximately 3 mL processed per hour [45]. Microfluidic channels inherently introduce high levels of shear forces that prevent the increase of fluid flow rates to practical levels, and require the need for careful optimization so fluid shear does not exceed the electrostatic force of antibody capture. These constraints ultimately result in an assay that would require a day or more to isolate a population of CTCs sufficient for immediate characterization.

2.4 Conclusions and Perspectives

Here, the biology of cancer metastasis has been discussed, as well as the limitations of current CTC isolation approaches. In the context of sorting rare stem-like populations, these cells purportedly exist in a dedifferentiated state that can respond to a multitude of lineage-specific, directing stimuli [47]. Therefore, we submit that not only does a CTC sorting method need to yield functional cells, perform with high specificity and purity, but also be a high-throughput and rapid technique to successfully isolate these stem-like populations for analysis.

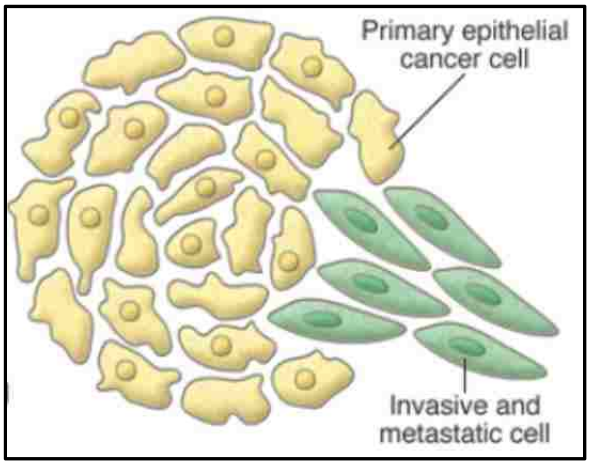

Figure 2.1: Schematic depicting invasion of mesenchymal-transitioned cells leaving the primary tumor site. From Kalluri & Weinberg (2009) [1].

Chapter 3: Hydrogel Polymerization Approaches to Cellular Encapsulation and Surface Modification

3.1 Introduction

In the past several decades, the use of synthetically derived polymeric materials has revolutionized the field of medicine, particularly for targeted therapy and tissue regeneration. Hydrogel polymers allow remarkable versatility; they can be tailored to possess a wide array of functional characteristics that make them well suited as a medium in biomedical settings [48, 49]. This chapter will focus on the polymerization of hydrogels as a scaffold for cell encapsulation. First, the chemical and structural characteristics of hydrogels will be introduced in the context of cell encapsulation. Microencapsulation strategies will be discussed with perspective on the effect of encapsulation environment on permeability and mass transfer to the cell surface. Next, photoinitiated free radical polymerization will be examined as a route to hydrogel formation, with particular emphasis on the eosin Y photoinitiation system, which is used throughout this dissertation. Lastly, we will examine surface initiated polymer-based amplification as a method to form nanometer-scale hydrogel films specifically at sites of protein expression.

3.2 Hydrogel Properties

Synthetic hydrogels have long been studied for the protection of biological species *in vivo* [50]. Hydrogels for cell encapsulation are typically covalently crosslinked [51]. The most definitive property of hydrogels is the ability to absorb water and swell and remain stable and water-insoluble, often to several fold greater sizes that the dehydrated states [52]. This swelling occurs due to hydrogen bonding and electrostatic

interactions between water and the crosslinked structure, such that water is thermodynamically favored to infiltrate the porous material. In applications in aqueous cell media settings, oxygenated water and other small molecules can readily permeate to and from the cell surface while the cell itself stays protected and occluded for large molecular structures. This allows cells to remain encapsulated for long periods of time while retaining high viability [53, 54].

One particularly advantageous capability is the polymerization of hydrogel materials directly around cells from a monomeric precursor solution. This allows one to carefully tune and tailor the properties of the eventual 3D material. Scaffold geometry and material thickness is an important design consideration and can be modified depending on the polymerization method employed. Mechanical properties can also be tuned with the monomer chemical composition and concentration. Crosslinked hydrogels consist of a porous mesh structure with void space between crosslinks, which allows for significant movement and flexing under mechanical strain. Many groups have shown that the mechanical performance of hydrogel is predictably controlled to mimic that of biologically derived tissue depending on the monomer, crosslinking density, and molecular weight between crosslinks (MWBC) [55-57]. Hydrogels can been designed to resemble a variety of complex tissues at a wide range of length scales from extracellular matrices, to individual cells, to whole organs [58, 59].

These parameters (monomer concentration, crosslinking density, MWBC, mesh size) are also significant determinants of the permeability of hydrogel scaffolds. For homogenously crosslinked hydrogels, smaller MWBC and mesh size or higher crosslinking density will generally result in lower permeability [60-62]. Tailoring the

selective permeability of hydrogel encapsulation environments is critical for many applications. Selectivity based on sized can prevent large macromolecules such as host antibodies and immune cells from penetrating the hydrogel architecture while allowing smaller growth factors to freely penetrate. Cruise et al. has shown in bulk crosslinked PEG-diacrylate membranes that PEG-diacrylate with MWBC of 2kDa, vitamin B12 (1.2 kDa) was able to permeate the material while globular proteins such as myoglobin (16.7kDa) and larger showed no detectable diffusion [60]. Membranes composed of 20kDa PEG-diacrylate, however, readily allowed both vitamin B12 and myoglobin, showing the effect of MWBC on the membrane permeability. Reinhart et al. developed a model for swollen polyvinyl alcohol hydrogels that relates solute diffusivity to these structural parameters for several biomolecular permeants, which further suggests the direct positive correlation between MWBC and diffusivity [63, 64]. Increasing the cross-linking density, by either increasing the monomeric concentration in solution, longer polymerization reaction times, or increased reaction kinetics, can also reduce the permeability of hydrogel membranes. More complete crosslinking (i.e. unreacted pendant monomer ends) reduces the mobility and access of solutes as they navigate through the material via passive diffusion.

3.3 Hydrogel Chemical Composition

Many monomer chemistries have been explored for hydrogel cell encapsulation and are selected with consideration to each particular application [65]. Both naturally-derived and synthetic polymers have been investigated. Naturally-derived hydrogel materials typically offer innate compatibility with the encapsulated cells of interest as they are often derived from ECM scaffolds that would surround these cells

physiologically. They include materials composed of collagen, gelatin, fibrin, and chitosan typically covalently modified with vinyl moieties to allow for radical polymerization [66]. While these materials have shown successful application in tissue engineering to encapsulate chondrocytes [67], cardiomyocytes [68], and mesenchymal stem cells [69] among many others, they are often impractical to utilize due to their heterogeneous and complex nature. Gelation kinetics, mechanical performance, and diffusivity are often difficult to predict and control for these materials. Alternatively, synthetic monomeric compounds are typically more monodisperse and predictable and offer high control over gelation rates and consistent mechanical performance. Synthetic materials that have been utilized for cell encapsulation include polyethylene glycol (PEG), polycaprolactone (PCL), polyvinyl alcohol (PVA), poly lactic acid (PLA), and poly lactic-co-glycolic acid (PLGA) [70]. Of these, PEG has been by far the most widely investigated material for encapsulation. PEG macromers are typically functionalized with acrylate groups to enable radical polymerization in solution, and are typically water soluble. PEG hydrogels also show high structural and chemical stability [71]. While the ester bond within acrylate backbones of PEG hydrogels is susceptible to hydrolytic degradation, this occurs at very slow rates. Further, PEG has been widely shown to be biocompatible *in vivo* and exhibit low encapsulated cell toxicity [53]. Many acrylated PEG macromers with excellent monodispersity are also commercially available, providing a convenient medium with which to design and scale up many cell encapsulation technologies with predictable gelation kinetics and mechanical properties.

3.4 Microencapsulation and Hydrogel Geometry Effects on Mass Transfer

While macroscale cell-laden hydrogel scaffolds have advanced numerous applications in tissue engineering and regenerative medicine , many researchers have recognized the potential advantages of microengineered hydrogel architectures in certain applications [51, 72-74]. Microencapsulation is the strategy to coat individual cells or small groups of cells with porous scaffold material with thicknesses typically a few hundred micron or less. Minimizing the coating thickness, and thus the diffusion length, would improve the transport of low-molecular weight nutrients and cellular waste components while still preventing large immune molecules from reaching the cell surface. Because of the increased surface area to hydrogel volume ratio, the overall mass flow rate can increase per cell. In the field of islet encapsulation for insulin therapy, Canaple et al. showed an improvement in diffusion leading to increased long term viability and cellular function for islets encapsulated in 400 μm thick coatings as compared to 1000 μm [75]. Further, for coatings designed to be degradable (enzymatically or photocleavage), the volume of material to be degraded is minimized.

Several methodologies have been investigated for hydrogel cell microencapsulation. Mumaw et al. encapsulated small groups of mesenchymal stem cells in PEG-diacrylate (10kDa) by oil-aqueous phase microemulsion and subsequent UV-range photopolymerization for bone grafting therapy [76]. Microcapsules were approximately 100 μm in diameter, and showed high long term viability and cell proliferation. Photolithographic techniques can also be useful in forming microstructures with high spatial resolution. Koh et al. showed PEG microstructures could be patterned down to 50 μm containing as few as one 3T3 murine fibroblast per structure [77]. Flow

microfluidics and combined lithographic techniques have also been explored that can generate well defined and gradient microencapsulation geometric shape on the order of tens to hundreds of microns in thickness [78, 79]. Cruise et al. showed the capability of encapsulating individual porcine islets with visible-light photopolymerization of PEG-diacrylate coatings after soaking cells in eosin Y (type II photoinitiator) solution [54, 80]. This technique allowed for thicknesses down to a few hundred microns, and showed long term cell survival and insulin secretion *in vivo* after xenograft transplantation.

3.5 Approaches to Photoinitiated Polymerization of Hydrogels

One of the most commonly employed methods of forming hydrogels for cell encapsulation is through radical photopolymerization. This method offers many practical advantages for hydrogel formation over other types of polymerization. Photopolymerization allows for rapid and predictable gelation from an aqueous monomer precursor solution at room temperature, often at buffered, pH balanced conditions [81, 82]. Initiating light can typically be delivered uniformly throughout hydrogel systems creating highly homogenous materials. Further, by controlling where and when light is exposed, one has excellent spatial and temporal control over the reaction, allowing for complex material geometries or crosslinking gradients to be engineered into hydrogel systems if desired. Both visible and UV spectrum range photoinitiated systems have been described, where light sensitive compounds are excited to generate radicals to crosslink the hydrogels from the precursor solution. Water-soluble monomer units are often vinyl or acrylate functionalized, enabling this free radical polymerization process [70]. In the following sections, two types of photoinitiator compounds (type-I and type-II) will be introduced that have been utilized for hydrogel formation.

3.5.1 Type-I Photoinitiators

Type-I photoinitiation involves the photoinduced cleavage of initiators to produce free radical reaction products, which then propagate crosslinking of monomers in solution. While these polymerizations are complex reactive processes, a typical mechanism can be written for type-I photopolymerization as shown in **Scheme 3.1**.

During the initial phase of the polymerization, the reaction rate and double bond conversion increase as radicals are generated at a rate such that reaction dominates the process and monomer crosslinking propagates. Once the gel point is reached, diffusion begins to control the process as radical mobility is decreased leading to termination of radicals as nearby monomer ends react. These photocleavage type initiators are commonly employed in dental resins and simple tissue engineering scaffolds, where rapid gelation and homogenous crosslinking is desired [2]. Widely employed type-I photoinitiators for polymerization include the acetophenone and hydroxyalkylphenones chemical families, mostly sensitized with irradiation light below 400 nm [70]. One particular concern for hydrogel cell encapsulation is water solubility and cell cytotoxicity. Because these compounds are mostly comprised of alkyl groups and aromatic rings, they typically display limited water solubility making implementation in cellular systems difficult. Of type-I photoinitiators, lithium acylphosphinate (LAP), 2-hydroxy-1-[4-(hydroxyethoxy)phenyl]-2-methyl-1-propanone (Irgacure 2959), 2,2-dimethoxy-2-phenylacetophenone (Irgacure 651), and 1-hydroxycyclohexyl-1-phenyl ketone (Irgacure 184) have commonly been employed for hydrogel formation [81, 83]. Williams et al. formed cell-laden hydrogel systems with the listed Irgacure compounds in a comparative toxicity study and showed that all were generally significantly cytotoxic, with Irgacure

2959 showing moderate cell compatibility for a limited number of cell lines [84]. Another practical concern is that these compounds are generally unable to achieve regeneration after cleavage and must be used at relatively high concentrations, hindering their application to coating individual cell surfaces by interfacial polymerization.

3.5.2 Type-II Photoinitiators

In type-II polymerization, often referred to as dye photosensitizer systems, photosensitive compounds absorb irradiation light energy, enter an excited state and abstract a hydrogen molecule from a nearby donor coinitiator which then initiates crosslinking of monomer acrylic groups. **Scheme 3.2** shows a typical reaction mechanism for this process:

While this system requires a more complex two-component initiation step, the propagation and termination steps occur similarly as to type-I systems. Common type-II photoinitiators include benzophenone, camphorquinone, xanthene derivatives, and thioxanthones [70, 85, 86]. For cell encapsulation, hydrogen donor coinitiators have typically been tertiary amines. Several xanthene derivatives absorb in visible range, affording the use of more cell compatibility lamp outputs than the typical UV range lamps [83]. Of these, eosin Y and fluorescein have been commonly investigated as type-II initiators and absorb around 450-550 nm [87]. The eosin system in particular shows sufficiently fast gelation and excellent cytocompatibility for cell encapsulation utilized in tandem with tertiary amine coinitiators [80].

3.5.3 Eosin Y Photoinitiation System

As this dissertation utilizes primarily eosin Y as a type-II photoinitiator, this section will expound on the previous work with this specific system. Eosin Y has been

used with a tertiary amine coinitiator triethanolamine (TEA) to form crosslinked hydrogel networks in aqueous media [88-90]. In our studies, an isothiocyanate group is coupled to eosin to form eosin-5-isothiocyanate (EITC), which negligibly affects the absorbance properties. A plot of extinction coefficient dependency on wavelength for EITC is shown in **Figure 3.1**. In eosin/TEA systems, eosin is irradiated by visible green light typically in the range of 500-550 nm, corresponding to the shown range of absorptivity. Eosin molecules are excited to a triplet state, which is quenched by the tertiary amine TEA which acts as a hydrogen donor. Proton transfer occurs, which yields a protonated eosin radical and a neutral α-aminoalkyl radical. This amine radical then acts to initiate polymerization of nearby carbon double bonds [87, 91].

Encinas et al. has demonstrated the rate of eosin/TEA system in the polymerization of acrylamide in water is largely unaffected by pH changes in the range of 3 to 10 [87]. Further, this work showed the efficiency of photoinitiation at 20mM TEA of approximately 45-55% of triplets quenched to form active amine radicals, which is well correlated with trends in the initial polymerization rates of other xanthene dyes. Avens et al. presented evidence of a cyclic photoinitiator regeneration mechanism that enables eosin to overcome high concentrations of polymerization inhibitors in the reaction environment, whereas the cleavage-type photoinitiator Irgacure-2959 was completely inhibited in this setting [86]. These data suggested many dye photosensitizer systems benefit from cyclic regeneration to achieve overall improved polymerization efficiency. Kizilel et al. demonstrated the eosin/TEA system in surface-mediated polymerization, where eosin molecules where covalently functionalized on glass substrates, and surface grafted thin films of PEG-diacrylate were analyzed both chemically and visually by

microscopy [85]. Here, as commonly employed with similar systems, 1-vinyl-2-pyrrolidinone is included in the monomer formulation as a polymerization accelerator. The performance and significant parameters of the surface-mediated eosin system was also investigated by Avens et al. for both PEG-diacrylate and acrylamide formulations [92]. At eosin functionalization densities greater than 200 molecules/μm^2, the acrylamide system generated films >600 μm and the PEG-diacrylate system generated films of approximately 150 μm. It should be noted that acrylamides have shown to be highly toxic in cell environments whereas PEG-diacrylate is generally non-toxic. This work also showed the phenomenon of a lower photoinitiator surface density threshold for this interfacial system, below which radical generation was no sufficient to crosslink any detectable film.

3.6 Surface-Mediated vs. Bulk Polymerized Hydrogels

Differences arise between bulk and surface-mediated polymerization settings in both design considerations and the eventual hydrogel structure. A bulk crosslinked system refers to polymerizations in which photoinitiator is dissolved and distributed indiscriminately throughout the precursor solution, and upon irradiation the polymerization reaction proceeds uniformly throughout the gelling material irrespective of location. In surface-mediated or interfacial polymerization, photoinitiator molecules are adsorbed to a surface or interface, and remain localized at this surface throughout the reaction. Type-II photosensitizers are often employed in applications for surface-mediated hydrogel systems and can leverage cyclic regeneration and achieve appreciable polymerization efficiencies, whereas cleavage-type compounds can only generate an amount of radicals on the same order as the initially adsorbed surface density of

molecules. Competing diffusive-reactive phenomena play a large role in the overall polymerization performance of surface-mediated systems, as coinitiator molecules in the immediate vicinity of the photoreactive surface are radicalized [93]. These free radicals are able to diffuse away from the reactive surface, so radical generation must be sufficient to overcome diffusion of radicals to reach the gel point for a continuously interlinked polymer network to form. While bulk crosslinked systems typically display homogenous crosslinking density, this phenomenon in surface-mediated systems leads to a gradient, with crosslinking density decreasing at increasing distance from the reactive surface as shown in **Figure 3.2**. As the gel point is first reached near the photoinitiator-primed surface, radical mobility falls significantly and leads to overall decreasing free radical concentration a further outward distances, leading to the gradient in crosslinking density. This is an important consideration in hydrogel structure design, particularly in applications where permeability is a critical parameter as the hydrogel mesh size cannot be assumed to be constant through the entire material.

3.7 Polymer-Based Amplification

The work in this dissertation leverages the efficiency of the eosin photopolymerization system to generate polymer thin films specifically at sites of protein recognition by adapting the recently described technology of polymer-based amplification (PBA), as shown in **Figure 3.3** [94]. PBA was developed as an inexpensive diagnostic platform to generate an easily detectable signal prompted by recognition of biomolecules at extremely low concentrations on printed microarrays. Other signal amplification approaches such as tyramide-signal amplification are highly sensitive to variations in enzyme activity and preparation conditions that often lead to inconsistent

results and high nonspecific signal. In contrast, PBA has shown to generate predictable signal responses with high signal-to-noise [95]. Specific antibodies or anti-sequence oligonucleotides are contacted with microarrays printed with analyte solution. Photoinitiators, typically eosin or fluorescein, are covalently labeled directly on these molecules or on secondary biorecognition molecules that bind to analyte. Photopolymerization is then initiated in the presence of acrylic monomer and tertiary amine coinitiator to generate a crosslinked polymer response at sites of analyte presentation. PBA has been shown to generate polymer films in response to as low as zeptomolar analyte concentrations in seconds to minutes [96]. Applications have been developed that utilize initiating visible range light from broad spectrum mercury lamps, collimated LEDs, and lasers. Monomer formulations studied for use in PBA include acrylamide/bisacrylamide and polyethylene glycol diacrylate, both including 1-vinyl-2-pyrrolidinone as an accelerator [92]. Because this reaction has been shown to be inhibited by oxygen, printed chips or slides are typically purged with inert gas (nitrogen or argon) during photopolymerization to remove oxygen from the reacting system. For visualization of analyte recognition, polymer films are either colorimetrically stained post-polymerization or loaded fluorescent imaging nanoparticles that are physically entangled in the film crosslinking during initial photopolymerization. Notably, the signal intensity of loaded fluorescent nanoparticles has been shown to trend linearly with film thickness in PBA applications [97].

PBA has been adapted as a diagnostic platform to detect several types of analytes. Hansen et al. (2007) showed a PEG diacrylate film response to detect a short oligonucleotide sequences [98]. Hansen et al. (2009) then progressed DNA detection with

the specific detection of *KRAS* sequence variants [99]. Antibody based detection has also been investigated, where biotin-α-goat IgG is printed on glass array chips [95]. Eosin-labeled streptavidin then bonds to sites of biotin functionalization and initiates fluorescent PBA with visible light and monomer. Here, fluorescent PBA is shown to achieve 100-fold greater signal-to-noise than samples stained with traditional fluorescent probe approaches. Fluorescent PBA has also been previously demonstrated for enhanced histochemical staining on fixed mammalian cells [100]. Nuclear pore complex, vimentin, and von-Willebrand factor proteins are targeted with primary antibodies in permeabilized lung fibroblasts, which direct streptavidin-eosin binding and fluorescent PEG-diacrylate film formation. PBA is shown to provide enhanced signal-to-noise immunostaining compared to parallel stained samples with streptavidin-FITC and tyramide signal amplification approaches.

3.8 Conclusions

Hydrogels offer a cell compatible material for covalent microencapsulation. By dispersing cells in a monomer precursor solution, hydrogel can be formed by photopolymerization *in situ* around individual cells. Further, by tuning the molecular weight of monomeric units and crosslinking conditions, hydrogel materials can be engineered to act as size selective, semi-permeable membranes that occlude large biomolecules while allowing free passage of small compounds. Lastly, eosin-mediated polymer-based amplification provides an efficient and convenient approach to forming nanothin films specifically at sites of surface protein expression.

$$I \rightarrow 2R\bullet$$

$$R\bullet + M \rightarrow M\bullet$$

$$M_n\bullet + M \rightarrow M_{n+1}\bullet$$

$$M_n\bullet + M_m\bullet \rightarrow P$$

Scheme 3.1: General mechanism for Type-1 (photocleavage) polymerization. Adapted from Ifkovits & Burdick, 2007 [2].

$$I \rightarrow I^*$$

$$I^* + R \rightarrow I^{+}\bullet + R\bullet$$

$$R\bullet + M \rightarrow M\bullet$$

$$M_n\bullet + M \rightarrow M_{n+1}\bullet$$

$$M_n\bullet + M_m\bullet \rightarrow P$$

Scheme 3.2: General mechanism for Type-II photopolymerization.

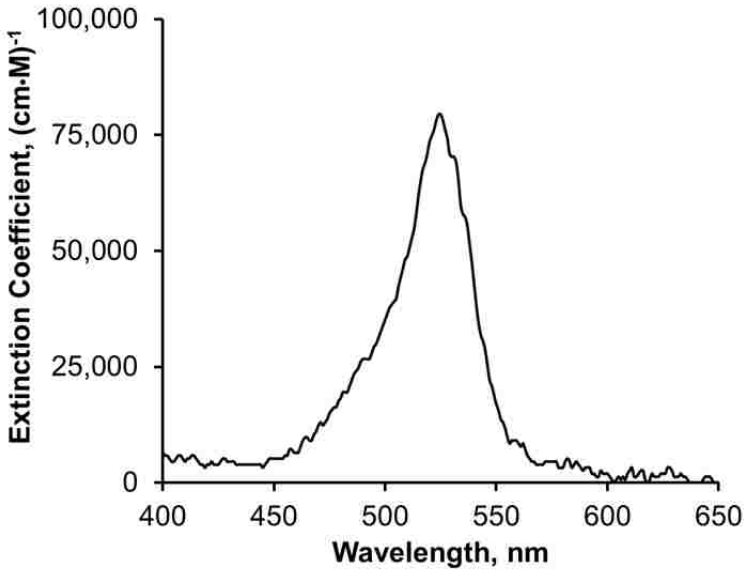

Figure 3.1: Plot of extinction coefficient dependency on wavelength of eosin isothiocyanate in water. Calculated from UV-Vis absorbance spectra.

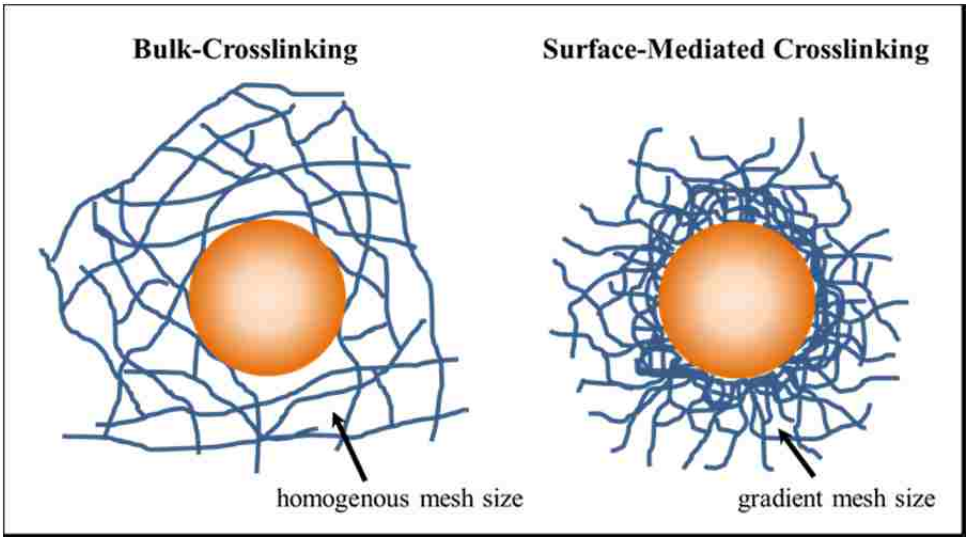

Figure 3.2: Comparison of crosslinking density and mesh size for bulk and surface-mediated polymerization schemes.

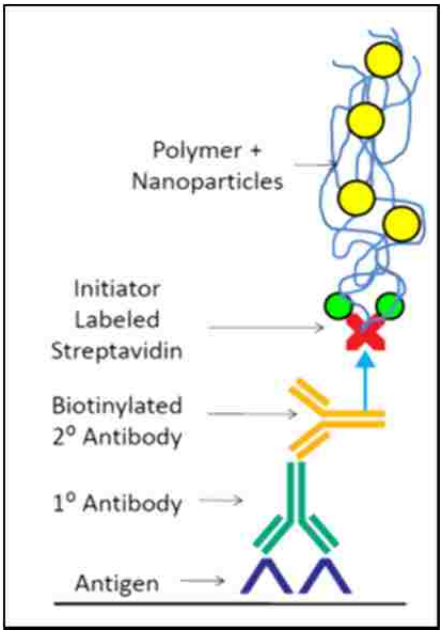

Figure 3.3: General schematic of fluorescent polymer-based amplification.

Chapter 4: Characterization of Molecular Transport in Ultrathin Hydrogel Coatings on Cellular Substrates for Engineered Selective Permeability

This work studies a surface-initiated, nanoscale hydrogel coating on mammalian cells for tunable, size-selective permeability. Coatings composed of PEG diacrylate of molecular weight 575 Da and 3500 Da were studied by tracking the transport of fluorescently-labeled dextrans across the coatings. The molecular weight of dextran at which the transport is blocked by these coatings are consistent with cutoff values in analogous bulk PEG materials. Additionally, the diffusion constants of 4 kDa dextrans across PEG 575 coatings was lower than across PEG 3500 coatings and these trends and magnitudes agree with bulk scale models. Further, this study supports the adaptability of this coating strategy for a lysis-based isolation methodology, where antigen presenting cells are coated with ultra-thin films which impart protection during exposure to SDS micelles. The data suggest these hydrogel coatings will be fundamentally capable of excluding SDS micelles that are several orders of magnitude larger than the dextran molecules shown to be excluded. The chapter presented here is adapted with minor modifications from work previously published:

> Jacob L. Lilly, Gabriela Romero, Wejie Xu, Hainsworth Y. Shin, Brad J. Berron. Characterization of Molecular Transport in Ultrathin Hydrogel Coatings for Cellular Immunoprotection. Biomacromolecules. 27;16(2):541-9, 2015.

4.1 Introduction

Synthetic hydrogels have long been studied for the protection of biological species [53, 66]. Hydrogel architectures have been designed for use in applications ranging from drug delivery particles and scaffolds to large tissue grafts for implantation

[101-103]. For cell replacement therapies, exogenous cells have been encapsulated in hydrogels to physically prevent the host's antibodies from recognizing the foreign cells while allowing the free transport of water and nutrients throughout the porous mesh [50, 70]. This strikes a careful balance between the transport of the unwanted high molecular weight materials and the beneficial low molecular weight materials. The size selectivity of the hydrogel is a property of the polymer mesh structure, where large molecular weight materials do not penetrate appreciably into the hydrogel.

We seek to encapsulate mammalian cells in suspension by the photopolymerization of ultra-thin hydrogel films for designed semi-permeable barriers to prevent large molecules from reaching the encapsulated cell surface. Our approach is based on surface-mediated polymerization of nanoscale films (**Figure 4.1**), where photoinitiator is grafted to the outside of a cell in extremely low concentrations [95]. In these conditions, the photoinitiator content is reaction limiting, and the subsequent growth of polymer is restricted to a thin film at the cell surface [104]. Upon introduction of a monomer precursor solution containing triethanolamine (coinitiator), the initiator-primed cells are exposed to green light, and a free-radical, interfacial polymerization process results [85]. We expect this technique will be capable of completely coating cells for size selective control of materials to the cell surface. Prior calculations on 100 μm and 1 mm thick analogues of these materials describe a mesh size of 2-5 nm which prohibits IgG diffusion, yet readily permits diffusion of low MW materials [60, 105]. Critically, the diffusion properties of these ultra-thin films on cells have yet to be measured.

This chapter directly studies the chemical, physical, and transport properties of nanoscale hydrogel films on a cellular surface. For experimental simplicity, we examined

coatings on the surface of Jurkat cells, an immortalized, robust, and easily cultured T lymphoma cancer cell line. The chemistry of the coatings was directly analyzed with Raman microscopy showing shifts consistent with the localization of PEG coatings on the cell's surface. The coatings were imaged by scanning electron microscopy, supporting a surface morphology distinct from native cells and consistent with control samples of surface-initiated polymer thin films.

While structure and chemical characterizations provide valuable insight to the film properties, the most definitive measure of an encapsulation technique is the capability to exclude large biomolecules from penetrating the coating while allowing the free transport of low molecular weight nutrients to retain high viability. Extrapolation of transport properties of a bulk hydrogel to thin film geometries is commonplace, yet fundamentally assumes identical and uniform cross-linking in the film [60]. For the surface-mediated, free radical polymerizations employed here, a gradient of double bond conversion arises during the photoreaction yielding a film with non-uniform microstructure [93]. To this end, we measured these transport properties directly on a coated cellular substrate for measurement of film properties directly on biological supports without any extrapolation of bulk transport properties. Our findings support the current practice of extrapolating bulk hydrogel transport properties to nanoscale coatings, where minimal differences were observed between our diffusion constants and those of the analogous bulk materials. These findings support the potential use of ultra-thin coatings, such as those presented here, for tunable, size-selective membranes effectively halting transport of large molecular weight materials above the critical values observed in bulk hydrogel systems.

4.2. Materials and Methods

4.2.1 Materials

A Jurkat cell line (clone E6.1) was purchased from ATCC. RPMI-1640 with L-glutamine and Dulbecco's Modified Eagle's Medium were both purchased from Corning Cellgro, and supplemented with fetal bovine serum (Gibco) and Streptomycin/Penicillin solution (Thermo Scientific). Deionized and ultra-filtered water was purchased from Fisher Scientific. Eosin-5-isothiocyanate, poly(ethylene glycol) diacrylate (M_n=575), 1-vinyl-2-pyrrolidinone, poly-L-lysine (PLL), bovine serum albumin, HEPES-KOH buffer solution, potassium acetate, magnesium acetate, and fluorescein isothiocyanate-dextran (FD) with MW of 4, 10, and 20kDa were purchased from Sigma-Aldrich. Poly(ethylene glycol) diacrylate was passed over a MEHQ removal column twice prior to use. Phosphate buffered saline 10X solution, nile red carboxyl-terminated 20 nm Fluosphere nanoparticles (NPs), and calcein AM were purchased from Life Technologies. Biotinylated monoclonal mouse IgG anti-human CD45 was from BD Pharminogen, monoclonal mouse IgG anti-human nuclear pore complex was from Covance, biotinylated goat IgG anti-mouse IgG was purchased from Vector Labs. Lyophilized streptavidin, biotinylated bovine serum albumin and 4',6-diamidino-2-phenylindole (DAPI) were purchased from Thermo Scientific. Poly(ethylene glycol) diacrylate (M_n = 3500) was purchased from Jenkem Technology. Triethanolamine and Triton X-100 were purchased from Acros. Paraformaldehyde (16%, EM grade) was purchased from Electron Microscopy Sciences. Sucrose was obtained from MP Biomedical. Calcein/ethidium homodimer-1 Cytotoxicity kit was purchased from Life Technologies.

4.2.2 Preparation of Polymer Encapsulated Cells in Suspension

The T lymphoma Jurkat cell lineage was cultured in RPMI-1640 supplemented with 10% fetal bovine serum (FBS) and 1% streptomycin/penicillin at 37 °C and 5% CO_2. The cell culture was maintained at approximately 0.5-1x10^6 cells/ml. A sample of 1.5 x 10^6 Jurkats was washed once with phosphate buffered saline (PBS) supplemented with 3% FBS (PBS/FBS). Between each rinsing step, the cells were pelleted by centrifugation at 300x*g* and 4°C for 5 minutes. The pellet was resuspended in 20 μL biotinylated mouse anti-human CD45 in 100 μL PBS/FBS per 10^6 cells, gently vortexed and incubated at 4°C for 40 minutes. Then, the pellet was resuspended in 25 μg/mL streptavidin-eosin isothiocyanate (SA-EITC) in PBS/FBS, gently vortexed and incubated for 30 minutes at 4°C. The SA-EITC was synthesized and purified according to a previously reported protocol [98]. After incubation and rinsing with PBS/FBS, the cells were dispersed in 300 μL of a monomer precursor solution consisting of 420 mM poly(ethylene glycol) diacrylate (M_n = 575) (PEGDA 575), 21 mM triethanolamine (TEA), 35 mM 1-vinyl-2-pyrrolidinone (VP) in PBS. In fluorescent imaging studies, 0.05 wt % nile red 20 nanometer fluorescent NPs were also included in the precursor solution. Just before introduction to cells, the monomer solution was bubbled with ultra-pure N_2 for approximately 5 minutes to remove oxygen (polymerization inhibitor). The monomer/cell solution was gently vortexed and then pipetted onto a standard microscope slide in a Chip-clip chamber well (Whatman). The Chip-clip was then placed in a clear plastic bag and purged with ultra-pure N_2 for 5 minutes. Then, a photopolymerization reaction was initiated with an LED lamp emitting collimated 530 nm light, adjusted to an intensity of 30 mW/cm^2 for 10 minutes. (See **Appendix A-1** for example of general

photopolymerization setup) The Chip-clip was then removed from the purged bag and the cells were removed from the slide with a shearing stream of PBS and washed two times to remove any unreacted monomer solution species and free nanoparticles.

4.2.3 Raman Microscopy Analysis

To probe the surface chemistry of coated cells, first a PEGDA coated Jurkat cell sample was prepared as described, except that Jurkats were fixed in 1% paraformaldehyde for 10 minutes and rinsed three times in PBS, and then incubated in PBS + 3% FBS for 30 minutes before primary antibody incubation. After rinsing the coated cells, the supernatant was removed and the cell pellet was pipetted onto a clean microscope slide and allowed to dry for 2 h. For a native cell control, 10^6 cells were centrifuged and rinsed once with cold PBS and then fixed in 1% paraformaldehyde for 10 minutes. The cells were then rinsed 3 times in cold PBS. After the final rinse, the supernatant was removed and the pellet was gently pipetted onto a clean microscope slide. A bulk polymer control was prepared by first reacting 25 μg/mL SA-EITC in PBS on an epoxy-functionalized slide inserted in to a Chip-Clip for 1 hour. After rinsing, 300 μL of monomer solution was pipetted into the Chip-Clip well. The Chip-Clip slide was purged and irradiated with an LED lamp for 10 minutes, emitting 530 nm light at an intensity of 30 mW/cm^2. The slide was then washed with deionized water and allowed to dry overnight. The samples were analyzed using a Thermo Scientific DXR Raman microscope. The 532 nm laser and 100X objective were used for all spectral measurements. The pinhole aperture was set to 25 μm, corresponding to a focal spot of approximately 1 μm diameter. Spectra were recorded between 300 and 3600 cm^{-1} at a 5 cm^{-1} spectral resolution. The system was calibrated to the spectral line of crystalline

silicon at 520.7 cm^{-1}. For a spectral measurement, the microscope was focused on the surface of a sample and at least 8 scans at each spot were used to reduce the spectral noise.

4.2.4 Scanning Electron Microscopy

For SEM analyses, a control Jurkat sample was fixed in 1% paraformaldehyde for 10 minutes, rinsed twice in PBS, and placed on a PLL coated microscopy slide for electrostatic attachment. A coated sample was prepared with paraformaldehyde fixed cells, as before. Samples were dried overnight before analysis. The sample slides were then coated in gold/platinum by standard techniques and micrographs were taken with a Hitachi S-4300 scanning electron microscope (Hitachi, Japan). The working distance was set at 15 mm with an accelerating voltage of 5.0 kV.

4.2.5 Viability Assays

Cellular viability was measured by a calcein assay. Cells were rinsed once with PBS, then the cell pellet was resuspended in cold PBS 1X with 50 nM calcein AM and incubated at room temperature protected from light for 15 minutes. After incubation, the cells were loaded into a BD Accuri C6 flow cytometer (Becton Dickinson), and run was performed at a medium fluidics rate to a total event count of 100,000.

4.2.6 Surface-Initiated Polymer Microarrays

Epoxy-functionalized microscopy slides 25 x 75 mm (CEL-1) were rinsed once with ethanol and dried with ultra-pure N_2. Serial dilutions of biotinylated bovine serum albumin (bBSA) from 0.11 to 1000 μg/mL were prepared in PBS plus one negative control with 0 mg/mL bBSA (12 solutions total). bBSA solutions were then loaded into a 96 well plate and printed on the epoxy slides with an Affymetrix 417 Arrayer and

allowed to dry overnight. Two replicate spots were printed for each biotin concentration in an array, as shown in **Appendix A-4**. A biotin-functionalized slide was loaded into a Whatman Chip-Clip, rinsed once with PBS supplemented with 0.1% BSA (PBSA) for 2 minutes, and then incubated with PBSA for 1 hr. After blocking, a 25 μg/mL SA-EITC solution in PBSA was incubated in the array well for 30 minutes. The slide was then rinsed once with PBSA for 2 minutes, then twice with PBS for 2 minutes each. For this study, three polymerization conditions were investigated that mimicked live cell encapsulation (Condition 1) and conditions used to coat fibroblast nuclei (Conditions 2 & 3). For live cell encapsulation, the monomer solution (1) consisted of: 420 mM PEGDA 575, 21 mM TEA, 35 mM VP, 0.05 wt% nile red NPs in PBS. For PEGDA-575 thin films around nuclei (2), the monomer solution was: 420 mM PEGDA 575, 210 mM TEA, 35 mM VP, 0.05 wt% nile red NPs in deionized water. For PEGDA 3500 thin films (3): 25 wt% PEGDA-3500, 210 mM TEA, 35 mM VP, 0.05 wt% nile red NPs in deionized water. Before polymerization, the solution was bubbled for 5 mins with ultra-pure N_2. After rinsing a slide, 300 μL of the corresponding monomer solution was pipetted into the Chip-Clip array well, and placed in a clear plastic bag and purged with N_2 for 5 minutes. The photoinitiation conditions were as follows: (1) 530 nm, 30 mW/cm^2, 10 minutes; (2) 530 nm, 10.5 mW/cm^2, 20 minutes; (3) 530 nm, 10.5 mW/cm^2, 20 minutes. After photopolymerization, the slides were rinsed twice with deionized water before imaging. After drying overnight, profilometry measurements were performed on each array set with a Dektak 6M profilometer to prevent scratching of the film, scan settings were maintained at 4200 micron for 120 s, with a stylus force of 1 mg.

4.2.7 Preparation of Encapsulated Subcellular Species by Polymer-Based Amplification

Human dermal fibroblasts were cultured to ~80% confluency in DMEM supplemented with 10% FBS and 1% penicillin/streptomycin at 37 °C and 5% CO_2. Cells were trypsinized, centrifuged, and seeded onto 35 mm cover glass-bottom culture dishes (Mat-tek) in media. For encapsulation of nuclei, a recently published protocol was adapted [104]. Cell dishes were washed twice with cold PBS, and then fixed with 1% paraformaldehyde in PBS for 10 minutes. Cells were then washed 3 more times with cold PBS. The fixed cells were then permeabilized with 0.01% Triton X-100 in PBS for 7 minutes, and washed 3 times with PBS. A blocking solution consisting of 2 mL of PBSA with 2% FBS was pipetted into the dishes and incubated for 30 minutes at 4°C. Cells were then immersed in a primary antibody solution of 1:1000 monoclonal mouse IgG anti-human NPC in PBSA for 40 minutes at 4°C, followed by a secondary antibody incubation of 1:400 biotinylated goat IgG anti-mouse IgG in PBSA for 40 minutes at 4°C. Cells were rinsed 3 times with PBSA, and then incubated with SA-EITC (25 μg/mL) in PBSA for 30 min at 4°C. The cells were then washed 2 times with PBS and once with deionized water. Two monomer solutions were prepared for polymer films of PEGDA-575 (420 mM PEGDA-575, 210 mM TEA, 35 mM VP, 0.05 wt% nile red NPs in deionized water) and PEGDA-3500 (25 wt% PEGDA-3500, 210 mM TEA, 35 mM VP, 0.05 wt% nile red NPs in deionized water). For each monomer molecular weight, 915 μL of monomer solution was pipetted into a petri dish, and placed in a nitrogen-purged bag as before. An LED lamp emitting green light (530 nm, 10.5 mW/cm^2) was placed over

the dish and the reaction was allowed to proceed for 20 minutes. The dishes were then washed 3 times with deionized water.

4.2.8 Time-Dependent Confocal Microscopy Analysis of Diffusion

To probe macromolecular permeation through films formed by polymer-based amplification, varying sizes of FITC-labeled dextrans (FD) (4kDa, 10kDa, 20kDa) were prepared in transport buffer adapted from Mohr et al, consisting of 20mM HEPES-KOH pH 7.4, 120 mM potassium acetate, 5mM magnesium acetate, and 250mM sucrose [106]. Solutions of 10 kDa and 20 kDa FD were prepared at 15 μM, however, the 4 kDa FD required a higher concentration of 45 μM for quantifiable fluorescence signal. Human dermal fibroblast cell samples were washed twice with transport buffer. Diffusion kinetics were analyzed with a Leica AOBS/TCS SP5 confocal microscope (Leica Microsystems, Wetzlar, Germany) equipped with a HyD photon-counting hybrid detector. A 63x oil objective and an argon laser were used at 30% power. Just before a confocal diffusion study, transport buffer was removed from a glass bottom petri dish and it was loaded onto the microscope stage. The focus was adjusted and centered (z-direction) inside a coated nucleus. An automated timed scan was initiated, with an image taken every 1.5 seconds. After approximately 3-4 scans, 100 μL of FD solution was pipetted directly onto the scanning region and the automated scanning program was allowed to run for at least 160 seconds. For statistical significance analysis Student's t-test was calculated for all samples and in all the cases the p value obtained was lower than 0.0001.

4.3. Results and Discussion

4.3.1 Encapsulating Live Cells in Suspension by Surface Protein Recognition

The purpose of this study was to characterize the structure and permeability of nanothin hydrogel coatings formed directly on cellular surfaces. These films are formed by interfacial polymerization by binding the type-II photoinitiator eosin to surface marker sites that enables excellent spatial control of polymer formation and ultra-thin coatings to control molecular transport. (See **Appendix A-5** for more details on protein specificity of polymer formation) Photoinitiated systems are convenient for cell encapsulation, owing to the delivery of uniform initiation energy to the system, rapid gelation, excellent viability, and the ease of scale-up to large cell populations [70, 107, 108]. For our suspension study we chose the T lymphoma Jurkat cell line because it is a robust immortalized lineage with a high growth rate and abundant expression of CD45, an antigen that is well understood and commonly targeted. The experimentally optimized conditions of 21 mM TEA, a 10 minute reaction time, and an initiation light intensity of 30 mW/cm^2 was used to encapsulate Jurkats with a crosslinked PEGDA film, shown in **Figure 4.2**. To monitor film formation by microscopy and flow cytometry, fluorescent NPs (nile red, 20nm, Fluospheres) were also introduced in the monomer mixture, and have been shown to be physically entangled in the surface-initiated films in a similar system [97]. High cell viability was preserved near 90% approximately 1 hour after encapsulation, as measured by a flow cytometric calcein assay (**Figure 4.3**). Further, cytometry experiments of coated cells showing low ethidium homodimer-1 fluorescence compared to dead controls also suggest high viability of Jurkats through the coating process. While longer time points are critical to the ultimate application of cell

transplantation, this level of initial viability is consistent with that of similar eosin photoinitiated PEGDA encapsulation systems with high long term cell viability [76, 80, 90].

4.3.2 Characterizing Film Surface Chemistry and Morphology

We used Raman microscopy to characterize the surface chemistry of the hydrogel coating. Spectra were collected at the surface of an uncoated Jurkat, the surface of a coated Jurkat, and at the surface of bulk cross-linked PEGDA-575 film (**Figure 4.4**). The three spectra revealed the different chemical nature at the surface of each sample. We expect the coated cells Raman spectrum to be the result of the superposition of both, native cells and polymer film spectra. The coated Jurkat spectrum shows a peak at 2850 cm^{-1} associated with the symmetric stretching of CH_2 groups from the lipid-rich cellular organelles (lipid bodies) present in native Jurkats, but also displays signals from bulk PEGDA at 2880 cm^{-1} and 2950 cm^{-1} corresponding to CH_2 and CH_3 vibrations, respectively [109]. The presence of peaks associated with both the native cell and the bulk polymer control in the polymer coated cell spectra further supports the presence of a PEG-diacrylate coating observed at the cell surface by fluorescent labeling (**Figure 4.1** and **Figure 4.2**).

Scanning electron microscopy was also used to analyze the surface morphology of a polymer coated cell. A scanning electron micrograph of a paraformaldehyde-fixed native Jurkat exhibits a smooth, flattened morphology (**Figure 4.5.a**), while a PEGDA-encapsulated, fixed Jurkat cell (**Figure 4.5.b**) possesses a similar size as the uncoated cell with a rough surface. The similarity in size between the coated and uncoated cells supports our hypothesis that thin films on the order of nanometers thick and do not

appear to alter the resulting coated cell size. The surface texture of coated cells is also different from that of an uncoated cell and appears to have a rough yet consistent topology. A magnified view of the coated cell surface (**Figure 4.5.c**) indicates a surface texture similar to that of a surface-initiated PEG-diacrylate film (**Figure 4.5.d**). While some variation in coating thickness is expected in surface mediated polymerization on the order of tens of nanometers, the surface features in **Figure 4.5.c** are more consistent with the underlying membrane folds common to Jurkats and other leukocytes [110]. Critically, SEM observation clearly supports that coatings are uniform and complete across the cell's surface, without observable gaps or apparent changes in thickness. Further, the covalent PEG crosslinking that forms these films is highly stable and to limit any opportunity for cells to shed the films in the transplantation environment [111].

4.3.3 Estimation of Film Thickness

The overall goal of this work is to determine the size-dependent transport properties of nanoscale hydrogels, and to relate them to the established bulk hydrogel transport properties. For accurate scaling of nanoscale barrier films to bulk materials, it is essential to attain an estimate of the coating thickness. The estimation of coating thickness is particularly challenging at thicknesses below direct optical observation. Measurement of coating thicknesses less than ~300 nm is typically accomplished by ellipsometry, atomic force microscopy, profilometry, or electron microscopy. When dealing with a poorly reproducible and non-uniform biological surfaces, it is difficult to obtain accurate baseline data for thickness measurement by ellipsometry, atomic force microscopy, and profilometry. Further, the solvent-dependent nature of hydrogel thickness makes any measurement in a TEM embedding medium impossible to correlate

without further understanding the solvent's influence on the hydrogel thickness. As a result, we estimated the thickness based on the fluorescent intensity of the polymer film on a biological substrate by correlation to the fluorescent intensity of an easily measured polymer film grown on a smooth glass substrate.

Biotinylated bovine serum albumin (bBSA) microarrays were prepared with biotin concentrations between 0 and 1000 μg/ml bBSA, where these surfaces were meant to replicate the chemical environment of the biotin-functionalized surface after a cell surface is labeled with biotinylated antibodies. These surfaces were treated with photopolymerization conditions that were identical to cellular coating procedures. As expected, polymer thickness increased with printed bBSA concentration, as more eosin molecules were bound to the array surface which increased radical formation during photoinitiation (**Figure 4.6**). From image analysis, it was determined that each a.u. of fluorescence intensity corresponded to 4.0 nm of thickness for the fluorescent nanoparticle loaded PEGDA-575 hydrogel coatings (**Table 4.1**). The slope is comparable for the PEGDA-3500 coatings (6.1 nm/a.u.), which suggests that the monomer size does not have a significant impact on fluorescence per polymer volume, and that the PEGDA-3500 films displayed reduced fluorescence simply because of lower polymer thickness. Using this correlation, the fluorescent signal from nanoparticle-loaded coatings on cell structures can be measured to then calculate a film thickness estimate. To obtain a thickness estimate for the coatings used later to study transport kinetics, the fluorescent signal from nanoparticle-loaded PEGDA-575 and PEGDA-3500 films encapsulating dermal fibroblast nuclei was measured by epifluorescent microscopy similarly to the microarray samples described above. To account for the signal contribution from the

upper and lower layers of the spherical nuclei, the signal was divided by two to get a representative estimate for the film coating. The thickness of PEGDA-575 and PEGDA-3500 coatings was then estimated to be 158±16 nm 200±42, respectively (**Table 4.1**). These estimates agree well with previous work with eosin-mediated growth of PEGDA thin films and are used later for mass transfer modeling of the films in this work [92, 95].

4.3.4 Assessing Permeation Across Hydrogel Thin Films

To assess the transport kinetics of nanoscale hydrogel coatings on cellular substrates, we use time dependent confocal microscopy to measure the transport of fluorescently-labeled macromolecules across hydrogel membranes. There are several advantages for studying diffusion through hydrogel coatings on adherent nuclei instead of an encapsulated whole-cell in suspension. First, using nuclei offer a substrate that is surface-anchored by cellular scaffolding without any further need for attachment factors that could potentially alter cellular geometry or bias the import kinetics. Nuclei are also much more rigidly spherical than other cellular species, including blood cells, that tend to flatten when attached to a surface, which allows for more accuracy when collecting confocal fluorescence data inside of the nucleus. Finally, the nuclear envelope can be extensively permeabilized (with Triton X-100) without complete loss of structure unlike most cell membranes, providing a scaffold for film coatings to be studied with minimal influence on diffusion kinetics.

Numerous groups have used this time-dependent confocal microscopy technique to study macromolecular permeation kinetics through nuclear pores of permeabilized cells, yet the focus has been mechanistic and on the biological cues to passive or active diffusion of different molecules [106, 112, 113]. We modify this established assay by

first forming a PEGDA thin film coating around a nucleus of a permeabilized cell with techniques described here and in prior work [104], and measuring passive diffusion of large fluorescent biomolecules through the film by sampling the fluorescence signal (i.e. concentration) inside the nucleus over time.

To establish that permeabilized fibroblast nuclei represented negligible resistance to mass transfer across the nuclear envelope, control samples were fixed and permeabilized with 0.1% Triton X-100. Solutions of fluorescein and various sizes (4, 10, and 20 kDa) of FD were prepared in transport buffer, and the accumulation of fluorescent material in nuclei was monitored by confocal microscopy (**Figure 4.7**). To account for differences in absolute fluorescence between permeants, the fluorescent signal was normalized by dividing the signal inside the nucleus by the signal outside the cell. For all of the permeants studied, diffusion was virtually immediate into the permeabilized control nuclei (>90% equilibrium concentration in nucleus at 3s).

In the uncoated permeation control study with 4 kDa FD, there is a clear affinity of the FD for nuclear material seen in **Figure 4.7.a**. The higher fluorescence of the nucleus versus the cytoplasm and surrounding regions at long timescales acts against the expected concentration gradient at the nuclear membrane and is contrary to the expected diffusive behavior. Further, the dynamics of the increase of fluorescence inside the nucleus after 40 s is linear, rather than the first order decay expected in a diffusive process. Importantly, the rate of this affinity process is less (0.2 change in relative fluorescence over 160 s) than the diffusive behavior (~1.2 change in relative fluorescence over 3 s).

PEGDA (M_n 575 and 3500) coatings incorporating red NPs were grown on the nuclear membrane by immunochemically localizing eosin to sites of nuclear pore complex expression (**Figure 4.7.b, 4.7.c**), as described previously [97, 104]. Permeant solutions were prepared as in the uncoated control experiments, and Figure 6 shows a representative images at t=3 s and t=160 s after introduction of the fluorescent permeant to the slide. For the PEGDA-575 coatings, fluorescein showed an immediate increase to a high F_{in}/F_{out} as the relatively small molecule readily permeated the film. However, the largest molecules investigated of 10 kDa and 20 kDa FD both showed essentially zero increase in F_{in}/F_{out} during the entire ~170 s experiment, suggesting that both molecules were completely excluded from the diffusing through the film. This exclusion of 10 kDa FD indicates the PEGDA-575 coatings have a polymer mesh size smaller than 3.7 nm (the hydrodynamic diameter of a 10kDa dextran) [114]. The trial of 4 kDa FD diffusion showed a F_{in}/F_{out} signal that increased, supporting that the mesh size of the PEGDA-575 film is larger than 1.3 nm (the hydrodynamic diameter of a 4kDa dextran). This 1.3 – 3.7 nm mesh size is in agreement with a previous estimate of 2.0 – 5.0 nm for bulk PEGDA-575 with the same mass fraction of monomer in water [97]. This prediction also agrees well with the unimpeded diffusion of the fluorescein dye observed in PEGDA-575 coatings, a clear demonstration of molecular weight cutoff behavior in this coating.

In diffusion trials for PEGDA-3500, we hypothesized that because the molecular weight between crosslinks was larger, the film would be more permissive to molecular diffusion. For the largest biomolecules of 10 and 20 kDa, the PEGDA-3500 film showed virtually no increase in F_{in}/F_{out} during the entire trial, demonstrating dextrans of hydrodynamic diameter of > 3.7 nm are excluded by the PEGDA-3500 coatings. The 4

kDa dextran (diameter ~1.3 nm) does permeate through the coating, indicating the PEGDA 3500 coatings also have a mesh size between 1.3 and 3.7 nm. This estimate agrees closely with the 2.2-2.7 nm mesh size reported for micron thick PEGDA-4000 coatings studied previously by Cruise, Scharp, and Hubbell [60]. To further support the molecular weight cutoff behavior of these interfacial coatings, a trial of just fluorescein showed that the film allowed instantaneous diffusion of the small molecule.

While the absolute cutoff behavior of the PEGDA-575 and PEGDA-3500 yields an identical range of mesh size, the PEGDA-3500 film permitted the diffusion of 4 kDa FD at a faster rate than PEGDA-575 (difference in Figure 6 slopes of over the first 10 s are statistically significant with $p = 1.76 \times 10^{-25}$). The faster transport across the PEGDA-3500 coating suggests a larger mesh size when compared to a PEGDA-575 coating. This fundamentally agrees with bulk scale expectations, where a larger diacrylate will yield a larger molecular weight between crosslinks, and faster diffusion than a smaller diacrylate at an identical mass fraction. It is also observed that the PEGDA-575 or PEGDA-3500 coating did not alter the apparent affinity of the 4 kDa FD for nuclear material observed in the uncoated control studies. At long time scales ($t>90$ s), there is an increase in fluorescence in the nucleus which appears linear and does not follow the expected rate decay of a diffusively driven process.

4.3.5 Estimation of Film Diffusion Coefficients

While these time-resolved images provide quantitative information about the size exclusion properties of the films, the completeness of substrate coating, and the molecular weight cut off for permeants, we also sought to extend our findings to estimate the diffusion coefficients. Because bulk photopolymerization proceeds through

drastically different initiation conditions than a typical surface-initiated system, the crosslinking profiles generated are inherently different [115]. Further, polymer diffusivities are typically measured with polymer geometries that are several micrometers thick when hydrated, which is a much larger length scale than the thin films generated in this work [60, 116]. Thus, direct measurement of diffusivities of films on cellular substrates would result in a more representative characterization of transport in the cellular microenvironment.

The diffusion constants for 4kDa FD through PEGDA coatings (D_{575} and D_{3500}) were the only analyzed, owing to clear change in nuclear fluorescence over an experimentally-accessible time scale. In addition to permeation data, a coating thickness was estimated (**Table 4.1**) using the relationship between film thickness and fluorescence summarized in **Figure 4.6**. The coating thickness for the model was further expanded to include a lower and bound approximately 50 nm above and below the calculated estimates from our microarray study of film thicknesses to account for potential error in our coating thickness estimate. Thus, a range was defined to be 100 to 200 nm for PEGDA-575 film modeling and 150 to 250 nm for PEGDA-3500 film modeling. Coating surface area and nuclear volume were calculated from confocal scans of the nucleus prior to the assay. The nonlinear fluorescence increase during the first 15 s of the polymer coated samples with 4 kDa FD appeared to be first order, and the fluorescence change in this region is used to estimate passive diffusion across the polymer coatings. In all 4 kDa FD samples, there was a consistent linear increase in nuclear fluorescence, and this non-diffusive behavior is attributed to an affinity of the dextran for the nuclear material. The contribution from 4 kDa FD nuclear affinity was estimated to be 0.03 a.u. per 15 s time

span. This contribution is <10% of the overall increase during the initial 15 s analyzed and was not included in the model. This omission potentially introduces a small error in the estimated diffusion constant, and future studies would benefit from identifying a low affinity fluorescent probe in this molecular weight range.

Using these data, Fick's Second law was numerically integrated, and diffusion constants were fit to the data for each condition. **Figure 4.8** shows plots representing a model fit for the estimated film thickness studied for each monomer length. For the lower and upper bounds of thicknesses modeled for PEGDA-575 (100-200 nm), the diffusivity of 4kDa FD through the film was calculated as $D_{575} = 9.5x10^{-10} – 2.0x10^{-9}$ cm^2/s Similarly, a diffusivity was fit to the F_{in}/F_{out} data for the PEGDA-3500 film at 150-250nm, and was calculated to be $D_{3500} = 5.9 – 9.8x10^{-9}$ cm^2/s. These findings agree with the expected higher diffusivity for the PEGDA-3500 film when compared to the PEGDA-575 film, owing to a higher molecular weight between crosslinks [117].

Remarkably, the magnitudes of the diffusion constants for these hydrogel thin films on fibroblast nuclei are consistent with that of bulk materials of similar macromer molecular weights reported in literature. The most direct literature comparison is in Cuchiara et al., where 3 and 10 kDa dextrans diffuse through PEGDA-6000 at a 10% w/v, and the diffusivities were reported to be on the order of 10^{-7} and 10^{-9} cm^2/s, respectively [116]. Further, our diffusion results also follow the expected trend of increasing diffusivity with increasing PEGDA length. Cruise et al. reported an increase in diffusivity as the molecular weight of the PEGDA monomer increased from 2kDa to 20 kDa for vitamin B-12 (~1.3kDa) permeation across the PEGDA hydrogels [60]. These diffusivities were on the order of 10^{-7} and 10^{-8} cm^2/s for the diffusion of a permeant

molecule considerably smaller than the 4 kDa FD studied here (**Figure 4.8**). This observed agreement in diffusivity between thin film and bulk polymer materials suggest that permeant diffusivity is largely decoupled from substrate encapsulation geometry. As such, we expect the permeability analysis performed here on adherent fibroblast nuclei to extend well to outer cell surfaces with minimal difference in diffusivities.

4.4 Conclusions

In this work we have demonstrated the encapsulation of both whole cell and sub-cellular species by photopolymerization of PEGDA films. By SEM and Raman microscopy we have shown that complete and conformal films are targeted to cell surfaces, and the coating surface is consistent in morphology to a surface-initiated PEG diacrylate film. This technique is applicable to both adherent and suspended cell configurations. By flow cytometric calcein assays we have shown that encapsulated cells retain viability of ~90%. Time-dependent, photon-counting CSLM analysis demonstrates that large 10- and 20 kDa fluorescein-functionalized dextran molecules are completely excluded by films formed from both PEGDA-575 and PEGDA-3500 monomers, and provides a polymer mesh size estimate of 1.3 - 3.7 nm. Microarray studies suggested these films were 100 - 200 nm in thickness, which is consistent with previously reported data on glass substrates [92]. Diffusion coefficients of 4 kDa FD permeation through films calculated from a model of Fick's second law were in good agreement with reported trends and magnitudes in bulk crosslink hydrogel materials of similar precursor monomer units. Notably, our results support that the technique described here can encapsulate cells with biocompatible hydrogel coatings that achieve similar size selective permeability behavior as previously studied cell encapsulation strategies, but with

drastically lower thicknesses and minimal synthetic material. Further, these data suggest that this surface initiated coating strategy will be capable of completely excluding SDS surfactant micelles in ASL isolation, where micelles should be larger than the polymer coating mesh size above the critical micellar concentration at ambient conditions [118].

Table 4.1: Comparison of fluorescent signal for nanoparticle-loaded films encapsulating dermal fibroblast nuclei.

Monomer (M_n)	**Fluorescence Intensity From Top and Bottom (a.u.)**	**Fluorescence Intensity From Top (a.u.)**	**Intensity to Thickness Conversion (nm/a.u.)**	**Film Thickness Estimate (nm)**
PEGDA (575)	71.9±8.2	35.9±4.1	4.0	158±16
PEGDA (3500)	63.8±13.8	31.9±6.9	6.1	200±42

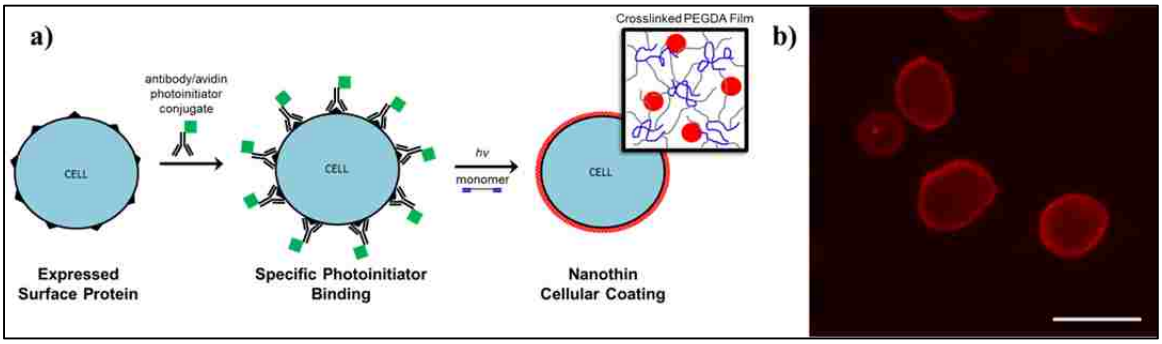

Figure 4.1: (a) Schematic of antigen-specific coating process to form nanothin films on the surface of individual cells. (b) Fluorescent image of PEGDA encapsulated Jurkats by recognition of CD45 antibody. Red fluorescence is from nile red 20 nm fluosphere nanoparticles physically entangled in the polymer film. Scale bar = 20 micron.

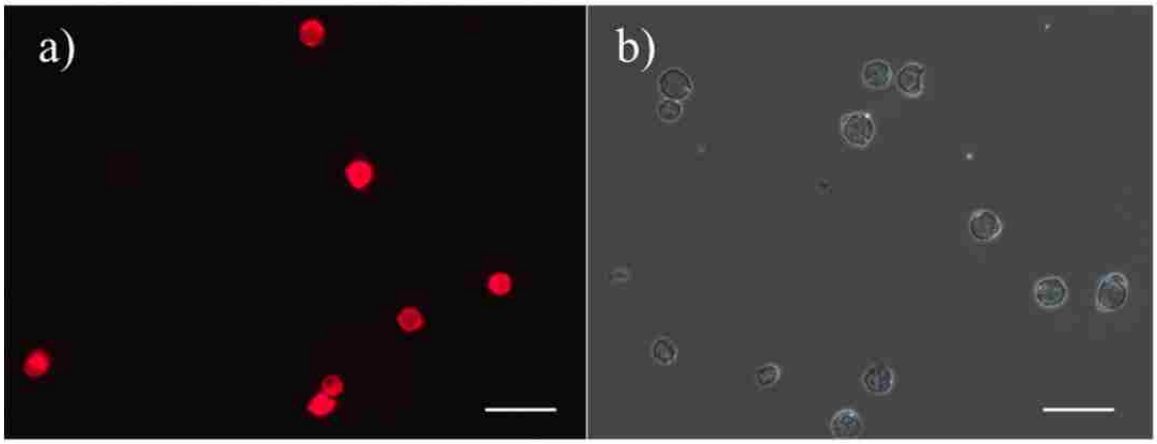

Figure 4.2: (a) Fluorescent image of PEGDA-575 encapsulated Jurkat cells. Red fluorescence is from 20 nm nile red fluorescent nanoparticles loaded in film (0.05 wt%) (b) Bright field phase image of PEGDA-575 encapsulated Jurkats. Scale bar = 50 μm.

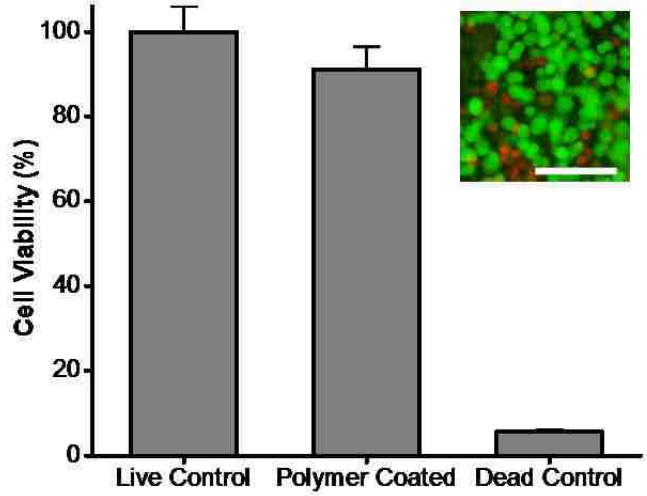

Figure 4.3: Flow cytometry analysis of coated cell viability by esterase activity. The live control represents calcein stained Jurkat cells from culture and the dead control were polymer coated cells incubated with 70% ethanol for 5 minutes before calcein staining. Image inset shows a representative micrograph of calcein AM (green) and ethidium homodimer-1 (red) staining of coated Jurkats. Student t-test for live control and polymer coated populations yielded $p=0.125$, and for polymer coated and dead control populations yielded $p=6x10^{-8}$. Scale bar represents 100 μm.

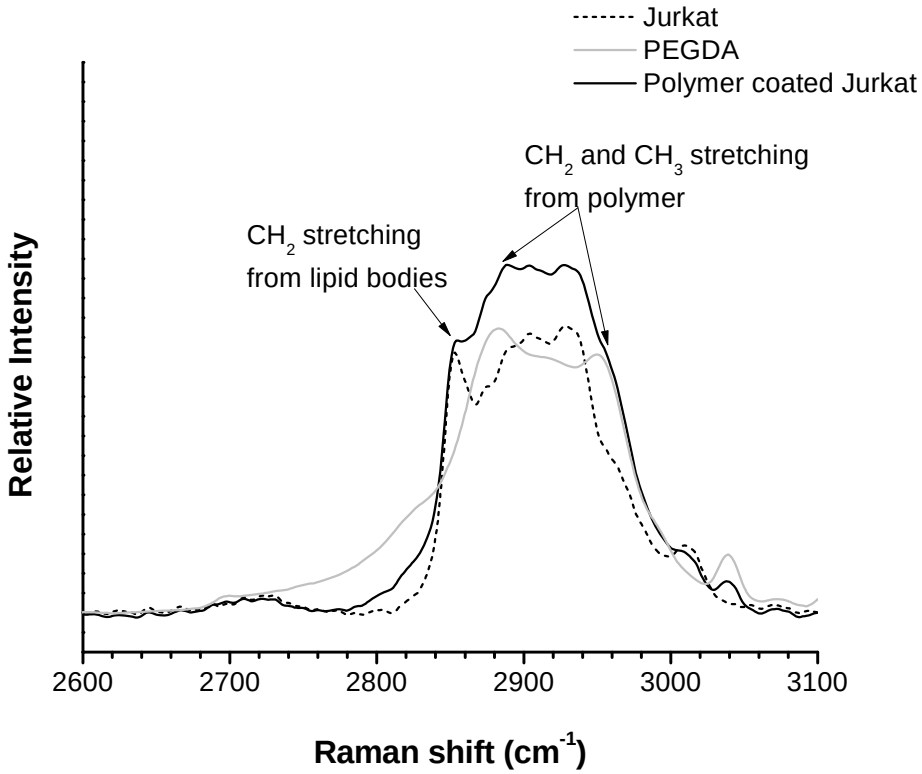

Figure 4.4: Confocal Raman microscopy surface analysis. Spectral comparison of surface of native Jurkat, coated Jurkat, and bulk cross-linked PEG diacrylate (M_n 575).

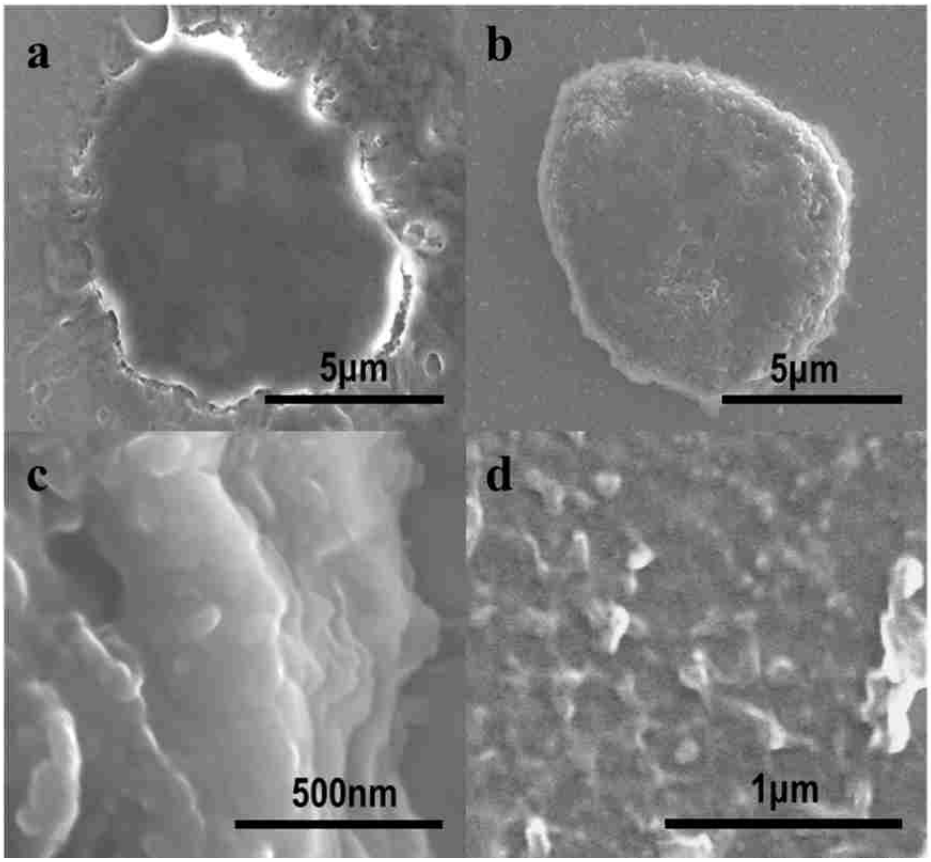

Figure 4.5: Scanning electron microscopy analysis of uncoated and coated cell surface morphology. (a) Surface morphology of a native and uncoated Jurkat cell. (b) Surface morphology of a PEG diacrylate coated Jurkat. (c) Higher magnification of coating morphology. (d) Surface of an interfacial PEG diacrylate film formed on glass.

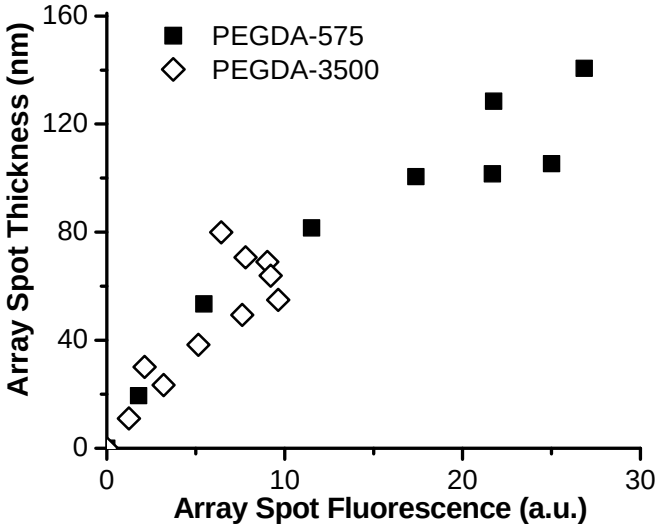

Figure 4.6: Plot of microarray spot thickness vs. spot fluorescence for different monomer molecular weights.

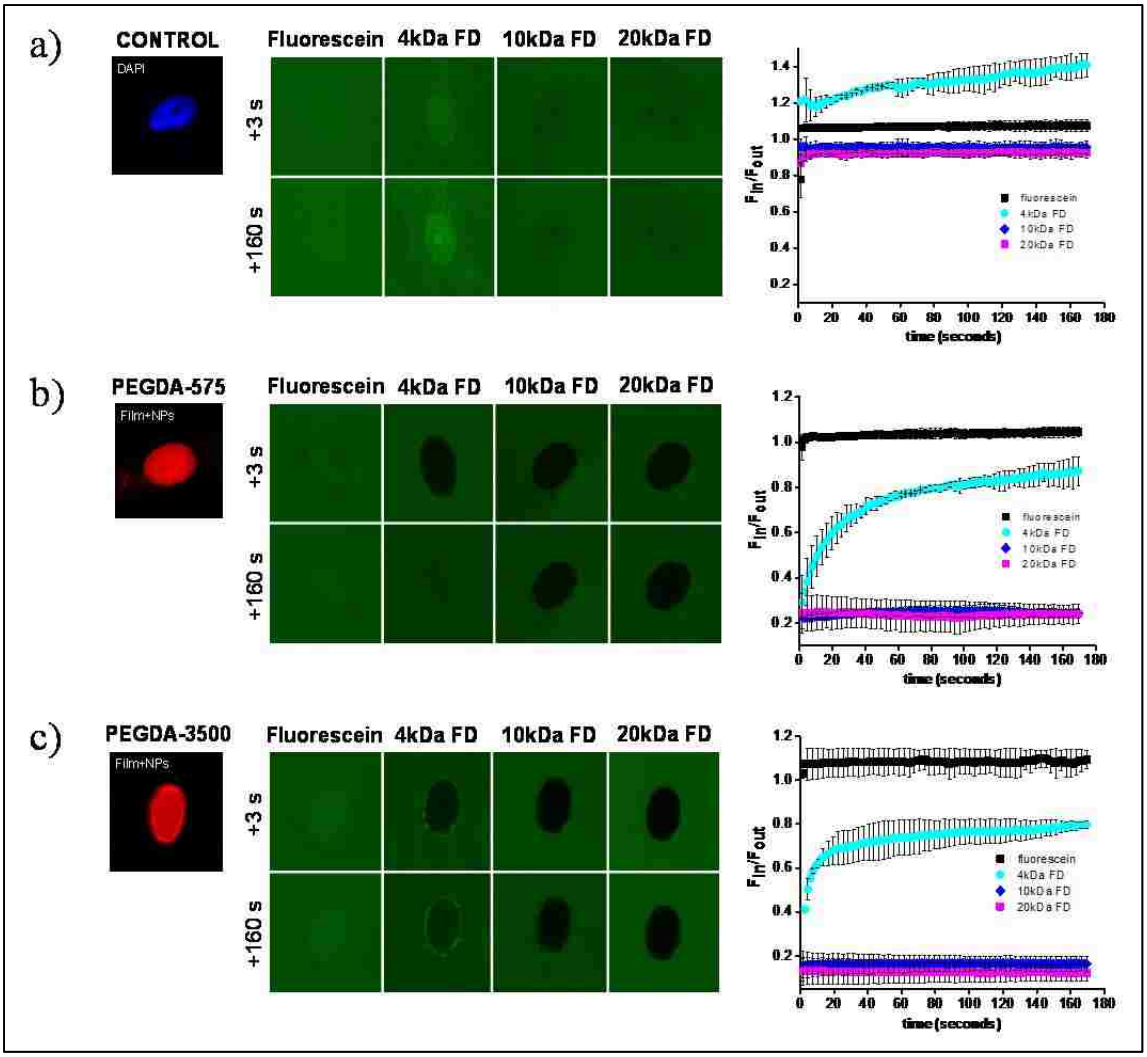

Figure 4.7: Quantification of molecular diffusion through nanoscale coatings. Image summary at t=3 s and t=160 s of passive macromolecular diffusion and time-dependent analysis of fluorescent signal from free fluorescein and FITC-Dextrans through (a) permeabilized dermal fibroblast nucleus controls, (b) PEGDA-575 and (c) PEGDA-3500 coated nuclei. F_{in} signal was from the inner domain of nuclei and F_{out} was the signal of the FITC-dextran solution outside the cell. Error bars are shown only on every other time point on plotted data for clarity.

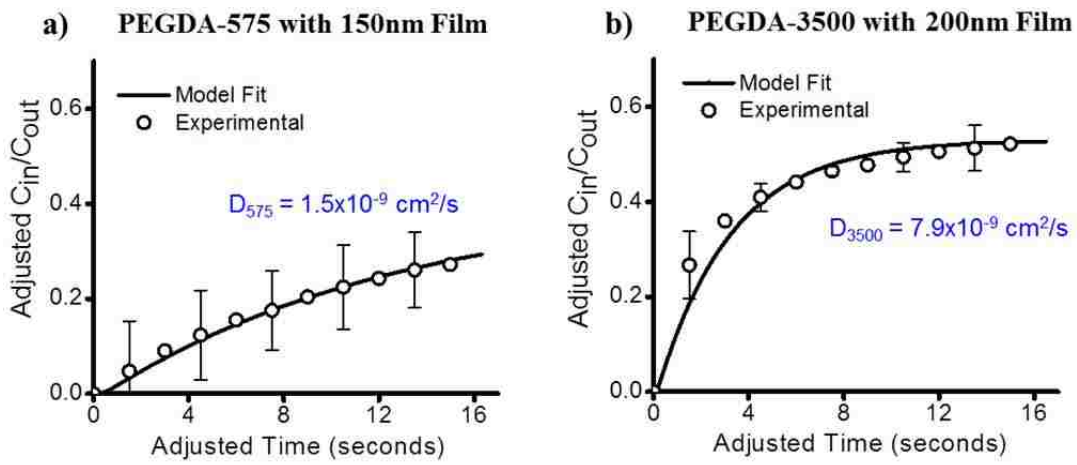

Figure 4.8: Analysis of diffusivity of 4 kDa FITC-labeled dextrans through nanoscale coatings on cellular substrates. Permeation data was fitted with a time-dependent Fickian diffusion model to calculate diffusion constants for lower and upper bounds of film thicknesses for both PEGDA-575 and PEGDA-3500 films. (a) Model fit and calculated diffusivity for diffusion of 4 kDa FITC-dextran though a PEGDA-575 film of an estimated thickness of 150 nm. (b) Model fit and calculated diffusivity of 4 kDa FITC-dextran through a PEGDA-3500 film of an estimated thickness of 200 nm. Initial concentration and time parameters were adjusted to a reference point of zero for model curve fitting.

Chapter 5: Design and Development of Protective Polymer Coatings for Rapid High-Purity Cancer Cell Isolation

In this chapter, we demonstrate the use of targeted, protective polymer coatings on cells for the rapid enrichment of cancer cells. Antigen-positive cells are coated with a biocompatible hydrogel which protects the cells, while uncoated cells are immediately lysed. The polymer coating is later removed through orthogonal photochemistry. The isolate yields viable cells which proliferate at rates comparable to control cells. Minority cell populations are enriched from erythrocyte-depleted blood to >99% purity, while the entire batch process requires one hour and <$2,000 in equipment. Batch scale-up is only contingent on irradiation area for the coating photopolymerization, as surfactant based lysis can be easily achieved on any scale. The information presented here is adapted with minor modifications from previously published work. Jacob L. Lilly worked collaboratively with Gabriela Romero as a primary contributor to protocol and assay development, experimentation, and data preparation.

> Gabriela Romero, Jacob L. Lilly, Nathan S. Abraham, Hainsworth Y. Shin, Vivek Balasubramaniam, Tadahide Izumi, Brad J. Berron. Protective Polymer Coatings for High-Throughput, High-Purity Cellular Isolation. ACS Applied Materials & Interfaces. Aug 7;7(32):17598-602, 2015.

5.1 Introduction

From the first observation of tumor cells in the peripheral blood of cancer patients, researchers have sought to develop a “fluid biopsy” in which patient-derived peripheral blood could be analyzed for circulating tumor cells (CTCs) with the goal of providing diagnostic and prognostic information with a minimally invasive procedure.

While the observed presence of tumor cells in circulation has been correlated with metastatic progression [6-8, 119], the current clinical utility of fluid biopsies remains questionable due to a lack of reliability and versatility to detect heterogeneous cancer cell types [4, 12].

Recent evidence suggests that multiple, distinct populations can arise from a single tumor primary with drastically variable phenotypes [1, 15, 17]. While the mechanisms that give rise to these populations remains an area of intense research, it has been proposed that metastatic cells can be generally categorized as either: 1) primary epithelial tumor cells spilling into circulation through leaky vasculature and 2) primary tumor cells that have lost their epithelial nature and have actively migrated into the peripheral blood in a mesenchymal state. Once in systemic circulation, little is known about the biological functionality that leads to colonization of metastatic foci at distant sites. Practically, functional characterization of CTCs has been encumbered by the extreme rarity at which they seen of ~1 per 10^6. Further, many CTC isolation methods currently available require fixation and intracellular staining to determine epithelial identity, which prevents further examination of behavior and functionality after sorting. In order to fully bridge our understanding of the mechanisms that allow an epithelial cancer cell to survive in circulation an eventually spread the disease, viability of these rare cell populations must be preserved during enrichment.

Researchers currently have a portfolio of technologies to meet many of their cell sorting needs. Critically, there is a technology gap in isolating viable, rare cancer cells in a rapid, highly-pure manner. Magnetic sorting excels in high-speed, low cost sorting, but is hampered in purity by nonspecific adsorption in antigen-positive sorts [38].

Fluorescence activated cellular sorting (FACS) delivers exceptional purity but at low throughput and high cost [120]. Microfluidic approaches are promising, but purities for populations adhered to antibody coated surfaces is typically low (<50%) [34], throughput is limited (~10 mL or 10^8 cells per day) [121], and recovery of isolated cells from the devices has proven difficult [122]. The most common approach for sorting large numbers of antigen positive cells at high purity is a sequential approach where cells are enriched with magnetic sorting, and purity is attained with FACS [41]. Even in this debulked case, each antigen positive cell must pass through a FACS system, and throughput for high purity sorts is typically ~10^7 cells/day, involving time-consuming sterilization and gate adjustment operations. The stark contrast in magnitude between rates achievable with FACS and the requirements of CTC isolation illustrates a critical obstacle in the development of a reliable fluid biopsy.

Here, we present Antigen Specific Lysis (ASL) technique as a fundamentally new approach to cellular sorting (**Figure 5.1**). Individual, antigen-positive cells are protected with a biocompatible hydrogel coating. ASL utilizes an antibody covalently conjugated to a photoinitiator, and upon incubation of cells in this conjugate, the initiator is localized to only antigen positive cells. After further exposure in a macromer solution and irradiation, polymer coatings are specifically formed around the targeted cells. The polymer coating protects the cells from a surfactant solution, while uncoated cells can be immediately lysed. Following lysis, the polymer coating is removed through orthogonal photochemistry. Different cellular activity indicators were used to evaluate viability after each step in ASL process. The isolate has >50% viability yield, negligible apoptotic activity and regulated proliferation rate. ASL purity was evaluated by utilizing GFP as

identity marker in a GFP-positive A549 cell line, where we detect >97% purity in the isolate. Specificity of ASL was corroborated by sorting a particular cell population from cell mixtures and further from leukocyte-enriched plasma from human blood samples. The feasibility and adaptability of ASL technique promises unprecedented sorting rate and throughput.

5.2. Materials and Methods

5.2.1 UV Degradable Monomer Synthesis

A poly(ethylene glycol) diacrylate macromer (M_n ~ 3500 Da) incorporating an *ortho*-nitrobenzyl functionality (**Figure 5.2**) was synthesized according to a published protocol by Kloxin et al. Structure and purity was confirmed by H-NMR [123].

5.2.2 PEG-diacrylate Monomer Synthesis

A poly(ethylene glycol) diacrylate macromer was synthesized with a similar molecular length as UV degradable macromers. Poly(ethylene glycol) (PEG, M_n ~3350 Da, Sigma Aldrich) was added to the bottom of an additional funnel flask at a 10 gram batch size and purged with ultra-pure N_2 for 10 minutes. Anhydrous dichloromethane (DCM, 30 mL) was added to the flask, and the PEG was allowed to dissolve under magnetic stirring for 5 minutes. The flask was kept in a stirred room temperature water bath (>500 mL) to serve as a heat sink for the exothermic reaction. For acrylation of the PEG macromer, a molar ratio of 1:4:4 PEG:acryloyl chloride (AC, Sigma Aldrich):triethylamine (TEA, Acros) was used. The calculated amount of TEA was added directly to the bottom of the flask under continuous stirring. The calculated amount of AC was mixed with 5mL of DCM and injected through a septum into the top of the addition funnel, and the entire apparatus was then purged with N_2 for 15 minutes. The

AC/DCM solution was then added dropwise (~1 drop every 5 s) with the addition funnel under continuous N_2 purge and stirring. When the entire amount of AC/DCM solution was added to the PEG/TEA/DCM solution, purging was stopped and the apparatus was sealed, covered with aluminum foil and reacted overnight. The resulting pale yellow mixture was then filtered through a Buchner funnel and washed with excess DCM to remove the bulk of the TEA salts that formed during the reaction. Next, 10-fold molar excess sodium carbonate was added to the solution, and the slurry was stirred vigorously for 1 hour. The mixture was then again passed through a Buchner filter funnel and washed with DCM to remove the insoluble sodium carbonate. A packed bed of alumina (~3 cm thick) was then prepared in a glass frit column, and the solution was passed through the bed and washed with DCM. The DCM was then evaporated off so that the solution volume was ~40 mL, and cold diethyl ether (400 mL) was added to precipitate the PEG diacrylate product. The mixture was kept at 4˚C for at least 1 hour to allow full precipitation. The white precipitate was then collected with a Buchner filter funnel and allowed to dry overnight in the dark. This process of dissolving in ~40 mL of DCM and then precipitating the PEG diacrylate product in cold ether and filtering was repeated to further remove any impurities. Structure and extent of acrylation (90%) were confirmed with H-NMR.

5.2.3 Photopolymerization of Degradable Coatings on Cultured Jurkat Cells In Suspension

Jurkat cells (ATCC) were cultured to ~60% confluency in RPMI-1640 (Cellgro) supplemented with 10% fetal bovine serum (FBS, Gibco) and 100U Penicillin, 10 mg/mL Streptomycin (Gibco). For each polymerization trial, 1.5 x 10^6 Jurkat cells were collected

in culture media. In a 15 mL conical tube, the cells were centrifuged at 300*xg* for 5 minutes at 4 °C. The culture media was removed, and the cell pellet was resuspended by gentle vortexing in 115 μL of DPBS (Gibco) with 3% FBS and 35 μL biotinylated mouse anti-human CD45 (BD Biosciences), and incubated for 40 minutes at 4 °C. Following incubation with primary antibody, the cell suspension was rinsed twice by centrifuging at 300x*g* for 5 minutes and then resuspending with cold DPBS with 3% FBS followed by gentle vortexing. After the final rinse, the cell pellet was resuspended in 1 mL of cold PBS with 3% FBS with 25 μg/mL streptavidin-eosin-5-isothiocyanate (SA-EITC), gently vortexed and incubated at 4 °C for 30 minutes. Streptavidin (Thermo Scientific) and eosin-5-isothiocyanate (Sigma Aldrich) were reacted and purified in-house by the method described by Hansen et al. (2007) [98], The cell suspension was then rinsed once, as before, with cold PBS with 3% FBS and then once with cold DPBS. The monomer mixture was then prepared as follows: 25 wt% UV cleavable PEG diacrylate [123], 21 mM triethanolamine, 35 mM 1-vinyl-2-pyrrolidinone, and 0.05 wt% nile red 20 nanometer fluorescent nanoparticles (Fluospheres, Invitrogen) in 1x phosphate buffer. The solution was bubbled with humidified ultra-pure N_2 for approximately 3 minutes to remove dissolved oxygen and reduce turbidity. The cell pellet was resuspended in 300 μL monomer solution, gently vortexed, and placed in pre-cooled Chip-Clip well (Whatman) with a standard microscopy slide (Fisherbrand). The Chip-Clip was then placed in a sealed clear plastic bad and purged with humidified N_2 for 3 minutes. While continuing to purge, the reaction was initiated by turning on an LED lamp (Thor Labs) emitting 530 nm light at 30 mW/cm^2 and centering the irradiation area on the well containing the cell suspension. The photopolymerization was allowed to proceed for 10 minutes, at which

time the Chip-Clip was removed from the bag and the cell suspension was removed rinsed 3 times with room temperature DPBS.

5.2.4 Photopolymerization of Degradable Coatings on Cultured A549 Cells in Suspension

Before a coating experiment, A549 cells (ATCC) were cultured to ~80% confluency in RPMI-1640 with 10% FBS and 100U Penicillin, 10 mg mL^{-1} Streptomycin. The culture flask was then rinsed with warm PBS 1x to remove media, and then trypsin/EDTA solution was added for ~5 minutes to detach the adherent cells. After detachment, cells were washed with 1 part trypsin neutralizing solution, pelleted and resuspended in culture media. For each polymerization trial, 1.5 x 10^6 A549 cells in 1 mL of media were used. Throughout the protocol, a rinsing solution consisting of DPBS 1x (free of calcium and magnesium), 5mM EDTA, and 3% FBS was used to minimize A549 attachment during immunolabeling and polymerization. The cells in media from culture were centrifuged at 300*xg* for 5 mins at 4 °C and resuspended in 100 μL rinsing solution and 1 μL of stock mouse anti-human EpCAM (BioLegend) by gentle vortexing. The cell suspension was incubated in primary antibody for 40 minutes at 4 °C. At the end of the incubation the sample was centrifuged at 300x*g* for 5 mins at 4 °C and resuspended in 1 mL rinsing solution with 5 μL stock biotinylated goat anti-mouse IgG, gently vortexed and incubated at 4 °C for 40 minutes. The cells were then again centrifuged as before, rinsed twice by centrifuging and resuspending with rinsing solution. After the final rinse, the cell pellet was resuspended in 1 mL of cold rinsing solution with 25 μg/mL streptavidin-eosin isothiocyanate (SA-EITC), gently vortexed and incubated at 4 °C for 30 minutes. The cell suspension was then rinsed twice, as before, with cold rinsing

solution. The monomer mixture was then prepared as described previously for Jurkat coating: 25 wt% UV cleavable PEG diacrylate [123], 21 mM triethanolamine, 35 mM 1-vinyl-2-pyrrolidinone, and 0.05 wt% nile red fluorescent nanoparticles in 1x phosphate buffer. The solution was bubbled with humidified ultra-pure N_2 for approximately 3 minutes to remove dissolved oxygen and reduce turbidity. The cell pellet was resuspended in 300 μL monomer solution, gently vortexed, and placed in a pre-cooled Chip-Clip well (Whatman) with a standard microscopy slide (Fisherbrand). The Chip-Clip was then placed in a sealed clear plastic bag and purged with humidified N_2 for 3 minutes. While continuing to purge, the reaction was initiated by turning on an LED lamp (Thor Labs) emitting 530 nm light at 30 mW/cm^2 and centering the irradiation area on the well containing the cell suspension. The photopolymerization was allowed to proceed for 10 minutes, at which time the Chip-Clip was removed from the bag and the cell suspension was removed and rinsed 3 times with room temperature DPBS.

5.2.5 Polymerizing Cell Mixtures

In experiments with mixtures of Jurkat and A549 cells, each respective cell type was cultured and collected as previously described and then combined at varying ratios. The polymerization protocol used depended on the cell type targeted for isolation. Because A549 cells were present in these experiments, 5 mM EDTA was included in all rinsing solutions to prevent cell attachment.

5.2.6 Removal of Antigen-Negative Cells by Surfactant Lysis

Following photopolymerization and subsequent rinsing, cell mixtures were resuspended in 500 μL PBS 1x and gently vortexed. To the cell suspension was added 500 μL of 10% sodium dodecyl sulfate (SDS) in PBS 1x and gently mixed by pipette to

get final concentration of 5% SDS in PBS 1x. The suspension was then immediately centrifuged at 300*g* for 5 minutes to collect the polymer coated, antigen-positive cells. The surfactant solution was removed by pipette, and the pellet was rinsed twice more with cold DPBS.

5.2.7 Coating Removal by UV Degradation

Polymer coated cells were suspended in 300 µL of 10 mM EDTA gently vortexed and pipetted into a Chip Clip well. A UV LED lamp emitting 365 nm light was set up to irradiate the entire well at 10 mW/cm^2 for 15 minutes, as shown in **Appendix A-1.** The cell solution was then removed from the well, and the well was rinsed twice and combined with the removed solution. The cells were then pelleted by centrifugation at 300*g* for 5 minutes at 4 °C, and then resuspended in PBS 1x. The cells were rinsed twice more in DPBS 1x similarly by pelleting and resuspending.

5.2.8 Cell Identity Assays

For cytometry experiments, an Accuri C6 flow cytometer was used. Gating between coated and uncoated cells is based on nanoparticle fluorescence (535/575 nm) and forward scatter. Each experiment was set to count 100,000 events and each run was recorded using identical measurement parameters. Each condition tested was replicated five times per experiment, and each experiment was repeated at least 3 times on different days. To support the cell identity analyses above, a cytometry experiment was designed to ASL sort GFP-transfected A549 cells (Cell Biolabs), where GFP signal serves as a strong biochemical reporter for A549 identity. GFP positive A549 and Jurkats were cultured in RPMI-1640 and collected as previously described above, and mixed at a ratio of approximately 10% GFP positive A549 into 90% Jurkats, where gating was set on FL-

1 vs forward scatter based on single cell population controls. GFP-A549 cells were targeted with anti-EpCAM, and coated by photopolymerization of 25 wt% PEG-diacrylate macromer similarly to the coating protocol detailed previously. After SDS lysis and rinsing with DPBS/FBS, cells were suspended in culture media and incubated overnight to allow recovery of GFP signal that is partially photobleached during photopolymerization. Cells were then resuspended in DPBS/FBS and analyzed again by cytometry. The experiment was repeated 3 times on different days with 1,000 events per replicate.

5.2.9 Viability and Proliferation Assays

Cell viability was determined by MTT, calcein, caspase-3/7, and SYTOX assays. Measurements were taken after antibody incubations, polymerization, surfactant lysis, and UV degradation. After the final rinse with cold PBS 1x at each step, cells were centrifuged at 300*g* for 5 minutes and resuspended in 50 nM of calcein AM (Invitrogen) in PBS and incubated for 15 minutes at 4 °C. Flow cytometric analysis was then performed to measure calcein fluorescence. First, a threshold of fluorescence was generated using uncoated and cells without exposure to calcein as control samples. All events corresponding to uncoated cells without calcein were located at intensities below this threshold for both green and red fluorescence, while events corresponding to polymer coated cells without calcein were located at intensities below the threshold for the green fluorescence channel. Each experiment was set to count 100,000 events per run and each run was recorded using identical measurement parameters. Each condition tested was replicated five times and each experiment was repeated at least 3 times in different days.

The variation between each replicate was always less than 5% and between experiments less than 10% in cell mixtures.

Cell viability after immunostaining, polymerization, lysis and polymer degradation was also studied with the MTT assay. After each step, 100,000 cells in 200 μL of culture media were seeded into each well of 96-well plates. Thiazolyl Blue Tetrazolium Bromide (Sigma Aldrich) was dissolved in PBS 1x at a concentration of 5 mg/mL. Then, 20 μL of MTT solution was added into each well and incubated for 3 hours. The absorbance was measured by means of a plate reader at 570 nm.

To further assay viability, a flow cytometry based caspase-3/7+SYTOX reporter kit (Invitrogen) was used. Approximately 10^6 Jurkat cells were obtained from culture, coated with polymer via anti-CD45, exposed to SDS lysis, then to degradation conditions of UV light in 10 mM EDTA as described above**.** Apoptosis and membrane integrity were probed after polymerization and degradation steps by incubating samples with both 500 nM caspase reporter reagent and 1 μM SYTOX reagent for 60 minutes at room temperature in the dark. For analysis, flow cytometry gating was set from Jurkat controls to 1,000 events per replicate. Fluorescence analysis was performed by excitation with a 488 nm laser with a 530/30 BP filter for the caspase channel and a 675/25 nm BP filter for SYTOX. A dead control consisted of 70% ethanol fixed Jurkats, and an apoptotic control was induced with a 3 hour incubation of Jurkat cells at 37 °C with 10 μM camptothecin in RPMI-1640 culture media. Cell proliferation after polymer degradation was studied with the MTT assay. 5,000 cells in 200 μL of culture media were plated into each well of 96-well plate. During 5 days of co-incubation, 20 μL of MTT solution (5

mg/mL in PBS 1x) was added into each well of the plates and incubated for 3 h. The absorbance was measured by means of a plate reader at 570 nm.

5.2.10 ɣH2AX Foci Quantitation

A549 cells were plated on 12 mm coverslips and incubated in DMEM 10% FBS + 1% streptomycin/penicillin + 1 % L-Gln for 16 h. The coverslips were soaked in 2 ml PBS in 6 cm dishes, and exposed to 10 mW/cm^2, 365 nm irradiation for 10 or 20 min, followed by incubation in a regular medium for 30 min, 1 h, or 3 h. Cells were then fixed in 50% methanol followed by 100 % methanol, and then stained with anti-ɣH2AX (Millipore) and probed with anti-mouse IgG-Alexa Fluor 488. Cells with foci were counted to calculate mean %cells with foci from 10 independent observations. Foci formation induced by 5 minutes of 0.2 mM H_2O_2 and measured after 30 minutes in regular medium post exposure treatment is shown as a ɣH2AX positive control.

5.3 Results and Discussion

5.3.1 Antigen Specific Polymer Coating

Antigen Specific Lysis (ASL) consists of specific cellular protection by a temporary polymer coating and the subsequent lysis of unprotected cells (**Figure 5.1**). The formation of a polymer film requires a polymerization initiator [124], and ASL utilizes antibodies to localize eosin (a type II photoinitiator) on the surface of only antigen positive cells [97, 100, 125]. The monomer is prepared in a mixture composed by 25 wt% UV cleavable PEG diacrylate [123], 21 mM triethanolamine, 35 mM 1-vinyl-2-pyrrolidinone, and 0.05 wt% fluorescent nanoparticles in 1x phosphate buffer. Coatings are formed upon immersion in nitrogen purged monomer mix and 530 nm LED irradiation (30 mW/cm^2) for 10 minutes, where a red fluorescent polymer coating is

formed on the outside of only targeted, initiator-labeled cells. When the photoinitiators are targeted against protein tyrosine phosphatase (CD45 antigen), protective polymer coatings are formed on the outside of Jurkat cells [97, 126]. Unprotected cells (**Figure 5.3.a**) are lysed and killed by a 10 minute exposure to 5% SDS (**Figure 5.3.b**) [127], while we observe that cells encapsulated in fluorescent polymer coatings retain cellular integrity (**Figure 5.3.c, 5.3.d**). Cellular integrity and activity was determined by caspase-3/7 + SYTOX assay where a cell population of 81.7 ± 8 % is detected viable (**Figure 5.4**). Viability by cellular activity was determined at each step in the ASL process by calcein esterase activity and capspase-3/7 + SYTOX assays. Calcein esterase assays showed more than 80% viable Jurkat cells after polymer coating (**Figure 5.3.e**). The lack of activation of caspase-3/7 apoptotic pathways by caspase-3/7 + SYTOX assay reveal that after the polymer coating process, a negligible Jurkat cells population (0.2 ± 6 %) was in the apoptotic stage and 14.5 ± 9 % of the cells were necrotic (**Figure 5.4**). The high viability for these coating materials is to be expected given previous studies using similar macromers and initiation chemistry [90, 126]. These same macromers were used with >80% viability in tissue encapsulation studies by Kloxin et al. [123] and with >90% viability by Griffin et al. [128] and by DeForest et al. [129]. Additionally, the polymerization by a type II photoinitiation system (eosin with a tertiary amine coinitiator) strategy has been extensively studied by the Hubbell [60, 80] and Lin [130, 131] groups for pancreatic islet and pancreatic cancer tissue engineering studies.

This cellular protection by a targeted coating is the foundation of ASL sorting, where complete elimination of the untargeted population is feasible through conventional approaches of cell lysis. While enrichment based on the exclusion of SDS is a chemical

means of selection, we have also evaluated the preservation of cellular function in hypotonic solutions using similar coatings. Immersion of 10^5 uncoated Jurkat cells in 1 mL of pure water results in a large osmotic imbalance, leading to swelling and rupture of the cell [132]. When Jurkat cells are coated with a PEG diacrylate polymer, the polymer coating preserves cell membrane integrity and enzymatic function (**Figure 5.3.d, 5.3.e**). In each mode of lysis, we have observed reductions in the numbers of uncoated cells. Cell exposure to 5% SDS led to an undetectable lysed population, while the water treatment results in a statistically insignificant ($p=0.0517$) number of viable cells. Polymer coating protection from SDS or hypotonic lysis demonstrates the potential for ASL to deliver 100% pure populations.

5.3.2 Specificity of ASL

The limiting factor for ASL purity is the specificity of polymerization afforded by the antibody-targeted initiator species. To investigate the specificity of these polymer coatings, we isolated A549 cells from a mixed population with Jurkat cells. Approximately 10^4 A549 cells were mixed with 10^5 Jurkat cells. For the sake of adaptability, we synthesized a streptavidin-eosin conjugate that can be targeted to A549 cells through the use of biotinylated antibodies and antibodies against epithelial cell adhesion molecule antigen (anti-EpCAM). After photopolymerization (as described above), the mixture of cells were analyzed by flow cytometry, and the two distinct populations are consistent with control populations of coated A549 cells and uncoated Jurkat cells. The fraction of each gated population (8% A549 to 90% Jurkat, **Figure 5.5.a**) is consistent with the fraction of starting populations. Upon addition of 5% SDS in PBS to the pelleted cellular mixture, a purified population of polymer coated A549 cells

is obtained through centrifugation (0.3 x g for 5 minutes) and rinsing in 3% FBS in PBS. Flow cytometry shows >98% of the population to be consistent with coated A549 cells (**Figure 5.5.b**).

To demonstrate that ASL specificity is feasible for other targeted populations, we performed a similar experiment to isolate a minority of 10^4 Jurkat cells from a mixture with 10^5 A549 cells. We labeled Jurkat cells with initiator by incubation in 1:5 biotinylated human anti-CD45 for 40 minutes in a solution of 3% FBS in 1x PBS, followed by incubation in 10 μg/mL streptavidin-eosin for 30 minutes. After photopolymerization with 530 nm light, the two distinct populations are consistent with initial populations of coated 9% Jurkat cells and naïve 91% A549 cells (**Figure 5.5.c**). Upon lysis with 5% SDS in PBS, ASL yielded a >96% pure Jurkat population as is observed by flow cytometry (**Figure 5.5.d**).

Purity was further supported by fluorescence analysis when sorting a GFP-transfected A549 cell line. Polymer coating was performed in cell mixtures composed by 90% Jurkat cells and 10% GFP-positive A549 cells (**Figure 5.6.a**). The GFP fluorescence signal serves as a strong biochemical reporter for A549 cell identity. GFP-positive A549 cell population is targeted using anti-EpCAM as described above for A549 cell sorting. After polymerization, unprotected cells are lysed with 5% SDS. Prior to flow cytometer analysis of the sorted population, cells are cultured overnight in media to allow the recovery of GFP signal from photobleaching caused by the photopolymerization. ASL yields a highly pure isolated fraction consisted of 97.1 ± 2.3 % GFP-positive A549 cells, and only 2.9 ± 2.3 % GFP-negative cells per each 10^4 cell batch (**Figure 5.6.b**).

5.3.3 Release of Sorted Cells From Polymer Coating

Removal of the polymer coating is essential for translation of ASL as a cell isolation technology. We use a UV-degradable PEG-diacrylate monomer developed by Kloxin et al. [123] to temporally control the presence of the crosslinked polymer coating. Coated Jurkat cells were released from the polymer coating through 10 minute exposure to 10 mW/cm^2, 365 nm light in PBS and 10 mM EDTA. As photobleaching and particle release possibilities weaken the certainty of direct observation of coating removal by fluorescent means, the removal of the coatings was confirmed by proliferation assays of the released cells and comparison to naive Jurkat cell. Released Jurkat cells proliferate at rates comparable to naïve Jurkat cells (**Figure 5.7.a**), indicating the sufficient degradation of the polymer coating to allow proliferation. We also evaluated the proliferation of released A549 cells, which are anchorage dependent. The A549 cells had a 2 day lag in proliferation (**Figure 5.7.a**). Discrepancies between the anchorage dependent A549 and the anchorage independent Jurkat cells suggests residual polymer may interfere with critical cell-substrate interactions. Observation of the cells in culture showed viable cell spreading and residual red fluorescent polymer remaining after 1 day (**Figure 5.7.c**) and although the fluorescent polymer can be observed still after 4 days of culturing (**Figure 5.7.d**), released A549 cells recover and proliferate at rates comparable to naive A549 cells. PEG hydrogels have been commonly used to prevent cell-substrate interactions, and the screening of these interactions by residual polymer highlights an opportunity for improvement of ASL through the more efficient removal of the polymer coating. Yield of viable cells throughout the ASL process is 59 ± 1.2 % as determined by MTT assay, (**Figure 5.7.b**) comparable to the viability achieved by FACS [133-135], which is

promising for a newly-discovered technology. Cell viability was further supported by caspase-3/7 + SYTOX (**Figure 5.4**). From the released cell population, more than the 72.6 ± 6.8 % of the cells remained alive, 19.5 ± 5 % were necrotic cells and the apoptotic activity detected was negligible (0.5 ± 4 %).

The impact of UV light on the cell viability was studied by calcein assay and by DNA damage quantification. There is a small impact (<10%) of UV light in the cell viability after polymer degradation (**Figure 5.8.a**). DNA damage was quantified by assessing the response of histone-2AX (H2AX) phosphorylation (ɣH2AX), a marker of DNA double strand breaks [133-136]. ɣH2AX foci induction was monitored following different time interval between UV light exposure and incubation in culture media (**Figure 5.8.b**). Induction of ɣH2AX foci was negligible and not affected by the radiation exposure time, suggesting no DNA damage in the cells after releasing them from polymer coating upon UV irradiation.

5.3.4 ASL in Spiked Blood

Cellular isolation from actual biological samples is often more difficult than the isolation of different cultured cell populations in buffers. Of these samples, blood is a commonly targeted tissue for cells, and has many clinically relevant applications ranging from progenitor cell isolation [137, 138] to cancer cell isolation [139, 140]. To support the generalized use of ASL for isolations of rare cell populations beyond cultured cells, we spiked A549 cells into the leukocyte-enriched plasma fraction harvested from asymptomatic human blood subjected to cell sedimentation (**Figure 5.9.a**).

The mixed population was sequentially labeled with anti-EpCAM, biotin-anti-Mouse IgG, and streptavidin-eosin, prior to polymerization in the monomer formulation

with 530 nm light at 30 mW/cm^2 for 10 minutes. The polymer coated A549 cells are distinguished from blood components by flow cytometry, constituting 16% of the nucleated cells in the mixture (**Figure 5.9.b**). After exposure to 5% SDS, around 99% of nucleated cells remaining correspond with A549 cells as quantified by flow cytometry (**Figure 5.9.c**).

The scale-up of ASL promises the rapid processing of large quantities of cells. ASL batch throughput is limited only by the lamp irradiation area. While our current experiments are performed with inexpensive LEDs using a ~40 cm^2 irradiation area, there is a possibility of adaptation to commercially available irradiation chambers with bigger irradiation areas (>850 cm^2). By starting with a large sample, rare populations may be isolated in appreciable numbers (~10^{10} cells per hour), allowing occult phenotypes to be studied beyond single cell analytical techniques.

5.4 Conclusions

ASL constitutes a completely unique approach for cellular isolation. Even at this early stage in development, the potential is clear for a high-purity, high-viability cell isolation technique for both small and large batch isolations. As in the popular antibody-coated microfluidic systems, ASL is limited to single antigen sorts at a given sensitivity. As such, it provides a high throughput alternative to microfluidic sorting which complements existing antigen-negative magnetic sorting technology for high throughput, high purity applications. Prior work has also shown the ease of tuning the sensitivity of antibody-directed polymer coating system through antibody dilution or competitive binding with non-labeled probes [141]. ASL's reliance on common light sources (LEDs from epifluorescent microscopes) allows capital costs to be >100x cheaper than a FACS

system. Furthermore, all ASL processing can be performed in common disposable labware, eliminating the expensive and time consuming sterilization procedures used in most other sorting techniques. Additionally, others have shown fluorescein to be a reasonable alternative to eosin-based initiation, where FITC-labeled antibodies could potentially replace our custom eosin conjugates [141]. Further developments using fluorescein-antibody conjugates for polymerization initiators would logically make ASL even more accessible to a broad range of researchers.

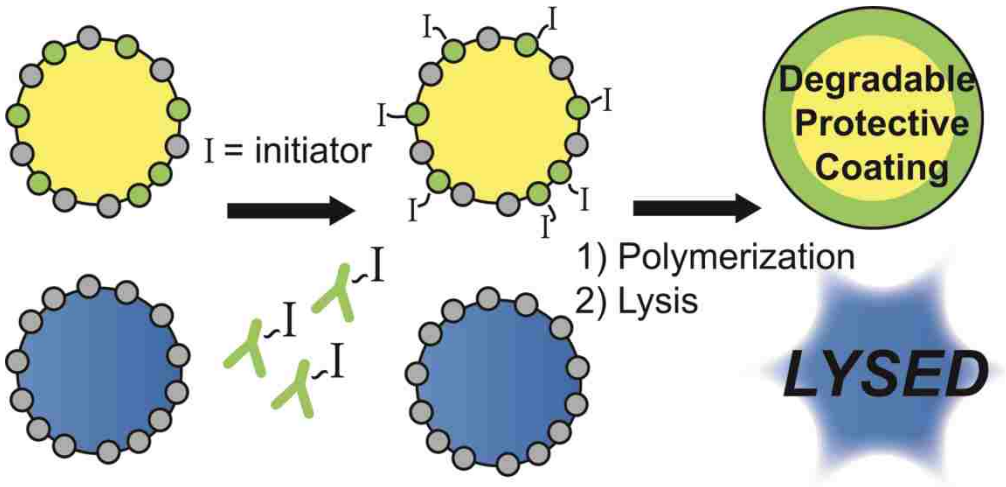

Figure 5.1: Schematic figure of Antigen Specific Lysis. Cells are immunolabeled with polymerization initiators, and protective coatings are formed only on initiator labeled cells. Unprotected cells are lysed while coated cells remain viable.

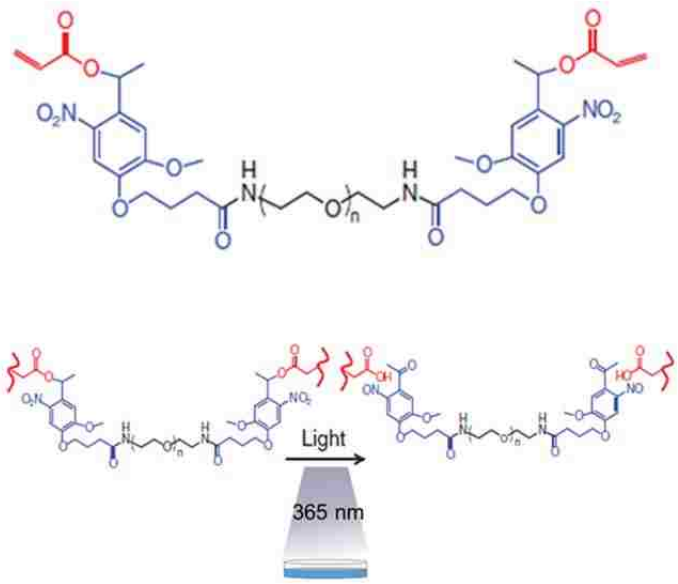

Figure 5.2: Structure and photocleavage route of *ortho*-nitrobenzyl-PEG-diacrylate macromers. Adapted from Kloxin et al. (2009) [16].

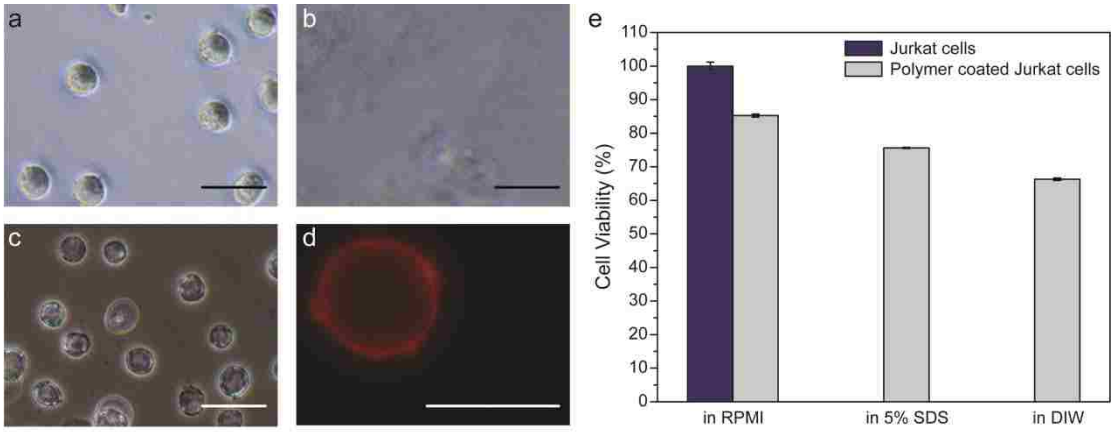

Figure 5.3: Protection of marker-positive cells through polymerization. a) Naive Jurkat cells. b) Uncoated Jurkat cells are lysed in <10 seconds in 5% SDS. Only sparse cellular debris remains in the viscous lysate. c) Polymer-coated Jurkats intact are after 10 minutes in 5% SDS. d) Epifluorescent image of Jurkat cells coated with a red fluorescent nanoparticle-loaded polymer in pure deionized water. Scale bars are 25 μm. e) Calcein viability assay of Jurkat cells and polymer-coated Jurkat cells after 10 minutes in indicated solution. Data are mean ± s.d.

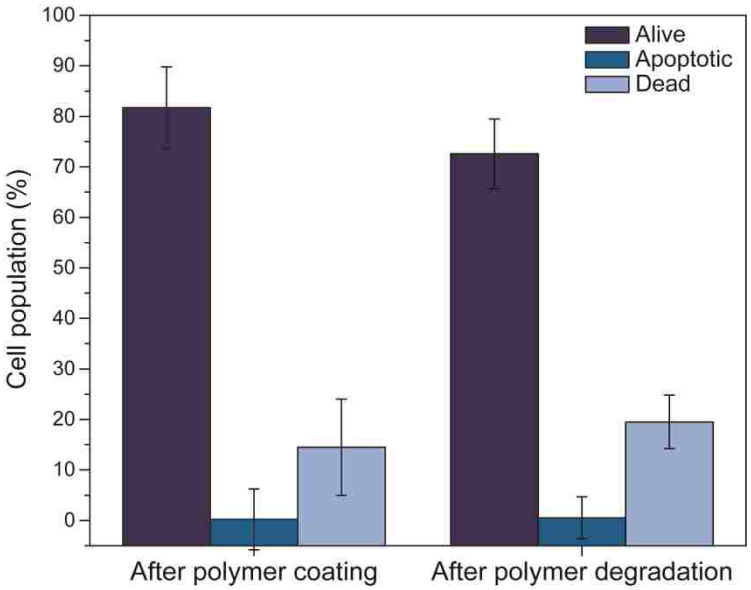

Figure 5.4: Viability of Jurkat cells before and after polymer degradation measured by Caspase and SYTOX assay. Data are mean ± standard error.

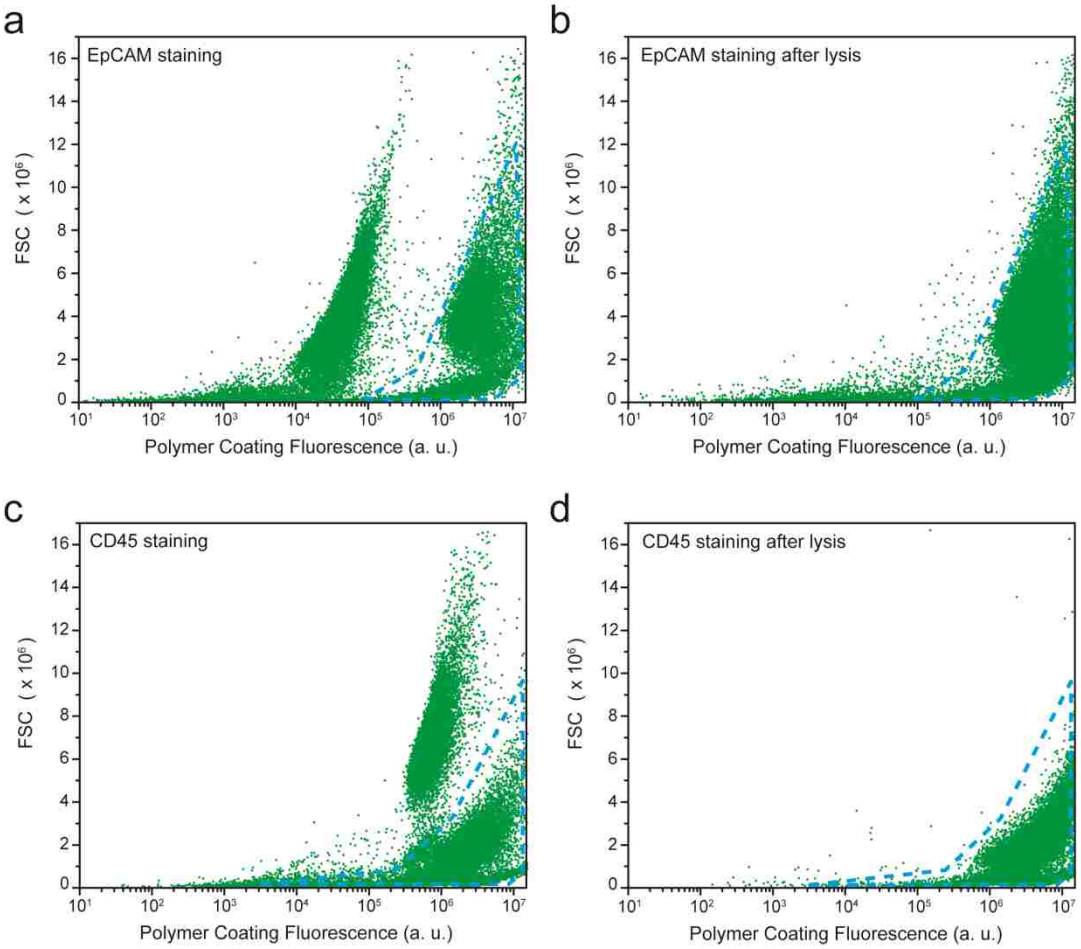

Figure 5.5: Specific lysis of cultured cells. Representative flow cytometric analysis of populations before and after exposure to SDS. a) Coating targeted to EpCAM+ cells from an initial population of 9% Jurkat and 91% A549 after polymerization. b) Population from (a) after 5 minute exposure to 5% SDS. c) Coating targeted to CD45+ cells from an initial population of 9% A549 and 91% A549 after polymerization. d) Population from (c) after 5 minute exposure to 5% SDS.

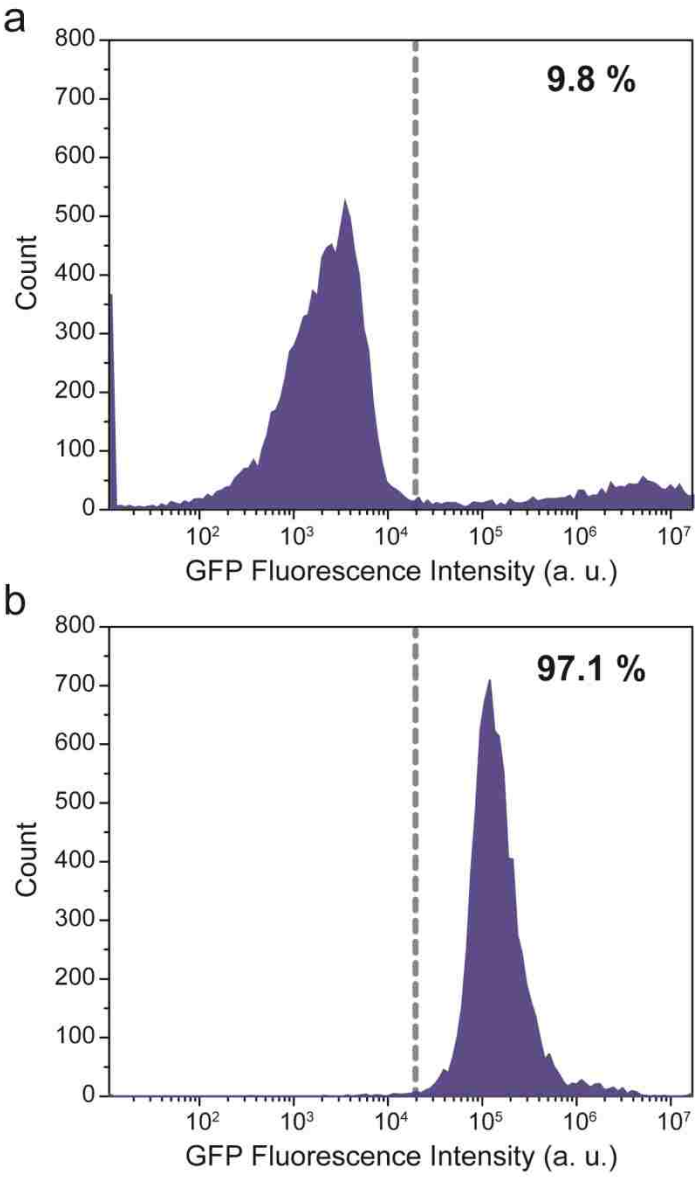

Figure 5.6: Antigen Specific Lysis purity from a cell mixture composed by 90% Jurkat cells + 10% GFP-positive A549 cells. a) Flow cytometric distribution from the cell mixture before ASL and b) Flow cytometric data of GFP-positive cells after ASL.

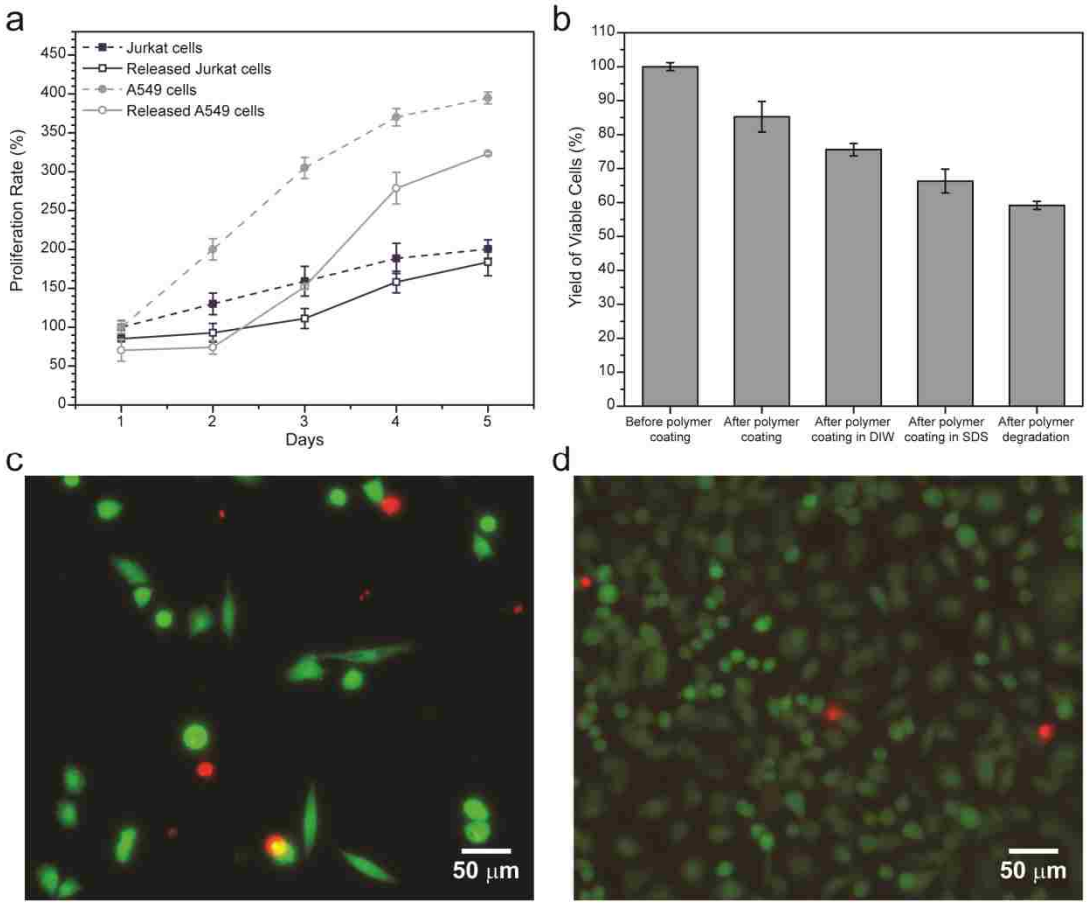

Figure 5.7: Proliferation and viability of processed cells. a) Proliferation rates of naive (dashed line) or processed/released (solid line) cells. Jurkat cells (blue). A549 cells (grey). b) Viability of Jurkat cells at critical steps in Antigen Specific Lysis processing. Data are mean ± s.d. Calcein staining (green) images of released A549 cells after polymer degradation after: c) 1 day and d) 4 days of culturing. The presence of red fluorescence indicates regions of residual red fluorescent nanoparticle-loaded polymer.

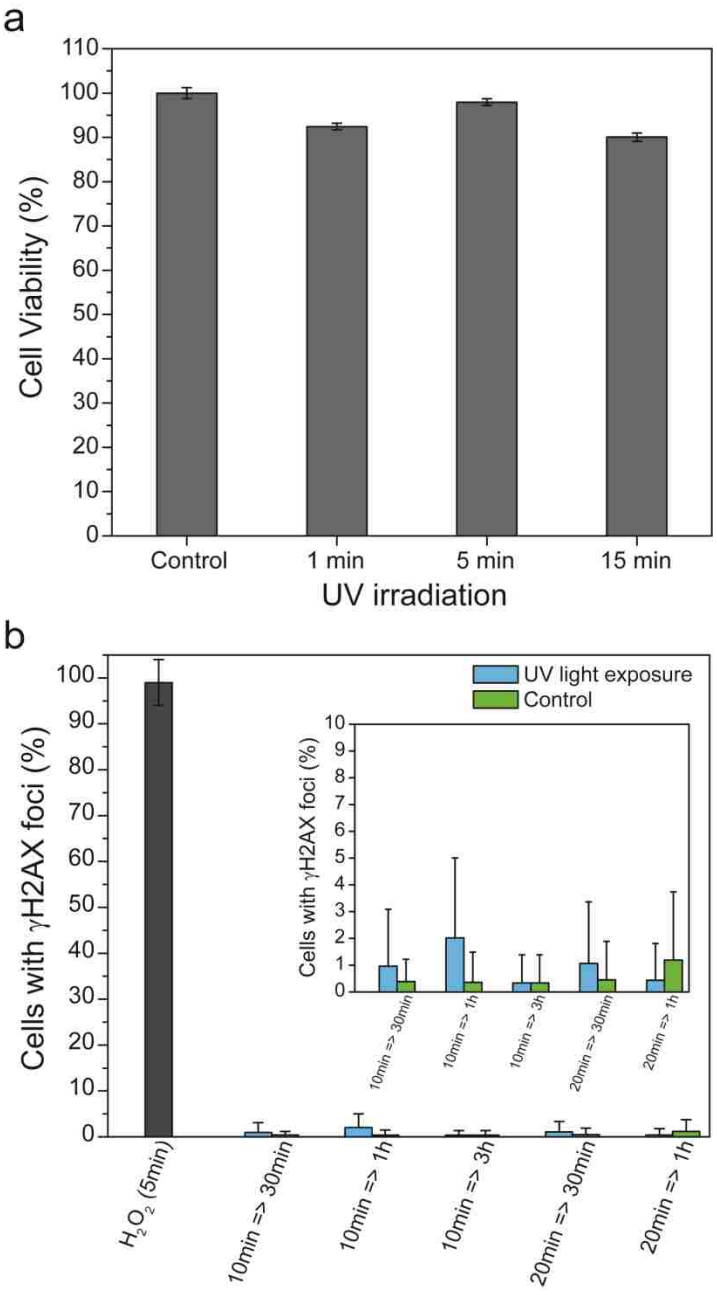

Figure 5.8: UV irradiation effect on cell viability. a) Cell viability determined by MTT assay after 365 nm, 10 mW/cm^2 light exposure over time. b) DNA repair activity in A549 cells after UV irradiation (365 nm, 10 mW/cm^2). Activity correlated to fraction of cells displaying ɣH2AX foci. X-axis indicates "[UV exposure time] => [recovery time prior to analysis]". Inset provides an expanded y-axis. H_2O_2 condition was 5 minutes of 0.2 mM H_2O_2 and measured 30 minutes post exposure. Data are mean ± s.d.

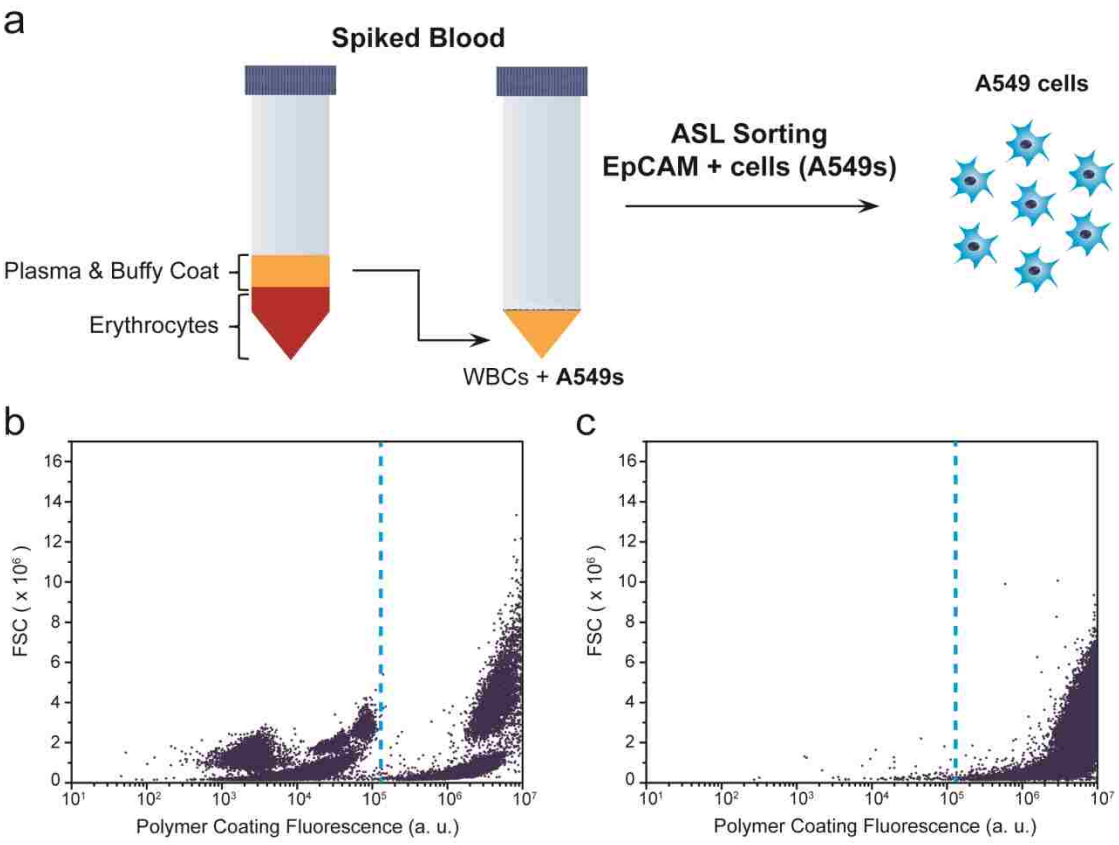

Figure 5.9: Isolation of EpCAM+ cells spiked into blood. a) Overview of approach. b) Flow cytometric data of A549 cell spiked into erythrocyte-depleted blood after EpCAM-specific polymerization. Dashed line indicates distinction between polymer coated A549 cells and other blood components based on control studies of pure populations. c) Flow cytometric data after lysis of EpCAM- components.

Chapter 6: Quantitative Investigation of Surface Receptor Expression Density For The Isolation of Tumor Cells

In this chapter, expression levels of common cancer markers are quantitated for three breast cancer and two non-small cell lung cancer lineage models. These levels are contrasted with that present on healthy peripheral blood mononuclear cells for comparison to expected background levels in a fluid biopsy setting. A key feature of this work is establishing a metric of markers per square micrometer. This describes an average marker density on the cell membrane surface, which is a critical metric for emerging isolation strategies. These results serve to extend expression of key tumor markers in a sensitive and dynamic manner beyond traditional "positive"/"negative" immunohistochemical staining to guide future fluid biopsy targeting strategies. The work presented here is adapted with minor modifications from work previously published:

> Calvin F. Cahall, Jacob L. Lilly, Edward A. Hirschowitz, Brad J. Berron. A Quantitative Perspective on Surface Marker Selection for the Isolation of Functional Tumor Cells. Breast cancer: Basic and Clinical Research. 9(Suppl 1):1, 2015.

6.1 Introduction

Much effort has gone into developing fluid biopsies of patient peripheral blood for the monitoring of metastatic cancers. One common approach is to isolate and analyze tumor cells in the peripheral blood [6, 8]. Widespread clinical implementation of this approach has been hindered by the current choice of targeting epithelial markers known to be highly variable in primary tumor sites [4]. Marker-targeting isolation strategies are intrinsically dependent on the level of antigen expression presented on target cells. Low

quantities, and more specifically low densities, of the target marker will decrease the net binding recognition of antibodies to a marker positive cell surface, potentially leading to poor discrimination between positive and negative events [4, 12]. Critically, the current literature poorly describes the expression of even the best known tumor markers on the most commonly studied tumor cell lines. Typically, the expression of a marker is communicated as positive or negative. At best, papers will communicate relative levels in terms of dim, moderate, bright, or variable. Alternatively, the level of receptor expression is given as moles of receptor per mass of cell lysate. Techniques that have been used to detect cell antigens qualitatively and quantitatively include enzyme immunoassay (EIA) and enzyme-linked immunosorbent assay (ELISA) [142, 143]. However, these techniques that quantify expression on a total mass basis are minimally useful in the development of viable cell sorting, as they report antigens that may be present only intracellularly and unavailable for targeting on an intact, viable cell [144, 145].

Herein, we seek to quantify the *surface* expression level of these critical markers on common cell lines. This work represents a critical step in assessing the opportunities and limitations of isolating functional tumor-associated cells from peripheral blood. We have chosen tumor cell lines, as the majority of clinical research has centered on the utility of finding epithelial cells in circulation. Finally, we discuss the significant limitations of using these *in vitro* cell models for CTCs in the study of rare cancer cell biology.

6.2 Materials and Methods

6.2.1 Cell Culture

Three breast cancer cell lines and two non-small cell lung cancer (NSCLC) cell lines were cultured. Breast cancer lines included MDA-MB-231 (mammary adenocarcinoma), MCF-7 (mammary adenocarcinoma), and T-47D (mammary ductal carcinoma), and NSCLC lines included A549 (alveolar adenocarcinoma) and H358 (bronchioalveolar carcinoma). All tumor lines were cultured in RPMI-1640 growth medium (HyClone) supplemented with 2.05 mM L-glutamine, 10% fetal bovine serum (FBS, Fisherbrand), and 1% penicillin-streptomycin (Sigma Aldrich), and maintained at 5% CO_2 in air and 37 ˚C. Cells were cultured for 48 hours and were approximately 60-80% confluent just before experimentation. Additionally, a peripheral blood control sample was obtained with informed consent through University of Kentucky Medical Center IRB protocols and processed within an hour of collection. Briefly, whole blood was mixed with a dextran/NaCl solution to a working concentration of 2 wt% dextran and 0.3 wt% NaCl and was allowed to separate by 1x*g* sedimentation at room temperature for 1 hour. The buffy coat containing peripheral blood mononuclear cells (PBMC) was then pipetted off and exposed to red blood cell lysis buffer (155mM NH_4Cl, 10mM $KHCO_3$, 0.1mM EDTA) for 5 minutes to further remove red blood cells from the sample. The nucleated cells were collected by centrifugation at 300x*g* for 5 minutes and washed twice with cold 1X PBS.

6.2.2 Cell Imaging

Representative bright field, phase contrast images of all tumor cell lines were taken with a Nikon Ti-U inverted microscope.

6.2.3 Surface Marker Immunostaining

Tumor cells were incubated with trypsin/EDTA (0.25%) solution for 3 minutes to allow for detachment, rinsed with growth medium and centrifuged. Cell concentration and cell diameter was determined optically with a Cellometer Automated Cell counter (Nexelcom). Each data replicate sample consisted of $1x10^5$ cells in a microcentrifuge tube. For experimentation, a rinsing buffer of 1X PBS with 3% FBS was prepared and used for all rinsing steps. All materials and cell samples were kept on ice throughout the staining procedure. For immunolabeling, cell samples were first rinsed once with rinsing buffer and centrifuged (400x*g*, 1.5 minutes). Subsequently, samples were incubated with primary antibodies at ~0.5 μg in 150 μl of rinsing buffer for 40 minutes. For all cell lines, markers were targeted with primary monoclonal mouse IgG antibodies with corresponding isotype controls that consisted of: CD326/EpCAM (IgG2b, clone 9C4, BioLegend, San Diego, CA), HER1/EGFR (IgG1, clone AY13, BioLegend), CD44 (IgG1, clone BJ18, BioLegend), E-cadherin (IgG1, clone 67A4, BioLegend), erbB2/HER2 (IgG1, clone 24D2, BioLegend), N-cadherin (IgG1, clone8C11, BioLegend), alphaV-beta3 integrin (IgG1, clone 23C6, BioLegend), ICAM-1 (IgG1, clone HA58, eBiosciences, San Diego, CA), ER-α (IgG2a, clone F-10, Santa Cruz Biotechnology, Dallas, TX). Samples were then rinsed twice with rinsing buffer on ice, with centrifugation between rinses. Cells were then labeled with biotinylated goat anti-mouse IgG antibody (Vector Labs, Burlingame, CA) at a 1:400 dilution in rinsing buffer on ice for 40 minutes. Cells were rinsed twice with rinsing buffer and incubated with streptavidin-phycoerythrin at ~1 μg in 200 μl on ice for 20 minutes. Samples were rinsed three times and resuspended in ~200 μl rinsing buffer for immediate analysis.

6.2.4 Flow Cytometry

Cell sample immunofluorescence was assessed with an Accuri C6 flow cytometer. Samples were kept on ice, then gently vortexed before a cytometry run. For each replicate, 5000 cell events were collected based on initial cell culture control gating. Phycoerythrin fluorescence data was collected for each sample in the FL2 channel configured for excitation with a 488 nm laser and emission detected through a 585/40 bandpass filter.

6.2.5 Data Analysis

Data is calculated as mean ± standard error of the geometric means of event populations (N=3) for all marker quantification assays and cell diameter calculations. Standard deviation within individual replicates of cytometry data is also reported. Quantibrite PE bead calibration was performed during cell immunofluorescence data collection and fluorescence calibration values are collected in channel FL2. Statistical analysis consisted of a two-tailed student t-test performed in Matlab to calculate p-values.

6.3 Results and Discussion

6.3.1 Imaging Analysis

A summary of cell types and corresponding cell sizes is shown in **Table 6.1**. From a regression analysis relating mean forward scatter and mean Cellometer cell size (**Figure 6.1)**, cell diameters of individual populations of lymphocytes, monocytes, and granulocytes were extrapolated. As expected, these PBMC showed diameters smaller than epithelial cancer cells. To estimate cell surface area, a spherical model was assumed for each cell. While some cell types can possess membrane folds that can alter diameter and surface area in certain scenarios (e.g. activation of white blood cells) [146], we posit

this simple model is sufficient to generally show accessible marker densities on the surface of the cells studied here. For morphological comparison, representative bright field images of tumor cell lines are shown in **Figure 6.2**. The basal-like breast line MDA-MB-231 [147] show morphology quite distinct from any other investigated in the study, with elongated, multi-polar behavior and favoring minimal cell-cell contact consistent with basal subtypes. Luminal breast lines MCF-7 and T-47D [148] and NSCLC line H358 show morphology more consistent with an epithelial phenotype favoring extensive cell-cell contact and colonization. NSCLC line A549 appears to exhibit behavior somewhere between these extremes with less organized cell junctions.

6.3.2 Quantitation of Marker Expression by Flow Cytometry

The results of marker quantitation using the flow cytometric Quantibrite assay are presented in **Figures 6.3 and 6.4**, where Phycoerythrin fluorescence signal serves a reporter for antigen quantity. Expression data is presented here both as expression fold over isotype controls as well as normalized to the calculated mean surface area for each cell type. Because we employed an indirect immunostaining approach, some labeling amplification inherent in antibody binding interactions was seen. A biotin anti-EpCAM primary was labeled in parallel to biotin-anti-mouse secondary staining, with only a ~1.3-fold amplification seen for secondary immunolabeling. Further, we also expect some amplification at the biotin/SA-PE labeling interaction. Although this may skew the representation of the actual number of biological copies of these surface proteins, the focus of our study was to provide a methodology engineering perspective on the maximum level of antigen affinity recognition afforded by traditional immunolabeling for

viable CTC isolation, where some amplification is not only acceptable but desired. Moreover, as all markers were tagged with identical indirect staining approaches, relative expression across cell lines and between markers should be consistent regardless of any labeling amplification.

Overall, marker expression levels often varied drastically between cell lines with some correlation seen between cell morphology, behavior, and marker profiles. Specifically, MDA-MB-231 showed significantly decreased PE labeling density for EpCAM and E-cadherin compared to MCF-7, T-47D, and H358 (p-values<0.001), while showing higher levels of labeling density for CD44, EGFR and ICAM-1 (p-values≤0.01, **Figure 6.4**). A549 also showed decreased EpCAM and E-cadherin density (p-values<0.001) and increased CD44 density over MCF-7, T-47D, and H358 (p-values<0.01). EGFR and ICAM-1 expression seemed to be consistently high, resulting in PE label densities equal to or greater than 100 per μm^2 for all cell lines except MCF-7. EGFR has been linked to a basal-like molecular signature [149], and elevated levels of EGFR and ICAM-1 have been linked to metastatic disease [150, 151]. The αV-β3 integrin is elevated 10-fold in MDA-MB-231 cells compared to the other tumor lines investigated (p-values<0.001), with ~30 PE molecules per μm^2. Of particular interest for breast cancer lines was ERα and HER2 expression because of their prominent clinical role in breast cancer classification, prognosis and therapy selection. The antibody chosen (clone F-10, Santa Cruz) targeted the c-terminus ligand binding domain. All three breast cancer lines showed a slight increase in ERα expression over isotype controls (p-values<0.05, **Figure 6.3.a-6.3.c**), and a statistical elevation in expression over NSCLC lines (p-values<0.05) which showed virtually no ERα expression, with the exception of

MCF-7 compared to A549 (p=0.15, **Figure 6.3.d, 6.3.e**). HER2 expression was expressed at relatively high levels in all three breast cancer lines as well as NSCLC lines, resulting in roughly 50-100 PE molecules per μm^2 (**Figure 6.4**).

Our study also sought to provide background expression levels on PBMC for comparison, as it is ultimately a determining factor in marker selection for isolating CTCs from peripheral blood. **Figure 6.3.f** shows marker expression fold over IgG for separately gated lymphocyte, monocyte, and granulocyte populations. Notably, relatively elevated levels of both CD44 and ICAM-1 are seen. In **Figure 6.4.f**, the PE binding density is reported for PBMC, showing high non-specific noise in isotype controls, especially for monocytes. This immunolabeling noise can reduce the biorecognition contrast between the target tumor cells for capture and the majority PBMC, so here we further demonstrate the PE labeling density fold vs peripheral blood monocyte expression, which represent the most likely culprits for false-positive capture (**Figure 6.5**). First, MDA-MB-231 showed drastically attenuated EpCAM (p=0.0038) and E-cadherin (p=0.90) elevation over monocytes due to low expression seen in **Figure 6.4.a**. EGFR contrast remains high for MDA-MB-231 and NSCLC lines (p-values<0.01). Although CD44 and ICAM-1 were highly expressed across all cancer lines in the study, the contrast over blood cells is reduced because of corresponding high expression in PBMC. MDA-MB-231 have a slight CD44 contrast over monocytes, and MDA-MB-231 and A549 both retain high contrast for ICAM-1 expression (p-values<0.01). Finally, N-cadherin and αV-$\beta 3$ integrin expression on all five cancer lines investigated shows little to no elevation over that of peripheral monocytes.

Here, we have reported quantitative results of levels of antibody-mediated recognition attained for several commonly investigated markers associated with metastasis on both breast cancer and NSCLC lines. To our knowledge, very little information is reported on the numbers of marker proteins present on cancer cell membrane surfaces. While many fundamental biology questions can be answered with immunohistochemical and blotting assays that yield binned "positive" or "negative" information, these approaches generally fail to represent the highly dynamic and variable expression patterns seen for many tumor cells [31, 145, 152]. Particularly for antibody-based cell isolation methodologies, the ability to capture a marker-presenting cell amongst a majority of marker-negative cells is critically dependent on the amount of marker proteins available on the cell surface for labeling. In this light, we propose these findings represent a significant step toward providing the tumor cell isolation community with quantitative antigenic expression information.

Notably, our results show distinct expression signatures for basal and luminal breast cancer subtypes consistent with the characteristics commonly associated with each. Basal-like cells are often seen to be more highly invasive and de-differentiated, while luminal-type cells are often considered epithelial-like [148, 149]. MDA-MB-231 are classified as basal, whereas MCF-7 and T-47D are luminal A subtypes. We found that MDA-MB-231 showed elevated levels of mesenchymal and/or metastatic markers CD44, N-cadherin, αV-β3 integrin, ICAM-1, as well as upregulation of EGFR commonly seen for basal subtypes (**Figure 6.3.a**) [149]. Further, the basal-like MDA-MB-231 also showed lower expression of epithelial markers EpCAM and E-cadherin compared to MCF-7 and T-47D (**Figure 6.3.a-6.3.c**). Elevated levels of mesenchymal markers have

been linked to a more metastatic phenotype, as these proteins play key functional roles as tools for migration and invasion [18]. In the context of CTC isolation that currently is predominantly based on EpCAM+ sorting, these results highlight a disconnect between marker targeting strategy and the biologic tendencies of highly invasive cells. Specifically, a detection threshold of EpCAM expression exists for any antibody-based isolation methodology, and highly-invasive cells downregulate EpCAM and have a higher potential to go "unseen" as false negatives.

A surprising result was also seen for ERα expression in comparing the basal (MDA-MB-231) and luminal A (MCF-7 and T-47D) subtypes in the study. All three cell lines showed a similar expression of HER2, which was not unexpected for basal and luminal A subtypes that generally do not have overexpression of HER2 [148]. However, we found that MDA-MB-231 cells also expressed similar surface densities of ERα compared to MCF-7 and T-47D. One possible explanation could be that because our focus was to determine antigen densities on intact tumor cell surfaces, the antibody chosen for ERα targeting (clone F-10, Santa Cruz Biotech) targeted the C-terminal ligand binding domain; however, these nuclear receptors are often trafficked intracellularly.[153] Therefore, these results do not account for intracellular ERα where differences in expression between basal and luminal A subtypes could arise.

Our study also sought to offer some order-of-magnitude perspective on expression levels of surface markers CD44, N-cadherin, αV-β3 integrin and ICAM-1 implicated in metastatic progression [150, 154, 155], as these could potentially serve as promising new targets for sorting clinically relevant cells. A poorly expressed molecule may play an important role biologically, but would be of minimal utility as a target for live cell

isolation. Furthermore, a molecule may even be highly expressed, but if it is also highly expressed on peripheral blood cells, it would no longer serve to distinguish epithelial identity from the background blood cells. PBMC marker expression was normalized to cell size similarly to epithelial cells, and PBMC size estimates were found to be in fair agreement with literature [156, 157]. We found that although both N-cadherin and αV-β3 integrin were upregulated on some lines (MDA-MB-231 and A549), their inherent expression density was still approximately equal to or below the expression found on peripheral monocytes, which consistently showed the highest background staining levels(**Figures 6.4.f and 6.5**). Additionally, while CD44 was relatively high for all cancer lines (**Figure 6.4**) it was also highly expressed in PBMC which reduced the expression ratio over monocytes to nearly 1 or below for all lines except MDA-MB-231 that retained a 7-fold ratio over monocytes (**Figure 6.5**). Therefore, because our results show minimal differences in expression of these markers over blood cells, they are not recommended for targeting intact tumor cells. It is worth noting though that more work is warranted in quantitating the extent of elevation of markers like N-cadherin shown to undergo a "cadherin switch" from stromal cytokine stimulation *in vivo* [158, 159]. This phenotypic transition is correlated with a more invasive cell and could conceivably potentiate N-cadherin as a target for tumor cell isolation. ICAM-1 expression density was seen to be approximately 30- to 60-fold higher than monocytes for T-47D and MDA-MB-231, respectively (**Figure 6.5**). ICAM-1 is involved in cell adhesion interactions, migration, and has been recently been classified as a mesenchymal cell marker [160-162]. Further, one recent study has shown that increased populations of ICAM-1^{high} CTCs correlated to poorer prognosis in hepatocellular carcinoma patients [150]. Coupled with these findings,

our results point toward ICAM-1 as a potential target for isolation of clinically relevant tumor cells.

6.4 Conclusions

We have reported surface marker densities on several model tumor cell linages to guide the development of isolation methodologies for live and functional CTC populations. The surface density of targeted markers is a critical parameter for any antigen-based CTC capture platform, and likely represents a key oversight that has led to poor performance of many previously developed technologies. Our results also indicate extreme variability in expression between markers and cancer cell lines, and illustrate the need for greater appreciation of heterogeneity at the surface marker level across different cancer subsets. While **Figure 6.3** and **Figure 6.4** are presented as mean with standard error of mean, **Figure 6.6** also shows that the variance in immunofluorescence for cell events within each replicate was often considerably higher. This could be due in part to the inherent variability within the cultured cell population, as well as due to deviations from a mean K_d for each antibody used. As with any antibody based assay, the variance in antibody binding affinity from different suppliers should be carefully considered when interpreting these data as well as in designing an antibody-based isolation strategy. Further, cancer heterogeneity has also been widely reported for in vivo settings [152, 163]. Cytokine signaling and tumor-stromal interactions can cause certain subsets of malignant cells to display drastically altered marker profiles, some resembling stem-like phenotypes in what is referred to as epithelial-mesenchymal transition [1]. These highly potent subsets have been reported to go largely unnoticed in EpCAM+ based CTC isolation strategies, leading many to suggest that perhaps EpCAM alone is not sufficient

to capture any and all CTCs [12, 164]. Our findings further support that EpCAM surface presentation cannot be assumed to be similar for all tumor lines, and more comprehensive targeting strategies that account for expression level variability is warranted. One possible strategy would be to use panels of antibodies to target several tumor markers to ensure successful capture in instances where certain markers are downregulated. For example, Yu et al. targeted patient-derived breast CTCs with a cocktail of EpCAM, EGFR, and HER2 antibodies in a microchip device approach, where subsequent fluorescent immunostaining of captured cells revealed they possessed highly variable and dynamic phenotypes with both epithelial and mesenchymal markers [31]. Building upon these types of robust targeting strategies will be vital for developing future generations of more clinically relevant fluid biopsy technologies.

Table 6.1: Summary of cell types analyzed in the study. Diameter and surface area calculations are reported as mean ± s.e.m.

Cell Type	Description	Diameter (µm)	Surface Area (μm^2)
MDA-MB-231	mammary adenocarcinoma	11.5 ± 0.3	415 ± 19
MCF-7	mammary adenocarcinoma	17.1 ± 0.4	922 ± 43
T-47D	mammary ductal carcinoma	14.5 ± 0.3	663 ± 34
A549	alveolar adenocarcinoma	15.0 ± 0.4	710 ± 38
H358	bronchioalveolar carcinoma	16.8 ± 0.5	890 ± 47
Peripheral Lymphocytes	Healthy PBMC	6.7 ± 0.1	142 ± 1
Peripheral Monocytes	Healthy PBMC	7.9 ± 0.1	197 ± 2
Peripheral Granulocytes	Healthy PBMC	8.2 ± 0.1	209 ± 1

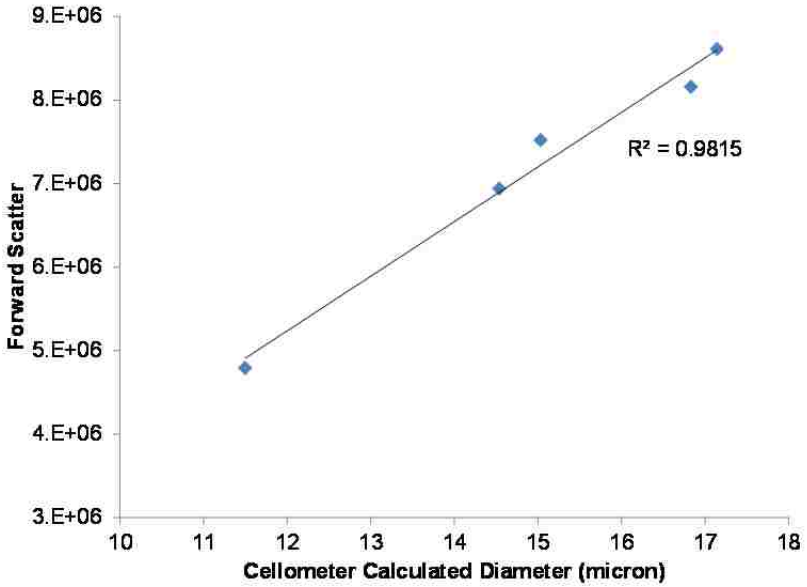

Figure 6.1: Plot of regression analysis relating mean forward scatter vs. mean Cellometer cell diameter for all five cancer lines.

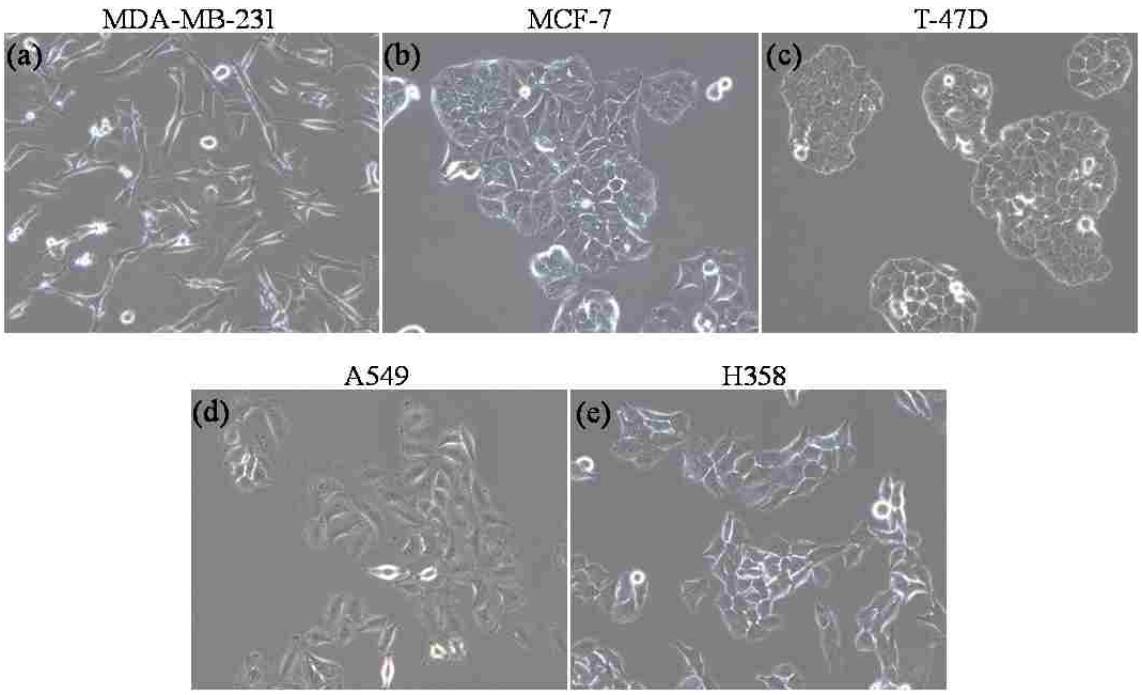

Figure 6.2: Representative bright field micrograph images of cultured breast cancer lines (MDA-MB-231, MCF-7, T-47D) and non-small cell lung cancer lines (A549, H358).

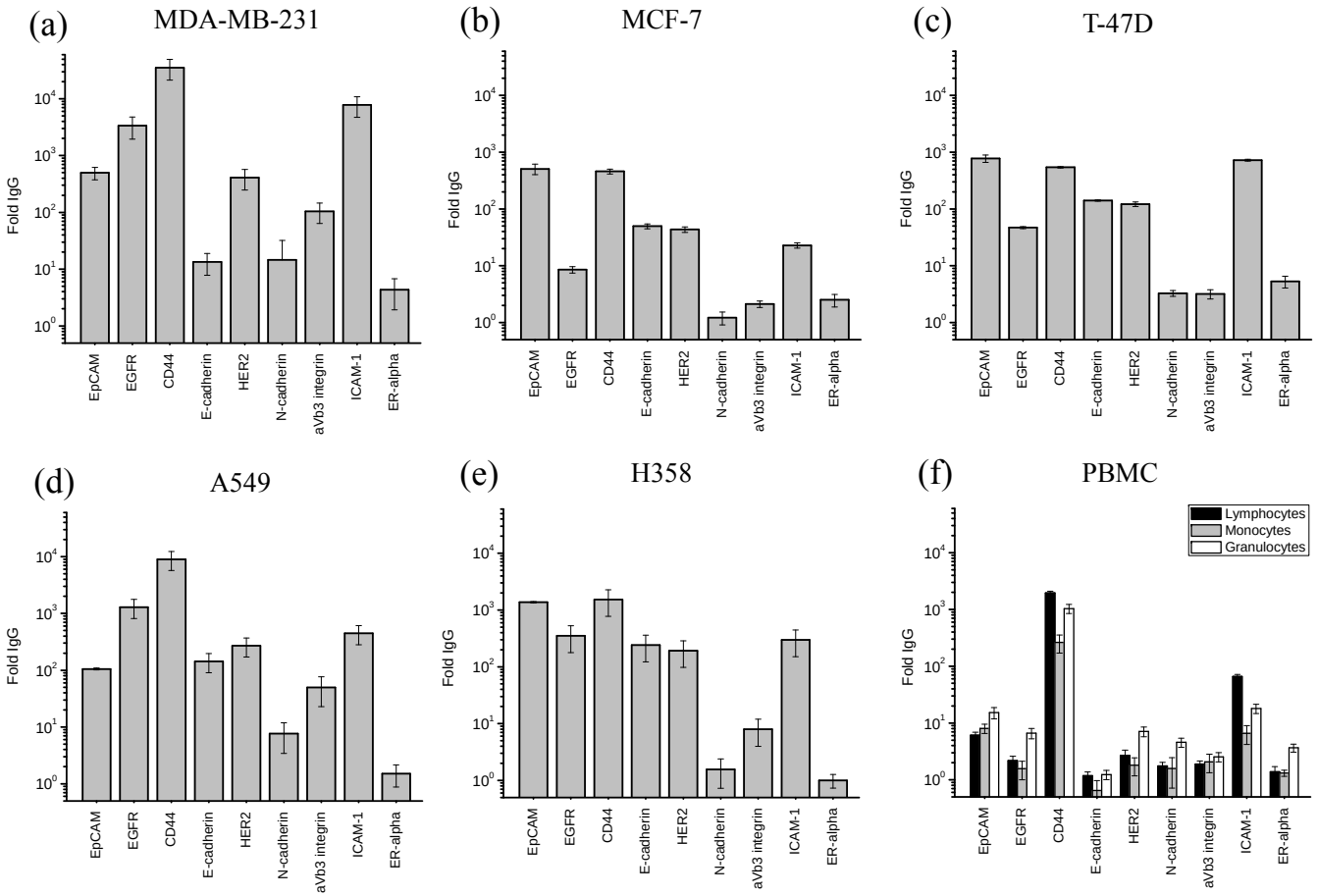

Figure 6.3: Summary of tumor marker expression on viable cells. Presented as fold over isotype controls for cancer lines and healthy peripheral blood mononuclear cells (PBMC) as quantified by flow cytometry analysis of a phycoerythrin reporter label. All data reported as mean ± s.e.m.

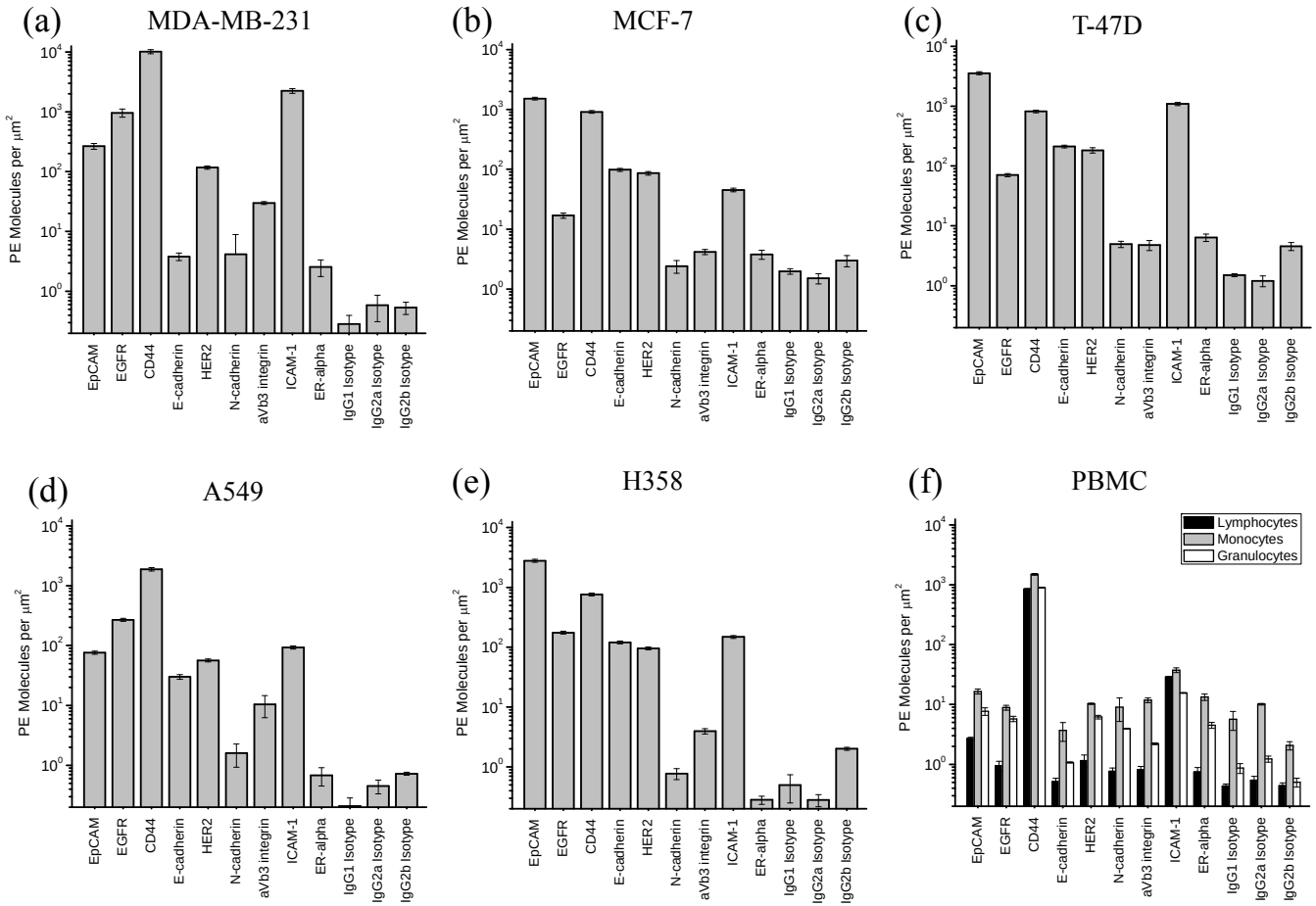

Figure 6.4: Summary of Phycoerythrin labeling density (# PE molecules per μm^2 of cell surface) for various tumor marker targeting conditions on viable cancer line cells and healthy PBMC. All data reported as mean ± s.e.m. Corresponding antibody isotypes are – IgG1: EGFR, CD44, E-cadherin, HER2, N-cadherin, aVb3 integrin, ICAM-1; IgG2a: ER-alpha; IgG2b: EpCAM.

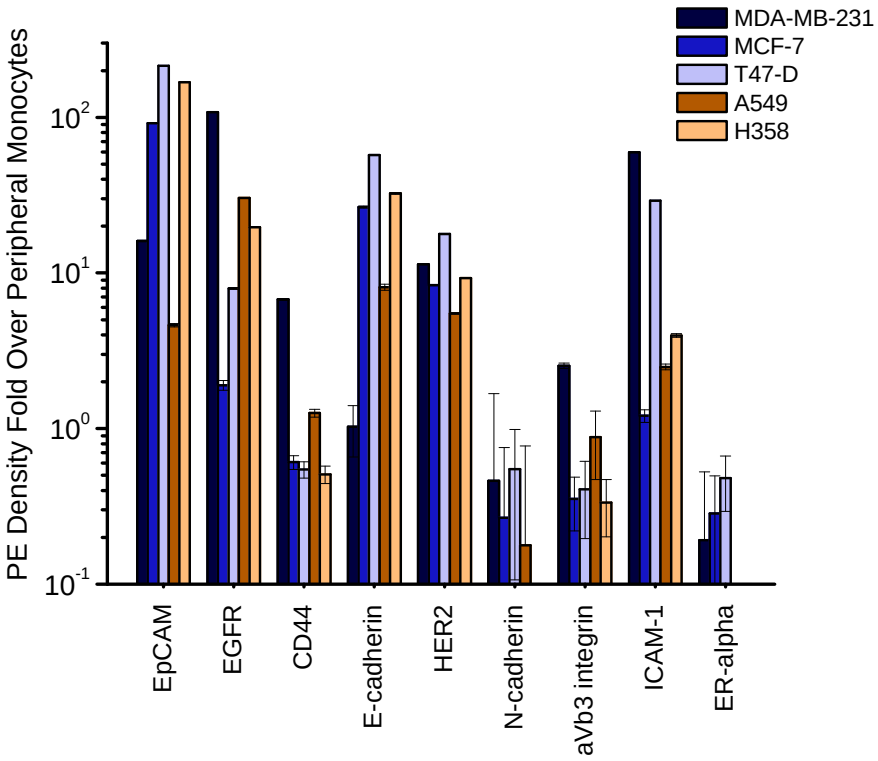

Figure 6.5: Summary of phycoerythrin labeling density of all cancer lines studied presented as fold expression over healthy monocytes from a peripheral blood sample. Data reported as mean ± s.e.m.

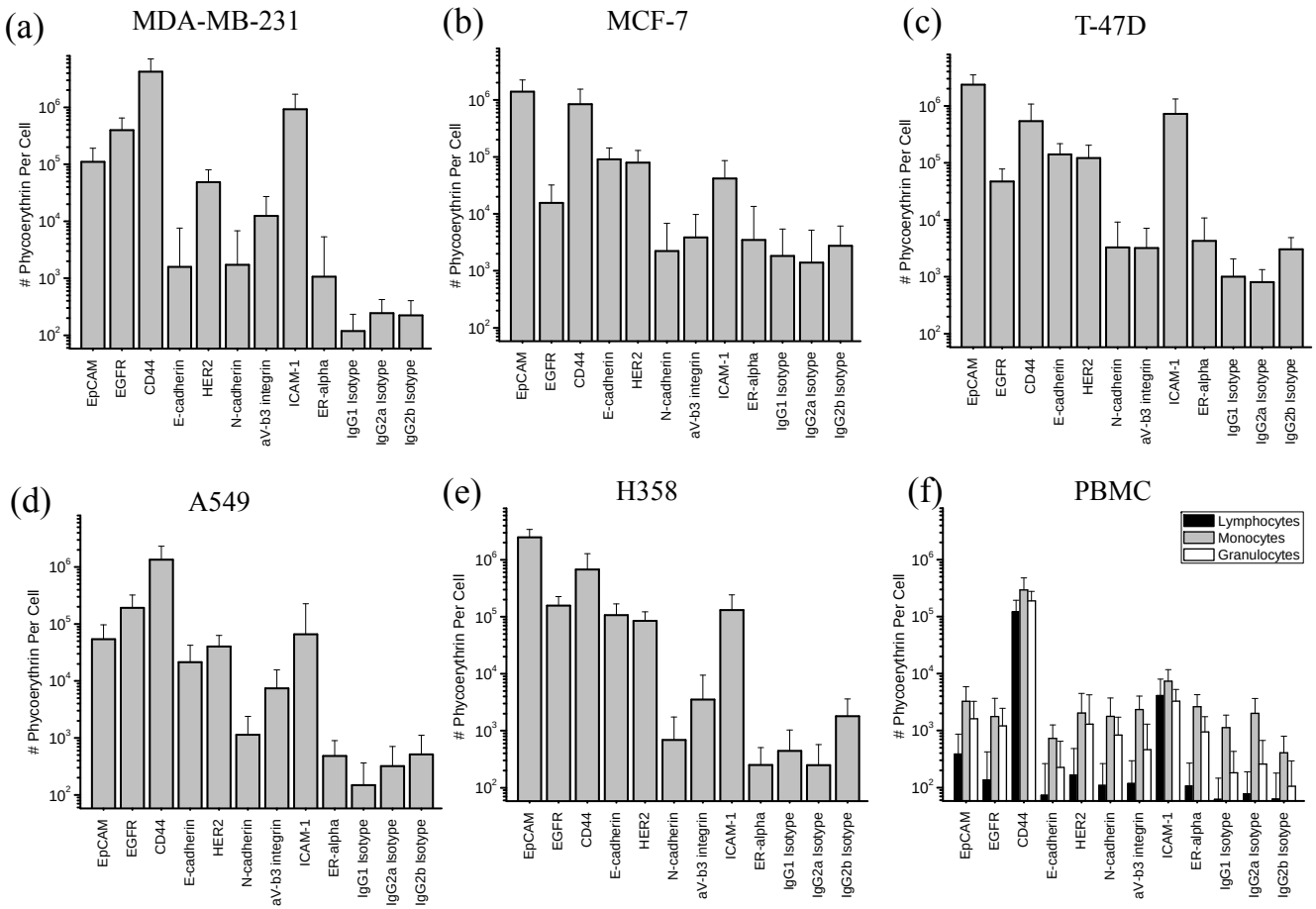

Figure 6.6: Summary of phycoerythrin labeling per cell for all markers and cell types. Error bars represent the standard error of events collected by flow cytometry. Corresponding antibody isotypes are – IgG1: EGFR, CD44, E-cadherin, HER2, N-cadherin, aVb3 integrin, ICAM-1; IgG2a: ER-alpha; IgG2b: EpCAM.

Chapter 7: The Role of Surface Receptor Density in Surface-Initiated Polymerizations for Cancer Cell Isolation

In this chapter, we demonstrate the labeling density of photoinitiators is strongly correlated with the yield of intact cells during ASL by flow cytometry analysis. Results suggest ASL is fundamentally capable of delivering approximately 50-60% of targeted cells after isolation, which rivals competing methodologies. The gelation response during ASL polymerization is also investigated via protein microarray analogs on planar glass. Finally, a density threshold of photoinitiator labeling required for protection during lysis is determined for both monomer formulations. These results indicate ASL is a promising technology for high yield CTC isolation for rare-cell function assays and fluid biopsies. The chapter presented here is adapted with minor modifications from the following work currently in review:

Jacob L. Lilly, Brad J. Berron. The Role of Surface Receptor Density in Surface-Initiated Polymerizations for Cancer Cell Isolation. Langmuir, *In Review*.

7.1 Introduction

Fluid biopsies potentially offer a minimally invasive alternative to traditional tissue biopsies for the continual monitoring of metastatic cancer [33, 165]. Current established technologies for isolating circulating tumor cells (CTCs) suffer from poor purity, yield, and require fixatives that preclude the collection of viable cells for longitudinal analyses of biological function. Antigen Specific Lysis (ASL) is a rapid, high-purity method of cell isolation based on targeted protective coatings on antigen-presenting cells and lysis depletion of unprotected antigen-negative cells. In ASL, photoinitiators are specifically labeled on cell surfaces that enable subsequent surface-

initiated polymerization. (See **Appendix A-5** for details on cell protein specificity) While we have shown ASL delivers viable (~90%) and highly pure (>97%) populations of marker-presenting cells, cell yield has yet to be fully investigated for this process. For CTC sorting, target cells exist in extreme rarity (~1 per 10^6 nucleated cells). Increasing isolation yield will minimize the occurrence of false negatives and potentially provide the key difference for an accurate diagnosis. Further, for any antigen-based isolation platform, successful positive capture of cells is inherently dependent on the density of surface markers available for targeting. For ASL, the surface density of markers dictates the concentration of eosin photoinitiators present at the cell surface. A distinct threshold eosin density has been previously reported for surface-mediated polymer amplification assays, below which radical generation is not sufficient for gelation [92, 125]. Therefore, we hypothesize a minimum density of antibody-photoinitiator binding is required to form complete protective coatings.

Herein, we investigate the effect of photoinitiator loading on polymerization and lysis-based negative depletion of cells. (**Figure 7.1**) A non-small cell lung cancer line (A549) serves as a model CTC. To eliminate heterogeneity in surface marker clustering, our investigation first nonspecifically biotinylates the cell surfaces for polymer protection studies. This approach allows for more consistent biotin functionalization and limits the potential for signaling activation that targeting a specific marker might enact, which could influence our results. We then shift to the more clinically relevant antibody-based strategies, targeting either EpCAM or a panel of metastatic markers for comparison to our covalent labeling approach. Finally, we relate the density dependent protection to thin film polymerization behavior on an analogous system of biotin-functionalized protein

microarrays. These glass microarrays afford a controlled environment to quantitatively determine the gelation response to the photopolymerization conditions used in the cell studies.

The impact of this study extends beyond our new lysis isolation process to the field of immunoprotective coatings on cells. Immunoprotection requires a complete polymer barrier to isolate the non-native cellular material from a host's immune response. Several groups are utilizing nano- and micro-scale polymers to isolate individual cells from immune response [54, 166-170]. As the thickness of these materials decreases, the diffusive flux of oxygen and low molecular weight nutrients increases. Critically, as the coating thickness approaches the diffraction limit of light, it is increasingly challenging to visually verify the completeness of the coating. This study uses surfactant lysis as a new approach to cheaply and quickly verify the completeness of the coating.

7.2. Materials and Methods

7.2.1 Reagents and Materials

The A549 cell line (non-small cell lung cancer) was purchased from American Type Culture Collection. RPMI-1640 culture media, penicillin/streptomycin (1%), and trypsin/EDTA (0.25%) were supplied by Gibco™. Advantage-grade fetal bovine serum (FBS) was purchased from Atlanta Biologicals. Lyophilized streptavidin, streptavidin-Cy3 conjugate, biotinylated bovine serum albumin (b-BSA), sulfo-NHS-LC-biotin, CellTracker™-Deep Red dye, Hoechst 33342 stain, and yellow-green FluoSpheres™ nanoparticles (0.02μm, carboxylate-terminated, 505/515nm excitation/emission) were purchased through Thermo Fisher Scientific. Bovine serum albumin (BSA), Polyethylene glycol diacrylate (M_n~575), Polyethylene glycol (M_n~3400), monomer MEHQ dehibiting

columns, 1-vinyl-2-pyrrolidinone, acryloyl chloride, triethylamine, Eosin-5-isothiocyanate (EITC), sodium dodecyl sulfate (SDS) were all supplied from Sigma Aldrich. Triethanolamine (TEA), dichloromethane (DCM), and diethyl ether were supplied by Fisher Chemical. DNase I (>500U/mg, from bovine pancreas) was supplied by Biomatik. Monoclonal antibodies against EpCAM (IgG2b, clone 9C4), CD44 (IgG1, clone BJ18), and HER1/EGFR (IgG1, clone AY13) were purchased from BioLegend, and anti-ICAM-1 (IgG1, clone HA58) was purchased from eBiosciences. Biotinylated goat anti-mouse IgG antibody was purchased from Vector Labs. Streptavidin R-phycoerythrin conjugate was purchased from Anaspec. The QuantiBRITE phycoerythrin (PE) fluorescence flow cytometry quantitation kit was supplied by BD Pharmingen.

7.2.2 Monomer Synthesis and Preparation

Polyethylene glycol diacrylate (M_n~575, PEGDA-575) was twice flowed by gravity through a dehibiting column to remove the polymerization inhibitor monomethyl ether hydroquinone, and stored for use protected from light at room temperature. Polyethylene glycol (M_n~3400) was dissolved in DCM and reacted with acryloyl chloride and triethylamine according a previously published protocol [171]. Monomer product purity (~90% acrylation yield) was confirmed by ^{1}H-NMR and was stored at 80% (w/v) in water protected from light. Co-monomer 1-vinyl-2-pyrrolidinone was used as received.

7.2.3 Photoinitiator-Protein Conjugation

The conjugation reaction to label eosin-5-isothiocyanate to streptavidin primary amines was adapted from a previous protocol with only a minor protocol modification of reacting at pH 10 in 0.1 M carbonate/bicarbonate buffer [98]. Conjugates were purified

with a 5 mL 7 KDa MWCO Zeba desalting column and the molar ratio confirmed with UV-vis analysis of absorbances at 280nm and 530nm. (see **Appendix A-2 and A-3**)

7.2.4 Cell Culture and Fluorescent Labeling

A549 cells were cultured in RPMI-1640 supplemented with 10% FBS and 1% penicillin/streptomycin at 37˚C and 5% CO_2 for approximately 48 hours. Cell flasks were 75-90% confluent at the time of experimentation. To harvest the A549 cells, the culture media was removed and the cells were washed with 37˚C sterile phosphate buffered saline (PBS 1X). Trypsin/EDTA (0.25%) was added to each flask and incubated for 3-5 minutes. Fresh culture media was added to the flask and gently rinsed by pipetting to detach cells. The cell suspension was then centrifuged at ~500*g* for 3 minutes and the supernatant discarded. The cell pellet was resuspended in fresh media and immediately stored on ice. To begin fluorescent labeling cell samples, cells were first centrifuged at 500*g* for 1.5 minutes at 4˚C and resuspended in cold PBS by gentle vortexing. Initial cell counts from culture were obtained by flow cytometry using an Accuri C6 cytometer and adjusted to $1x10^6$ per sample tube. Cells were rinsed in cold PBS twice more, then resuspended by vortexing in 0.5 μM CellTracker™-Deep Red in cold PBS and incubated for 30 minutes on ice. Samples were then rinsed three times with cold PBS as before. Experiments investigated two groups: covalently biotinylated cell samples and antibody immunolabeled samples.

For covalent biotinylation, cells were incubated with 1 mM sulfo-NHS-LC-biotin prepared in cold PBS for 30 minutes then rinsed three times with cold PBS. Cells were then rinsed once more with PBS supplemented with 3% FBS in PBS (PBS/FBS) and incubated for 10 minutes on ice. To predictably and incrementally vary photoinitiator

loading while keep covalent biotinylation conditions constant, streptavidin-EITC was combined with unconjugated streptavidin at known and varied ratios with a total streptavidin concentration of 25 μg/mL. Upon contacting with cells for 30 minutes, the proteins competitively bound to biotin sites, allowing for photoinitiator (eosin) to be reliably loaded at desired levels. After rinsing twice with cold PBS, cell count was obtained by cytometry and adjusted to $3x10^5$ cells per sample tube to ensure consistent cell density during cell photopolymerization.

For antibody labeling of samples, cells were incubated with primary antibodies (anti-EpCAM or a "metastatic" cocktail of anti-CD44, anti-ICAM-1, and anti-EGFR) consisting of 0.5 μg of each antibody in 100 μL PBS/FBS for 40 minutes, then rinsed three times in PBS/FBS. Cells were then resuspended in 1:400 dilution of biotinylated goat anti-mouse IgG antibody in PBS/FBS for 40 minutes, and rinsed again three times with PBS/FBS. After the biotinylation by immunolabeling, samples were incubated with 25 μg/mL SA-EITC for 30 minutes protected from light. After rinsing twice with cold PBS, cell count was obtained by cytometry and adjusted to $3x10^5$ cells per sample tube to ensure consistent cell density during cell photopolymerization. A negative labeling control was also performed for each monomer formulation that consisted of A549 cells incubated with 25 μg/mL SA-EITC for 30 minutes without prior incubation with biotinylating agents, followed by the polymerization and lysis procedures detailed for biotinylated samples.

7.2.5 Cell Suspension Photopolymerization and Lysis

Polymerization formulations were prepared in PBS consisting of 21 mM TEA, 35 mM VP, with 25% (w/v) of either PEGDA-575 or PEGDA-3500, and 0.05% (w/v)

Fluosphere nanoparticles. All formulations were adjusted to pH~7.5 with 1.2 M HCl and purged with humidified, ultra-pure N_2 for 15 minutes just prior to combining with cells. Each sample was polymerized in a sterile cover glass-bottom 35 mm culture dish placed inside a 150 mm culture dish outfitted with purging inlet and outlet ports. (See **Appendix Figure A-1**) The entire system was purged with N_2 for 5 minutes, at which point irradiation light was introduced while continuing to purge, consisting of 30 mW/cm^2 collimated 530 nm light (ThorLabs LED lamp) for 10 minutes. Lysing solutions were prepared in two parts: (1) DNase I solution of 5 mM $MgCl_2$, 1 mM $CaCl_2$ and 500 U DNase I in PBS, (2) 10% SDS in PBS. Lysing in the presence of DNase minimizes cell clumping due to free DNA in solution. After polymerization and rinsing, each cell pellet was gently resuspended in 500 μL of solution (1) and incubated for 5 minutes at room temperature, followed by addition of 500 μL of solution (2).

7.2.6 Flow Cytometry and Cell Fluorescence Analysis

Cell samples were analyzed during the isolation process just before addition of polymerization solution and after the lysis procedure to calculate the percent yield. To obtain a cell count before polymerization, each sample was redistributed evenly in 10 mL of cold PBS, and then 150 μL of the suspension was pipetted off for analysis. Cytometer fluidics were set to analyze 100 μL of the sample volume. "Positive" cell counts were defined from controls as FL4+ (CellTracker-Deep Red) and FSC$\geq$2x10^6 (intact cell). (see **Figure 7.2**) Additionally, the FL1 channel was monitored in this gated population to determine the SA-EITC loading corresponding to each sample. Identical run constraints and gating were imposed after lysis to monitor yield. In parallel experiments, streptavidin-PE conjugates were also reacted with covalently biotinylated A549

populations at identical conditions to streptavidin-EITC binding experiments at various loading levels to calibrate FL2 of streptavidin-PE loaded samples vs. FL1 of SA-EITC loaded samples. Samples of 10,000 events were analyzed by flow cytometry and the FL2 mean fluorescence of SA-PE tagged samples was plotted vs. FL1 of identically biotinylated SA-EITC samples, shown in **Figure 7.3.a**. BD QuantiBRITE PE quantitation beads were then used to quantify PE fluorescence by vortexing in 500 μL PBS and analyzing in the FL2 channel to calibrate PE binding on biotinylated A549 cells, as shown in **Figure 7.3.b**. The degree of substitution (DOS) of SA-PE and SA-EITC was also determined for fluorescent analysis. The mean DOS of SA-PE was provided by the manufacturer (Anaspec) to be 1.07 phycoerythrin per streptavidin. The DOS of the SA-EITC conjugate was determined by UV-Vis analysis. Standard curves of unconjugated streptavidin and EITC were prepared, allowing for **Equation A-2.1** to be generated that outputs the molar ratio of EITC to SA. The UV-vis of the conjugate used in this study is shown in **Figure A-2**, and the absorbance values at 280 nm and 530 nm were used to calculate a mean DOS of 4.05 eosin groups per streptavidin. Finally, an average cell diameter of 17 μm was determined through automated bright field image analysis with a Cellometer cell counter (Nexelcom) and was used to calculate average cell surface area of 908 μm^2, assuming a perfect spherical cell geometry. Using these data with the fluorescence cytometry calibrations listed above, **Equation 7.1** was developed to determine eosin molecule density from the mean FL1 obtained for each yield experimental trial.

7.2.7 Cell Fluorescent Imaging

A549 cells were imaged after exposure to lysing conditions with a Nikon Ti-U inverted epifluorescent microscope. Cells were incubated with 5 μg/ml Hoechst 33342 stain for 10 minutes, rinsed once with cold PBS and pipetted onto a coverslipped microscopy slide for imaging with a 20x objective. Hoechst DNA staining was imaged with UV excitation, followed by an overlay image of blue excitation to visualize the yellow-green imaging nanoparticles loaded in polymer coatings.

7.2.8 Microarray Fabrication and Hydrogel Film Formation

Epoxy-functionalized slides were washed with ethanol and loaded into an Affymetrix 417 Arrayer. Serial dilutions of bio-BSA and BSA were prepared in PBS, keeping the total protein concentration in solution constant at 1 mg/ml. Biotinylated-BSA concentration was varied to print 12 concentrations (1000, 400, 160, 64, 25.6, 10.2, 4.1, 1.64, 0.66, 0.26, 0.1, 0 μg/ml). Each slide was printed with an array of 24 spots with each concentration duplicated as shown in **Appendix A-4**. Slides were allowed to dry overnight before experimentation. Each array slide was loaded into a Whatman Chip Clip slide incubation apparatus, and blocked for 1 hour with 1 mg/ml BSA in PBS. Slides were then incubated for 30 minutes in 25 μg/ml SA-EITC in 1 mg/ml BSA in PBS. During incubation, the slides were protected from light to prevent photobleaching during photoinitiator loading at biotinylated sites. Slides were then rinsed 3 times with PBS, and photopolymerized with either PEGDA-575 or PEGDA-3500 monomer formulations at identical conditions as detailed above for live cell coatings. Slides were then washed once with PBS, 3 times with deionized water, and allowed to dry for 1 hour. To measure thickness response, a Dektak 6M stylus profilometer was used with a 1 mg stylus force

and a scan rate of 120 μm/s. Average height of each spot was measured, with n=6 spots for each measurement.

7.2.9 Cy3 Calibration of Slide Fluorescent Labeling

Array fluorescence was measured using an Affymetrix 428 Array Scanner. Streptavidin-Cy3 conjugates were contacted with array slides at identical conditions as for SA-EITC conjugates detailed above (n=6 spots at each concentration analyzed for Cy3 binding). Both SA-Cy3 and SA-EITC fluorescence was then measured with 532 nm laser excitation, detection with a PMT with a bandpass filter centered at 570 nm, and the gain set at 30 db. Array spot binding density was then calculated by calibrating at 30 db gain with a Cy3 scanner calibration slide from Full Moon Biosystems. Calibration slides contain 12 replicate spots of 28 different concentrations arranged at a 2-fold dilution. By UV-Vis spectroscopy analysis of SA-Cy3 and SA-EITC conjugates (**Figure A-2.4, Equation A-2.1, Figure 7.4, Equation 7.2**), the ratio of EITC to Cy3 functionalization was calculated to be ~2.1, which allowed for photoinitiator surface density to be calculated for each printed array spot.

7.3 Results and Discussion

The overall goal of this work was to determine to effect of photoinitiator labeling density on the gelation response and cell protection efficiency (i.e. yield) in lysing conditions. A549 lung cancer cells are biotinylated either covalently or with antibody targeting, then coated by visible light photopolymerization. The protection afforded by the coating was determined by exposing the coated cells to lysing conditions and interrogating the remaining cells by both fluorescent microscopy and flow cytometry. In parallel, an analogous planar microarray system is biotinylated and exposed to identical

photopolymerization conditions to provide hydrogel film thickness information about our system by profilometry analysis. Photoinitiator binding density is quantified fluorometrically in both experimental scenarios for comparison.

We first confirm the structural integrity of polymer coated cells in a 5% SDS lysis solution. **Figure 7.5** shows an overlay of fluorescent micrograph images of A549 cells encapsulated with crosslinked PEGDA-3500 just after exposure to 5% SDS lysis solution. Here, cells were biotinylated with the "metastatic" antibody cocktail (anti-CD44, Ant-ICAM-1, anti-EGFR). Panel (a) shows a fluorescent image of yellow-green fluorescent imaging nanoparticles previously shown to be physically entangled in the crosslinked film mesh in similar systems [97], showing visible fluorescent signal completely surrounding the cell perimeter. Panel (b), taken at the same stage position, is Hoechst 33342 DNA staining, which exhibits fluorescence confined to a smaller region than the polymer coating. The smaller localization of the DNA is consistent with a structurally-intact nuclear envelope. Frame (c) shows the blue and green channel overlaid, suggesting the cells have remained protected and intact and nuclear DNA localization has remained largely unaltered. We were unable to image any distinct structures in the cellular lysate of unprotected cells. Further, we have previously shown polymer coated cells are viable and proliferate after removal of the coating. In all, fluorescent imaging of the polymer supports the formation of a conformal coating, while nuclear staining supports the integrity of polymer coated cells in lysis conditions.

7.3.1 Relationship Between Initiator Density and Cellular Protection

Our seminal work in ASL work describes a binary relationship between specific photoinitiator labeling with antibodies and protection from surfactant lysis. On a

fundamental level, any antibody-based labeling is a contrast between specific and nonspecific labeling. As a result, our prior work implies that the specific labeling is sufficient to form a protective coating and nonspecific labeling is insufficient. In reality, the marker density of different surface receptors varies by several orders of magnitude within a single cell type. As such, even for a single cell type and a single marker, one would expect some cells to have high marker density and some to have low marker density. We hypothesize that this heterogeneity in marker density will translate to a comparable heterogeneity in photoinitiator density on the surface. In this same population, only a given fraction of cells will have sufficient photoinitiator density to completely form a protective coating on the given cell. Thus, only a fraction of the cells are expected to remain intact after surfactant exposure. The fraction of intact cells following surfactant exposure is expected to increase with an increase in the mean photoinitiator density for the population. In antigen labeling experiments, this equates to higher yields for higher surface densities of the targeted marker.

Figure 7.6 shows the results of the flow cytometry analysis of process yield dependence on mean photoinitiator labeling density of each sample. The presence of an intact cell was defined by both size and fluorescent intensity. A549 cells were labeled intracellularly with CellTracker Deep Red at the outset of each experiment to enable flow detection with the 630 nm laser and 675/25 nm filter combination in the FL4 channel. The excitation-emission spectra for this dye was specifically chosen because of the spectral separation at higher wavelengths from the photoinitiator, imaging nanoparticles, and irradiation lamp used in this study to provide a distinct and reliable fluorescent indicator of an intact cell event. Additionally, intact A549 populations consistently show

forward scatter above ~2,000,000 for our instrument. Thus, a "positive" intact cell event was defined based on live stained A549 controls by quadrant gating FSC vs FL4 as FSC > 2,000,000 a.u. and FL4 > 30,000 a.u. (**Figure 7.2**). The yield of intact cells was calculated as the cell count per 1 mL after lysis divided by the cell count per 1 mL just before polymerization. The mean photoinitiator density (fluorophores/μm^2) for each data point was determined by calibrating overall streptavidin-photoinitiator binding to A549 with a QuantiBRITE fluorescence quantitation assay, and then normalizing with the calculated spherical model surface area.

Figure 7.6.a shows a summary plot of A549 yield versus photoinitiator density for polymer coating with 25 wt% PEGDA-575. Each data point represents an independent isolation experiment. Covalently biotinylated samples were incrementally loaded by competitive binding of varied ratios of streptavidin-photoinitiator and unconjugated streptavidin. As expected, the yield of intact cells after lysis depletion was strongly and directly dependent on photoinitiator surface density. At the lowest loading density investigated (~1,600 eosin molecules per μm^2), the yield was <1%, while at the highest bound of our PEGDA-575 study of above 54,000 eosin molecules per μm^2 showed nearly 50% yield of intact cells. **Figure 7.6.b** shows a similar summary plot of isolation yield dependence on photoinitiator loading for PEGDA-3500 photopolymerization. As before, A549 cell samples were biotinylated covalently by succinimide-amine chemistry indiscriminately on surface proteins, then loaded with streptavidin eosin at incrementally varied levels by competitive binding with unconjugated streptavidin. At the lowest level of eosin loading of ~1,300 molecules per μm^2, yield was again below 1%, while for the highest bound of eosin functionalization at

~43,000 molecules per μm^2, the yield here for PEGDA-3500 coated samples was as high as 68%. For both monomer formulations, there is a distinct trend for a larger fraction of cells remaining intact when protected by a coating formed with a higher mean surface density of the eosin photoinitiator. This qualitatively agrees with our hypothesis that more cells in the population are above a threshold photoinitiator density required for protection.

With a protection trend established with nonspecific biotin functionalization of cell surfaces, we sought to verify this trend in an antibody labeling system. In separate experiments, cancer cell targeting scenarios were also investigated using antibodies. We have previously shown that A549 exhibit significantly lower surface density of epithelial markers (EpCAM and E-cadherin) than stem-like markers such as CD44 and metastasis markers like EGFR and ICAM-1 [172]. **Figure 7.6.a** shows that EpCAM targeting resulted in low photoinitiator loading density in agreement with our previous findings of below 1,200 eosin molecules per μm^2. The low eosin surface concentration using EpCAM resulted in low isolation yield near 1% for a PEGDA-575 monomer solution. For PEGDA-3500 in **Figure 7.6.b**, eosin loading was also below 1,200 molecules per μm^2 and delivered correspondingly yield of intact cells at around 1%. The yield of intact cells for both monomers are in close agreement with predictions based on the covalent labeling studies.

In separate experiments, A549 cell samples were also biotinylated by targeting a panel of markers implicated in metastasis, which included CD44, ICAM-1, and EGFR. In **Figure 7.6.a**, this antibody targeting strategy allowed for much higher surface densities of between 10,000 and 20,000 eosins per μm^2, and resulted in higher yield of intact cells

of approximately 20% for the PEGDA-575. Similarly, the metastatic marker targeting resulted in ~10% yield of intact cells for the PEGDA-3500. The qualitative trend of higher yields was in fairly good agreement with the percent yield of corresponding covalent biotinylated samples of similar photoinitiator loading. Further, **Figure 7.7** shows a negative control representing nonspecific labeling of streptavidin-photoinitiator without biotinylation by antibodies or covalent grafting. For both monomer formulations, photoinitiator loading densities were in the range of 100-200 eosin molecules per μm^2 and yielded <0.1% intact events, indicating that protection during lysis is predominantly due to the specific labeling of streptavidin-photoinitiator at biotinylated sites.

7.3.2 Analysis of Photopolymerization Gelation Response

Quantitative comparison of the lysis protection by PEGDA-575 and PEGDA-3500 indicates a higher yield of intact cells for the PEGDA-3500. Specifically, a PEGDA 575 coating from a photoinitiator density of 35,000 molecules per μm^2 results in ~35% yield, while the same photoinitiator density provides ~60% yield using the PEGDA-3500 monomer. To determine if this discrepancy originates in the sensitivity of polymer formation, we studied the polymerization of each monomer system on protein microarrays. Because of the inherent variability in cell geometry and morphology, direct measurement of nanothin film coating thickness on suspended cell substrates is prohibitively challenging. Protein microarrays on glass offer a reproducible platform to analyze these thicknesses (**Figure 7.8.a-c**). Photoinitiator surface densities can be tuned to recapitulate the range seen on cancer cell surfaces during ASL (0 to 20,000 eosin molecules per μm^2). **Figures 7.8.d** and **Figure 7.8.e** show plots of measured profilometry thickness of polymerized microarrays at varied photoinitiator densities.

Photopolymerization conditions were identical to those used for cell suspensions for both PEGDA-575 and PEGDA-3500 formulations. **Plot 7.8.d** shows the gelation response for PEGDA-575 reaches average thickness of 85 nm at the high bound of the array experiment at approximately 17,000 eosin molecules per μm^2. **Plot 7.8.e** shows the gelation response for PEGDA-3500 which exhibits a lower gel thickness response, reaching approximately 40 nm at the highest eosin density investigated.

Figure 7.8 also indicates that polymer forms at photoinitiator densities of ~100 and ~1,000 for PEGDA 575 and 3500, respectively. This observation is contrasted with the cell yield data, where comparable densities offers negligible protection (~1% yield, **Figure 7.6**). This underscores the requirement of a *complete* coating for protection against lysis. This has dramatic implications for the purity of ASL isolation, where cell with low levels of nonspecific adsorption is unlikely to protect a cell against lysis. Similarly, if large antibody aggregates adhere to a cell surface, it is unlikely to form a complete protective coating around the cell. The higher threshold of the PEGDA-3500 over PEGDA-575 suggests the 3500 system requires a higher antigen density for protection over the PEGDA-575 system. The distinction between the 575 and 3500 systems is not definitively observed in the yield data in **Figure 7.6**. Critically, the data in **Figure 7.6** is an analysis based on population means, where cell-level data is obscured.

7.3.3 Determining Photoinitiator Loading Threshold Required for Isolation

The calculated mean photoinitiator density is not a sufficient parameter to determine a required photoinitiator density for the protection of a given cell. To determine a minimum threshold density for protection, we must further examine the distribution of eosin-label density for each population. If an exact threshold exists, we

would expect every cell of higher eosin density than the threshold to remain intact through the lysis. As such, we expect a population with X % of events having greater eosin density than the threshold to have a yield of X %. To evaluate this we calculated the yield of each population and drew a line on the surface density histogram where the fraction of events with higher eosin density than the line is equal to that sample's yield. Further, we would expect this threshold to be the same for every trial. For example, if a hypothetical isolation run resulted in 60% yield intact cells, the histogram of eosin labeling for that experiment would be labeled at a density corresponding to 60% of events above the threshold. We then analyzed the surface density corresponding to that line for each population.

Figure 7.9 shows representative "low", "mid", and "high" photoinitiator labeling examples from our study for both PEGDA-575 and PEGDA-3500 polymer formulations. In **Figure 7.10**, we plot this threshold gate for all data trials for both PEGDA-575 and PEGDA-3500. There is a general upward trend in threshold photoinitiator density for the PEGDA-575. In the PEGDA-3500 system, the calculated threshold density value is independent of process yield. While the mean photoinitiator density shifts drastically in these systems (~50 fold change), the hypothetical density threshold corresponding to the yield only varies by 4 fold. This suggests that the eventual yield delivered is a strong function of the population distribution of initiator labeling in relation to this threshold. Based on our cytometry labeling calibration analysis described above, these threshold photoinitiator densities are roughly 27,000 eosin molecules per μm^2 and 21,000 eosin molecules per μm^2 for PEGDA-575 and PEGDA-3500 formulations, respectively.

7.4 Conclusions

In this work we have investigated the relationship between marker expression density on cancer cells and the yield of intact cells during ASL. A lung cancer cell line (A549) was used as a model CTC and cells were incrementally biotinylated via covalently functionalization and subsequent competitive binding with PI-conjugated and unconjugated streptavidin, which provided a predictable prototypic system to methodically study labeling density effects on yield. We have shown a strong, direct correlation between photoinitiator surface density and yield of protected, intact cells. Based on previous work [171], we expect these results to translate to heterogeneous cell suspensions and represents a critical first step in validating ASL as versatile platform for CTC isolation.

Further, there was no appreciable difference between covalent eosin functionalization and the antibody targeting strategies examined here. Mammalian cell membranes are a complex, dynamic composition of cell proteins and other biomolecules that are distributed over the cell surface into discrete locations, often non-randomly. We realized caution should be taken when selecting biomarkers for photoinitiator targeting because some have been shown to cluster into “islands” [173], which could exaggerate non-uniformity in expression and lead to incomplete coating formation. Because little difference was seen between covalent biotinylation and the markers selected here, we conclude that any surface protein clustering phenomena were not significant enough to preclude successful isolation of the cell/antigen systems studied.

Finally, we purposely chose to investigate an expanded photoinitiator loading range through covalent targeting that far exceeded conventional antibody targeting, and

showed elevated yield response at higher photoinitiator loading levels. These results suggest ASL would potentially benefit from the design and implementation of streptavidin-macrophotoinitiators that have been shown to direct several fold greater quantities of photoinitiator molecules to each site of biotin recognition and increase polymer amplification response [141]. Moving forward, development of such routes to increased gelation response to biorecognition could conceivably enable robust positive isolation based on targeting poorly expressed proteins that may be of high clinical relevance.

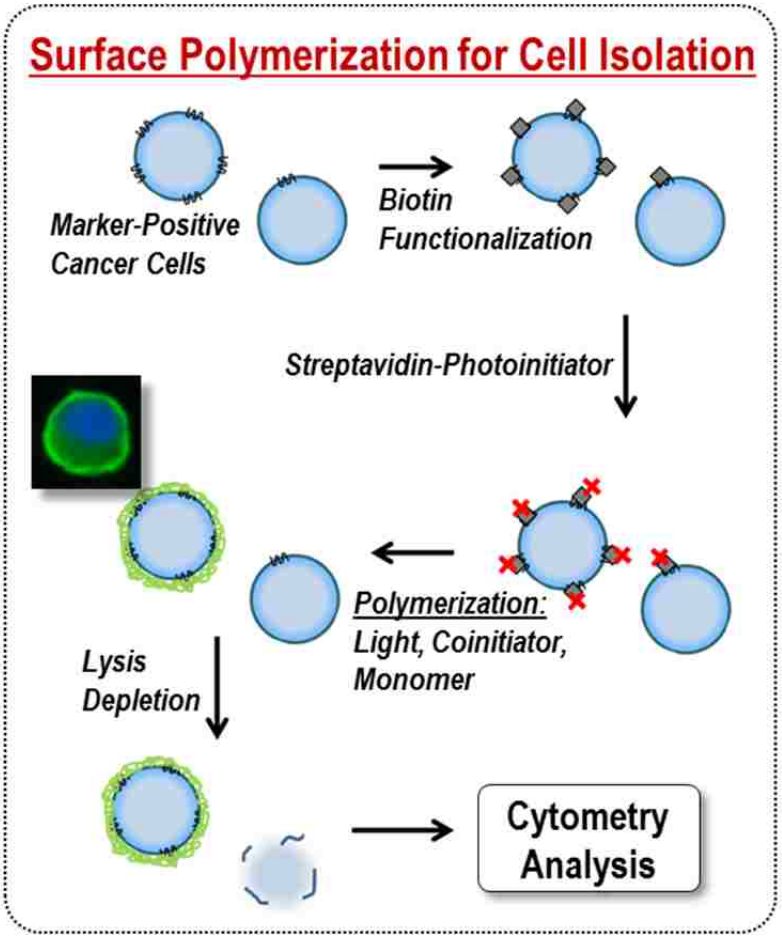

Figure 7.1: Schematic of surface polymerization approach for cancer cell isolation. Photoinitiator loading dictates yield of polymerized cells in surfactant lysis conditions.

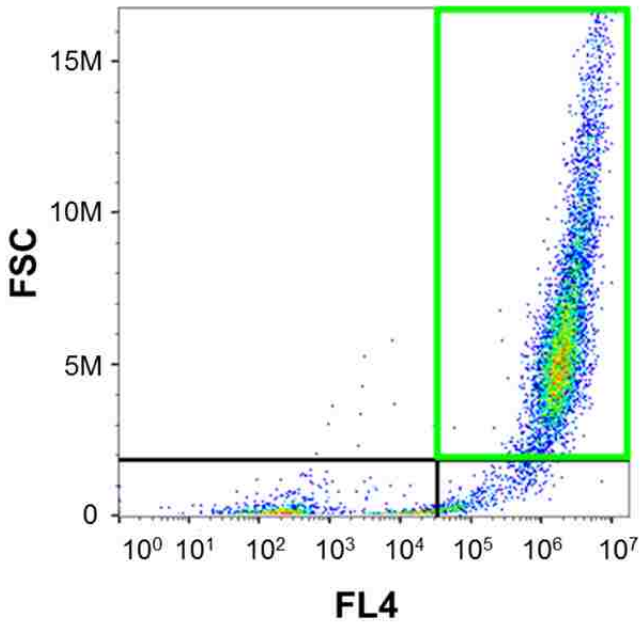

Figure 7.2: Flow cytometry control plot of forward scatter vs. FL4 showing gating definition of an intact cell in upper right quadrant.

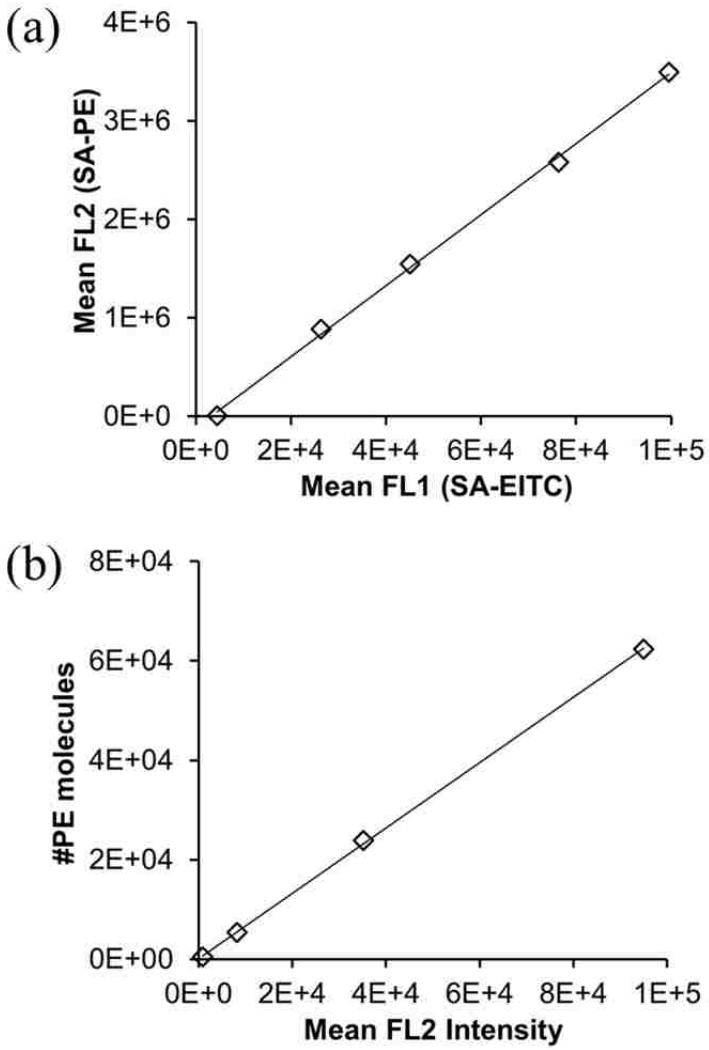

Figure 7.3: (a) Linear regression of FL2 vs. FL1 for calibration of SA-PE and SA-EITC labeling at varied biotinylation. (b) Cytometry standard curve of FL2 for R-phycoerythrin functionalized beads.

$$\frac{\#\mathbf{EITC\ molecules}}{\boldsymbol{\mu m^2}} = \frac{\mathbf{3.78[36.1(FL1) - 114929] + 111}}{\mathbf{908 \mu m^2}}$$

Equation 7.1: Calibration equation to relate photoinitiator cell surface density to mean FL1 of individual cell samples.

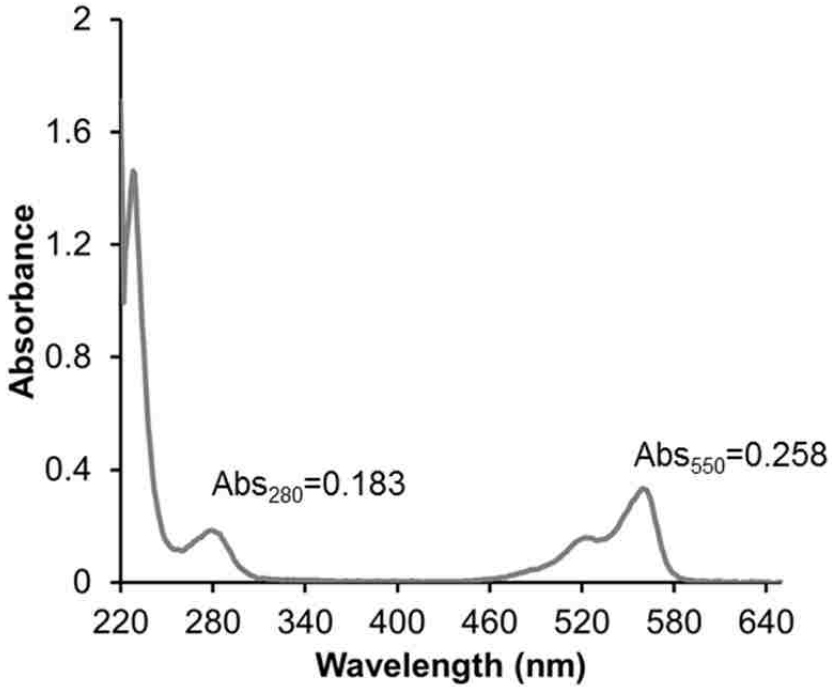

Figure 7.4: UV-vis absorbance spectra of streptavidin-Cy3 conjugate.

$$\textbf{molar ratio}\left(\frac{\textbf{Cy3}}{\textbf{SA}}\right)=\frac{\mathbf{MW_{SA}}}{\mathbf{MW_{Cy3}}}\frac{\mathbf{0.0757Abs_{Cy3,550}-0.0008}}{\mathbf{2.81\left(Abs_{SA,280}-Abs_{Cy3,280}\right)+0.0011}}$$

Equation 7.2: Equation to calculate the DOS of Cy3:SA by regression analysis of UV-vis analysis of absorbance values at 280 nm and 550 nm.

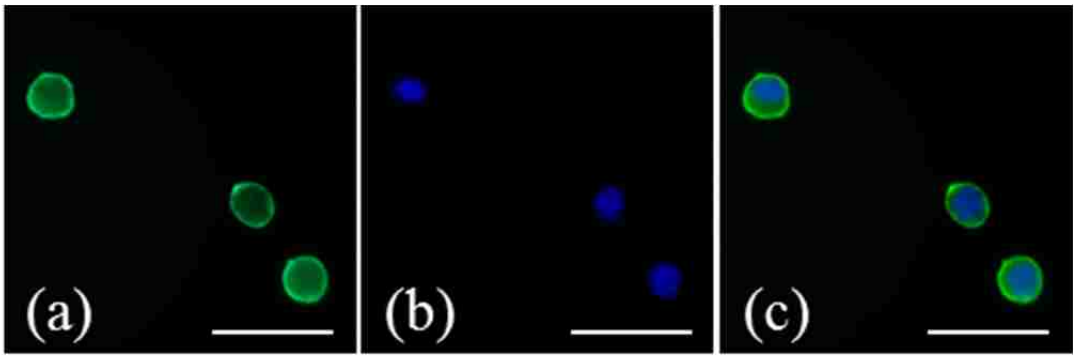

Figure 7.5: Fluorescent micrograph overlays of PEGDA coated A549 cells after exposure to 5% SDS lysing conditions. (a) Fluorescent signal from 20 nm yellow-green imaging nanoparticles physically entangled in polymer mesh. (b) Hoechst 33342 blue DNA staining. (c) Overlay of yellow-green nanoparticle and Hoechst 33342 images. Scale bars represent 50μm.

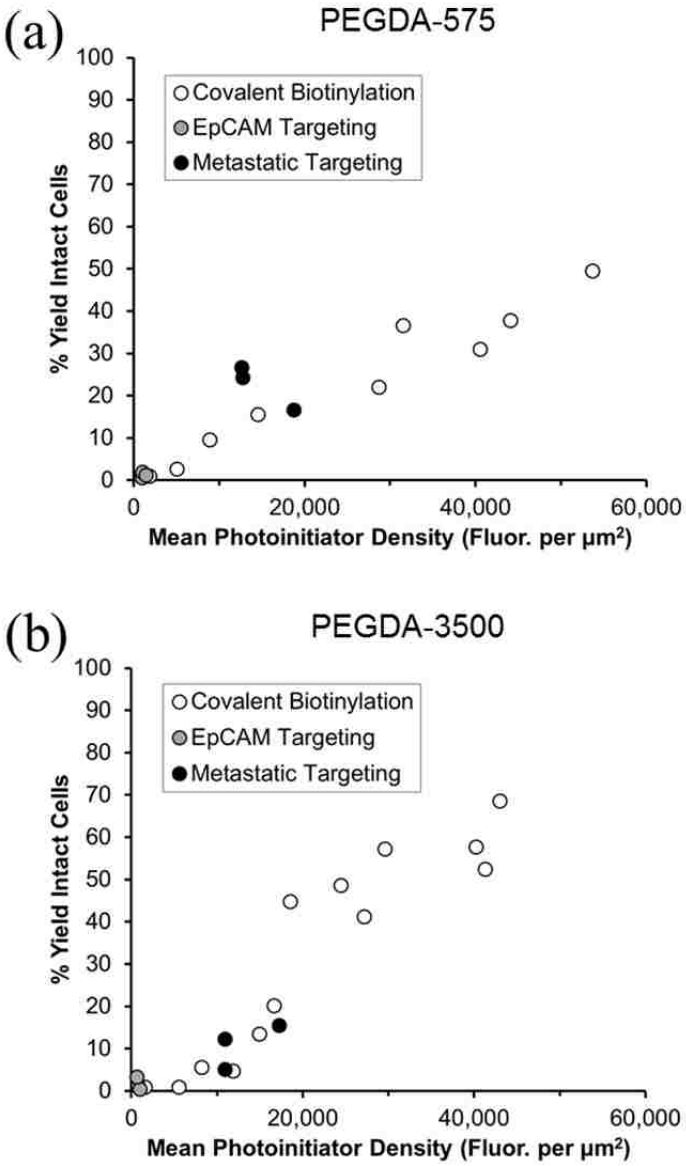

Figure 7.6: Plots of ASL isolation experiments showing yield intact yells attained after lysis vs. corresponding mean photoinitiator density via either covalent or antibody biotinylation for (a) PEGDA-575 and (b) PEGDA-3500 monomers during photopolymerization.

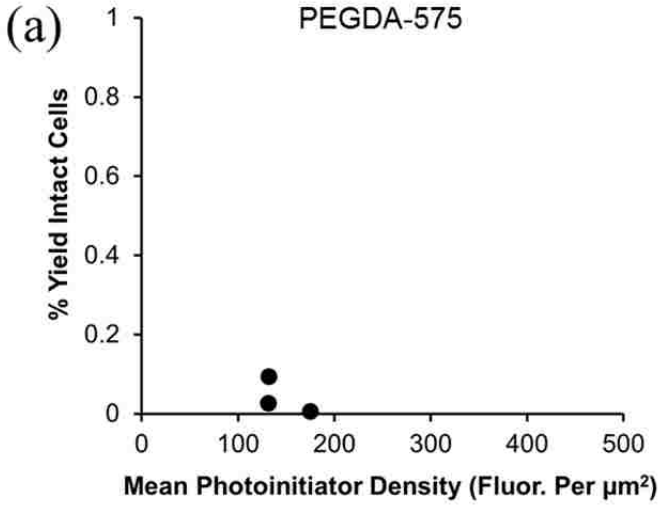

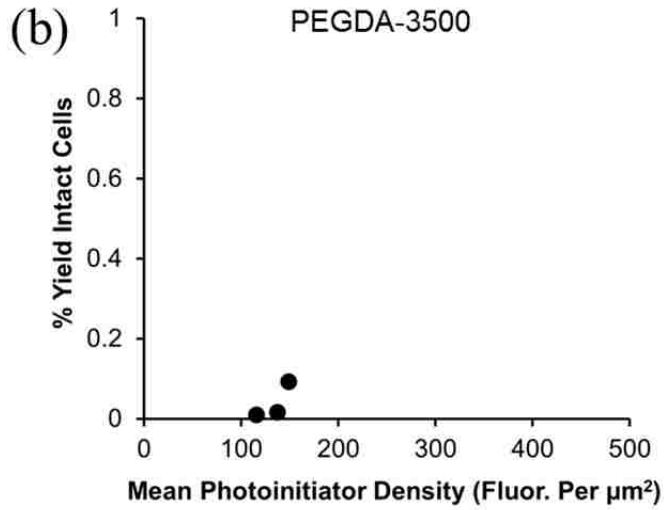

Figure 7.7: ASL negative control of A549 targeting. % Yield of intact cells for non-specific SA-EITC labeling for (a) PEGDA-575 and (b) PEGDA-3500 monomer formulations.

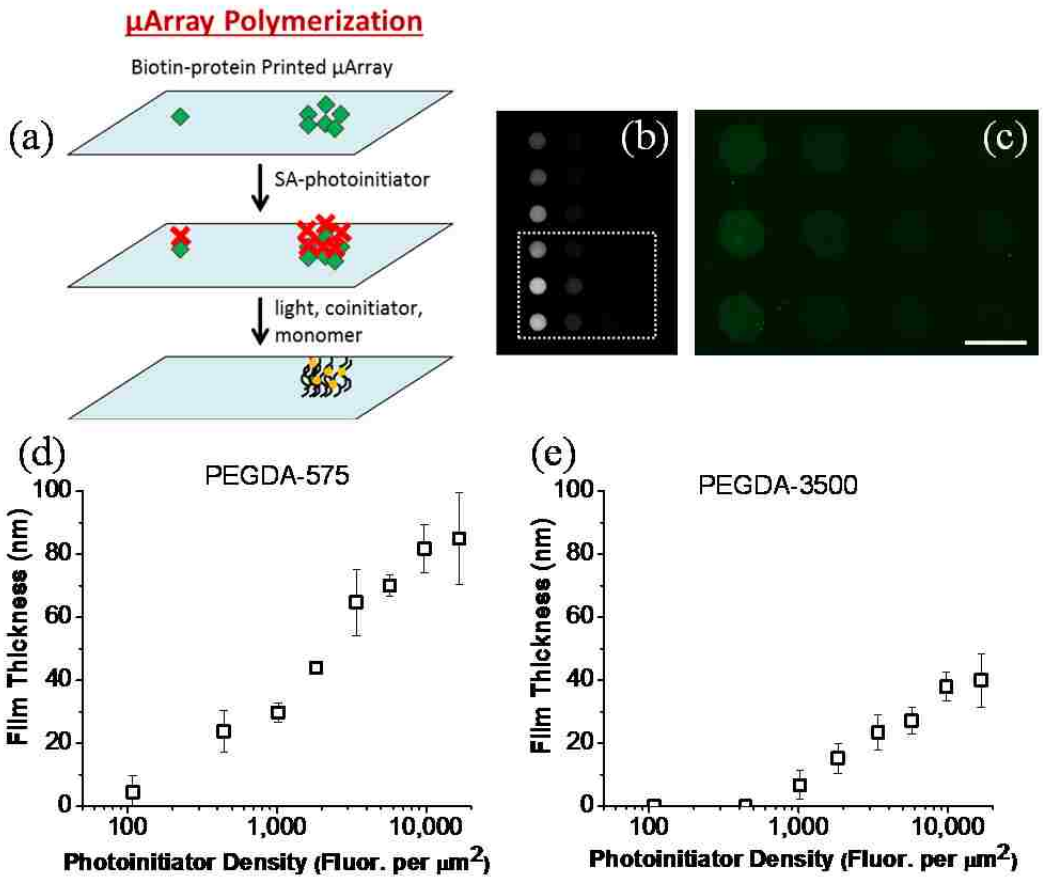

Figure 7.8: (a) Schematic of polymer microarrays to analyze gelation response vs. photoinitiator density. Biotin-BSA protein arrays are printed at serial dilution, contacted with SA-EITC and photopolymerized with cell encapsulation conditions. Panel (b) shows fluorescent array scanner image showing specific SA-EITC binding and fluorescence. (c) Fluorescent microscopy image after photopolymerization showing fluorescent nanoparticle loaded polymer film formation. Scale bar represents 500 µm. Contact profilometry thickness analysis vs. photoinitiator surface density of (d) PEGDA-575 and (e) PEGDA-3500 monomer formulations. Errors bars represent standard error for n=6 spot concentrations.

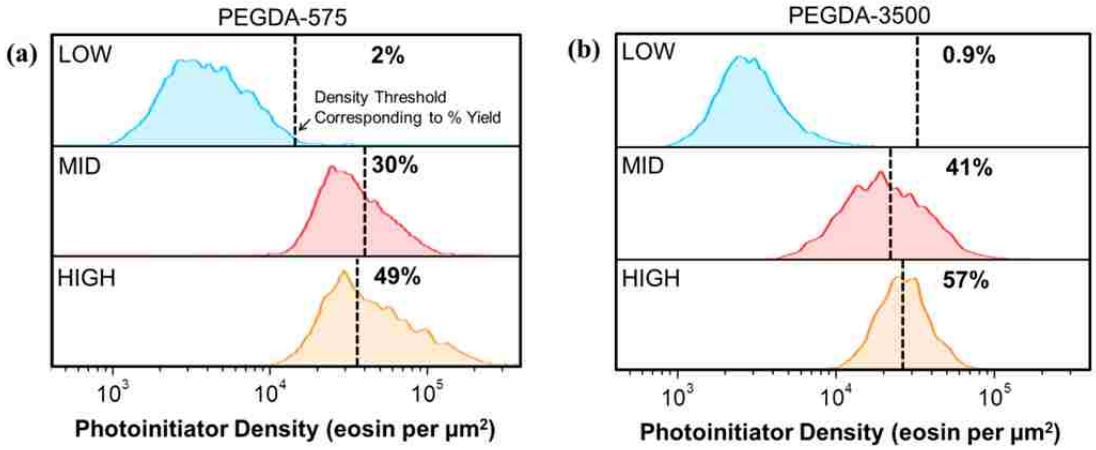

Figure 7.9: Photoinitiator density threshold analysis. Representative histograms for "low", "mid", and "high" photoinitiator loading trials and the FL1 intensity of the gating corresponding to the % yield of each individual experiment for both (a) PEGDA-575 (b) PEGDA-3500.

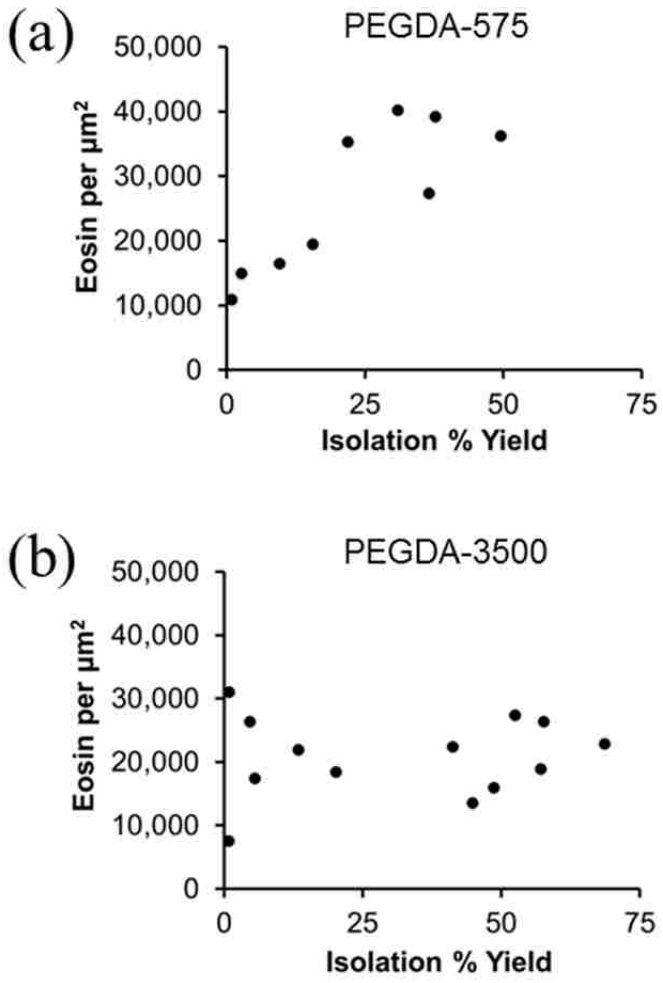

Figure 7.10: The threshold photoinitiator density corresponding to each individual isolation % yield shown for (a) PEGDA-575 and (b) PEGDA-3500 formulations.

Chapter 8: Conclusions and Future Perspectives

In this work, we explored the development of cell surface coatings formed by interfacial polymerization for protection during a lysis-based isolation method. This dissertation demonstrated several key findings for this novel technique. First in Chapter 4, individual cells were encapsulated with complete and conformal PEG crosslinked coatings, and are shown to remain highly viable through this biocompatible process. Polymer coatings are specifically formed from photoinitiator-tagged cell surface receptors through polymer-based amplification. Further, these film coatings exhibit size selective permeability, completely excluding fluorescent dextran molecules above a molecular weight of approximately 10 kDa. We then further explored this coating technique to specifically target and sort marker-presenting cells in heterogeneous mixtures in Chapter 5. Notably, model CTCs were sorted with exceptional purity (~99%) from spiked human buffy coat by targeting the EpCAM surface marker. Designed *ortho*-nitrobenzyl groups between crosslinks allows for photodegradation of positively-sorted cell to release pure populations for further analysis. Viability and proliferation assays showed these sorted and released cells are highly viable and proliferative compared to controls of cultured cells. While this study demonstrated ASL has great promise for high performance cell sorting of viable cells, we then focused on further examining marker availability and the feasibility of potential targeting scenarios. Chapter 6 examined the available densities of a panel of metastatic markers on commonly studied breast and lung cancer lines, revealing extreme variability between markers and cell lines. This showed that greater appreciation for biological heterogeneity is warranted when designing isolation targeting strategies, particularly for CTCs which have been shown to

downregulate epithelial markers. Finally in Chapter 7, our last study related the marker density for targeting to the eventual ASL process yield, and showed that targeting metastatic markers on A549 cells resulted in significantly higher process yield, as expected from the prior marker density analysis. In this work, we also determined a density threshold of photoinitiator functionalization on A549 for complete gelation and successful positive isolation that we expect to be generally applicable to other cell targeting scenarios.

Uniquely, we have demonstrated high performance for this sorting technique with components that are inexpensive and generally commercially available. The LED lamps to initiate polymerization are approximately $1000 each, and the costs for antibodies used in photoinitiator tagging are continuing to decrease as immunolabeling becomes more commonplace for virtually all biological research fields. The processing containers are pre-sterilized polystyrene or polypropylene cell culture products that are disposable, eliminating the need for lengthy and costly cleaning as required for fluorescent sorting. These low costs of processing could conceivably make ASL more accessible to a broader range of researchers that are generally not able to use other high cost competing technologies.

8.1 Future Perspectives

The results presented in this dissertation suggest ASL is a promising technology for the rapid sorting of tumor cells. However, there are several barriers to development and clinical implementation. The following sections detail these challenges and the future goals of this research direction.

8.1.1 Correlating Marker Targeting Scenarios with Invasive Functionality of CTCs

This work previously demonstrated the proliferative capacity and viability of cells after sorting. However, in the context of CTCs the most definitive assessment of functionality is direct measurement of invasiveness and motility. Therefore, we will evaluate the functionality of CTCs toward metastatic potential using a Matrigel basement membrane invasion assay. We expect that cells possessing the appropriate repertoire of migratory proteins and signaling will be able to dissolve the basement membrane mimicking 3D culture and will invade the farthest into the gel. The model CTCs with the high metastatic relevance will be generated by TGF-β stimulation, whereas tumor lines directly from normal epithelial culture will display lower metastatic potential. We hypothesize that sorting EMT stimulated model CTCs with stem cell markers will yield cells with the highest invasive potential in the Matrigel assay, given that the markers targeting allow sufficient eosin priming above the coating isolation threshold. Conversely, sorting tumor cells with epithelial markers that have not been stimulated toward a mesenchymal phenotype will yield cells with a lower invasive phenotype. All sorted scenarios will be compared to the parallel controls of cultured tumor lines seeded at matching cell densities into the Matrigel invasion wells. We expect that sorted cells to behave similarly to unsorted controls, in that they will proliferate and invade similarly. Additionally, migratory potential will also be confirmed with a wound healing scratch assay. As in the Matrigel assay, we expect that EMT stimulated model CTCs to migrate at a faster rate than non-stimulated counterparts. We again hypothesize that sorting by stem markers will yield populations with higher migratory potential than sorting by epithelial markers, and that sorted cells will migrate comparably to pre-sorted controls.

These assays will serve to both validate the metastatic functionality of CTCs sorted by ASL as well as further link a stem-like phenotype to higher invasive potential. We expect that these validations will inform the development of ASL as a more clinically relevant CTC isolation technology capable of delivering pure populations of biologically functional metastatic cells for analysis.

8.1.2 Developing ASL for Clinical Translation

Several challenges must be overcome to enable the translation of ASL as a clinically useful fluid biopsy technology. First, because these tumor cells circulate in metastatic patients at extreme rarity, the process yield for antibody targeting scenarios must be improved. In Chapter 7, we have shown that even with targeting several markers that are shown to be overexpressed in the model cell line used in the study, we were only able to achieve approximately 25% cell yield. However, the study also showed that by greatly increasing the photoinitiator labeling density with covalent tagging over what is capable with traditional immunolabeling, process yield was improved to approximately 50-60%. In these studies, we functionalized 4-5 eosin molecules per streptavidin; however, to achieve significantly higher levels of photoinitiator labeling we aim to design streptavidin-macrophotoinitiator conjugates that are capable of directing tens to hundreds of photoinitiator molecules per biotin binding event [141]. Macrophotoinitiators will be synthesized by coupling an excess of eosin isothiocyanate to primary amines of poly(acrylamide-co-acrylic acid) macromers of varying lengths. To conjugate photoinitiator macromers to avidin groups, carboxyl moeities contributed by acrylic acid monomer units will be activated by EDC/sulfo-NHS, quenched with 2-mercaptoethanol, and then reacted with streptavidin. Similarly, fluorescein macrophotoinitiators will be

investigated for feasibility with ASL. In preliminary studies, our group has shown the polymerized gel thickness of fluorescein surface initiation systems can rival eosin systems, but the fluorescein fluorophore is more widely assimilated in the scientific community and is approximately 20 times cheaper per milligram. Using these types of macrophotoinitiators systems, we expect significantly higher levels of photoinitiator surface densities can be achieved that will improve process yield.

After process yield is improved and carefully validated with model systems developed *in vitro*, the feasibility of ASL sorting patient-derived samples can be examined. The key advantage of ASL over other CTC isolation methodologies is the potential to rapidly collect *functional* cells. Conceivably, this technology is uniquely positioned to enable the researcher to correlate cancer cell phenotype and functional characteristics at both the tumor primary, at metastatic lesions, as well as in circulation from a single patient. While this correlative study is an exciting future possibility, there are challenges to achieving that goal particularly due to the rarity and uncertainty of cell occurrences in circulation. A practical starting point is at the primary, where there are simply more cells for experimentation. Fresh primary tissue punch biopsies can be collected, then enzymatically and mechanically dispersed into a cell suspension for ASL processing. A preliminary study of interest at the primary would be to first separate different regions associated with the primary (i.e. necrotic core, invasive front, stromal tissue) and sort in parallel. Here, one could examine the frequency of cells that are obtained at each region by positively sorting with a panel of markers, but also compare the functional characteristics of those populations post-sorting. After the ASL system is

well established with primary tissue, matched primary, secondary, and peripheral blood samples can be examined for similarities in cell phenotype and behavior.

Other challenges for clinical translation center around the logistics of processing the sheer magnitude of cells one would see in a fluid biopsy setting. A red blood cell depletion step with ammonium chloride is widely used for an initial debulking step; however, removing that large quantity of material from the system while preserving and separating all nucleated cells becomes a challenge. The incorporation of EDTA and DNase I is expected to be beneficial in preventing large cell clumping of nucleated cells. Practical adaptations must also be made for material handling, as density based centrifugation in culture tubes may cause the unintentional removal of large proportions of CTCs from the sample. Further, to photopolymerize these large cell samples, larger collimated LED lamps must be designed that can accommodate the large irradiation areas needed for adequate photoinitiation.

Appendix

A-1 Cell Photopolymerization and Degradation Experimental Set-Up

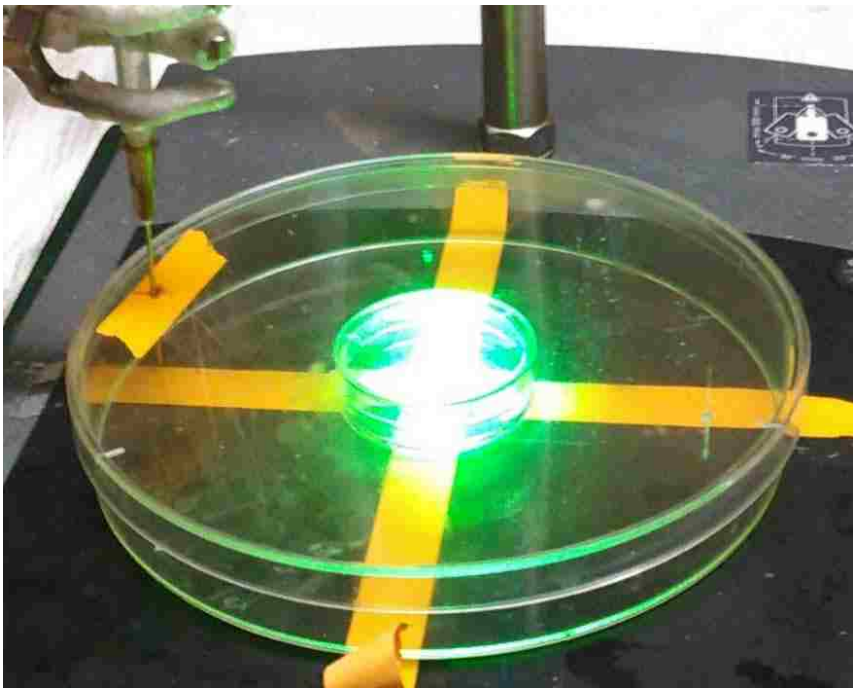

Figure A-1.1: Photograph of purging and photopolymerization set up. Cells are suspended in monomer solution in recessed well of cover glass bottom 35mm dish, and purged with ultra-pure N_2 in a 150mm clear culture dish outfitted with inlet and outlet ports. Irradiation light is supplied by collimated LED lamp (ThorLabs) outputting 530nm light.

Figure A-1.2: Photograph of the UV photodegradation apparatus. Collimated LED outputting 365 nm light with a ChipClip / FAST-slide assembly.

A-2 UV-Vis Analysis and Calculation of Degree of Substitution (DOS) for Streptavidin-eosin-isothiocyanate Conjugation

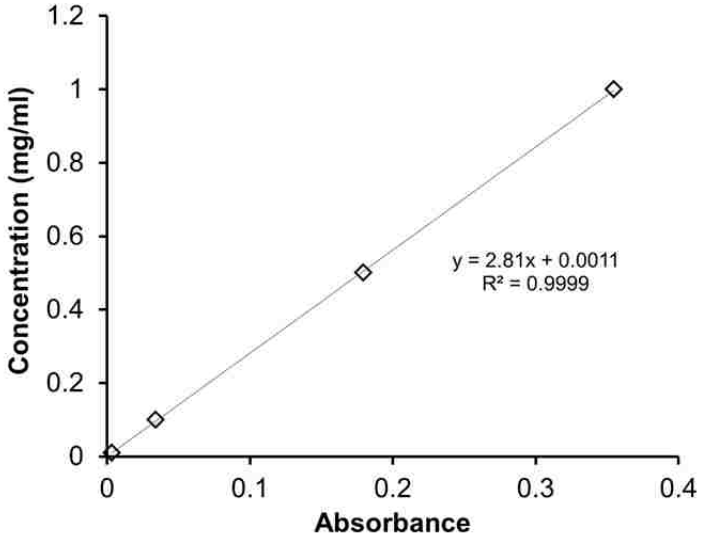

Figure A-2.1: UV-Vis standard curve of streptavidin prepared in PBS. Absorbances are at 280 nm.

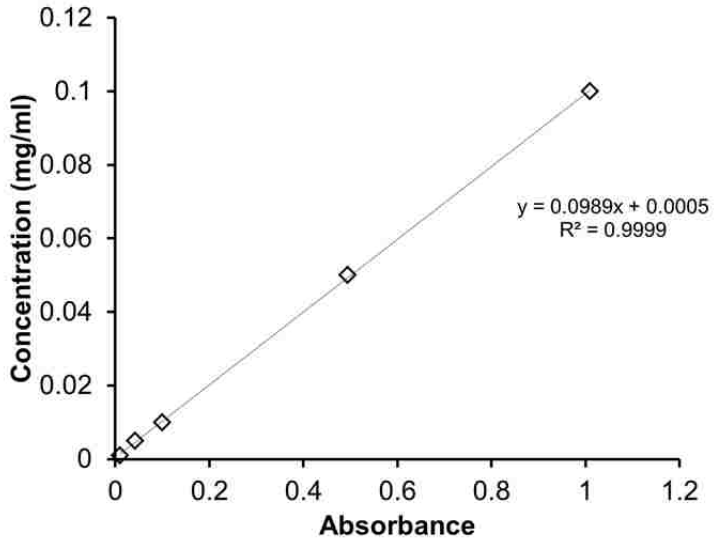

Figure A-2.2: UV-Vis standard curve of eosin-isothiocyanate prepared in PBS. Absorbances are at 530 nm.

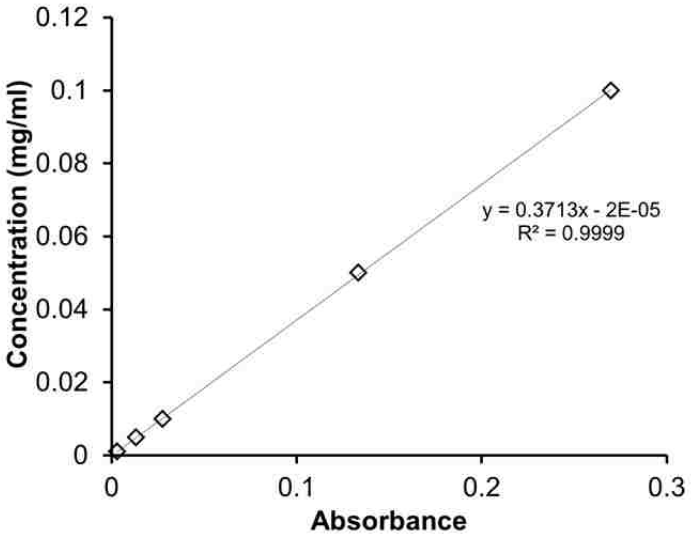

Figure A-2.3: Standard curve relating concentration and UV-Vis absorbance at 280 nm of eosin isothiocyanate prepared in PBS.

$$\textbf{molar ratio}\left(\frac{\textbf{EITC}}{\textbf{SA}}\right)=\frac{\mathbf{MW_{SA}}}{\mathbf{MW_{EITC}}}\frac{\mathbf{0.0989Abs_{EITC,530}+0.0005}}{\mathbf{2.81\left(Abs_{SA,280}-Abs_{EITC,280}\right)+0.0011}}$$

Equation A-2.1: Calculation of degree of substitution (DOS) of conjugation of eosin isothiocyanate (EITC) to streptavidin from UV-vis standard curve regression analysis.

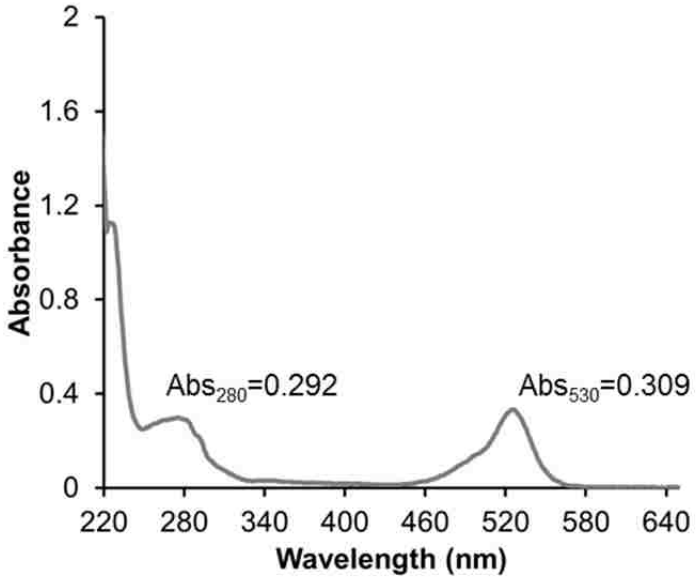

Figure A-2.4: Example of UV-Vis spectra of SA-EITC conjugate showing absorbance peaks at 280 nm and 530 nm.

A-3 Study of Significant Reaction Parameters Affecting Degree of Substitution of Streptavidin-eosin-isothiocyanate Conjugation

Polymerization experiments in this dissertation involve the specific labeling of biotinylated sites with streptavidin (SA) which is covalently conjugated with eosin istothiocyanate (EITC). The isothiocyanate group reacts with the primary amine of lysine residues at pH ~ 8 to 10. Previous studies report the use of general reaction protocol which involves dissolving lyophilized streptavidin at 10 mg/ml in 0.1 M carbonate buffer at pH 9, and reacting with EITC at a 140:1 molar ratio (EITC:SA) for 8 to 9 hours at 4 ˚C in the dark [98]. This protocol yields conjugates with a calculated DOS of approximately 2-3. We hypothesized that higher photoinitiator loading for cell labeling could be obtained by increasing the DOS of the EITC to SA reaction. Therefore, and investigation of the significant reaction parameters dictating the extent of labeling was warranted. We examined pH, reaction time, and the reactant molar ratio in the study, while the total buffer salt concentration and reaction temperature were kept constant. First, the molar ratio was kept constant at 140:1, while the pH was varied (9, 10, and 10.5) as well as reaction itme (9, 12, and 15 h). The EITC:SA ratio was calculated from UV-Vis analysis after conjugation of absorbance values at 280 and 530 nm. **Figure A-3.1** shows the results of the varied pH and reaction time experiment. This figure suggests that the reaction time in the range examined is not a significant parameter affecting DOS. However, the reaction pH did significantly affect the DOS, as increasing the pH from 9 to 10 almost doubled the DOS. The data suggests that increasing the reaction above 10 to 10.5 does not have a significant effect on the DOS, as here the increase only yielded ~10% increase in the DOS. Another experiment examined the reactant molar ratio as it

was increased above the original ratio of ~140:1 from the protocol originally reported by Hansen et al. (2007). **Figure A-3.2** shows the results of this experiment, and indicates that molar ratio does increase the reaction DOS. When the molar ratio is doubled, the DOS increases by approximately 1.5-fold. From these studies, it was concluded that a reaction time of 9 hours, a reaction pH of 10, and a reactant molar ratio of 140:1 would be sufficiently to yield a SA-EITC conjugate for cell labeling in ASL experiments.

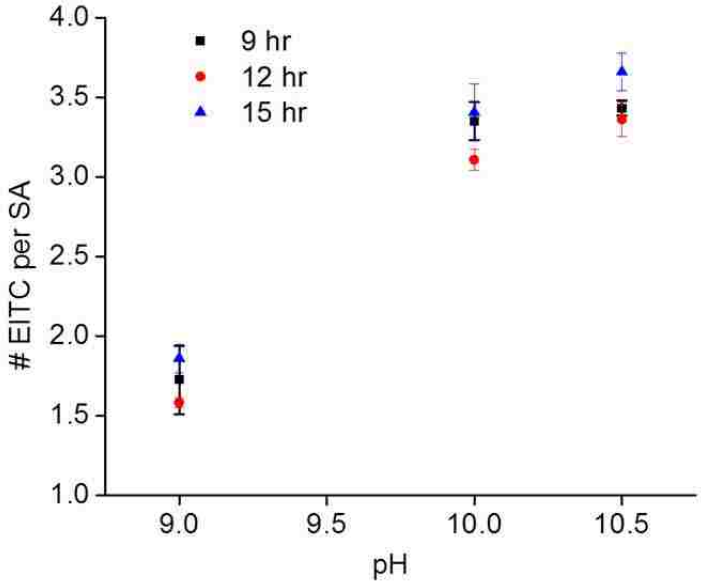

Figure A-3.1 The effect of reaction time and reaction pH on the DOS of EITC:SA conjugates. Data points are presented as mean, with error bars representing standard error for N=3.

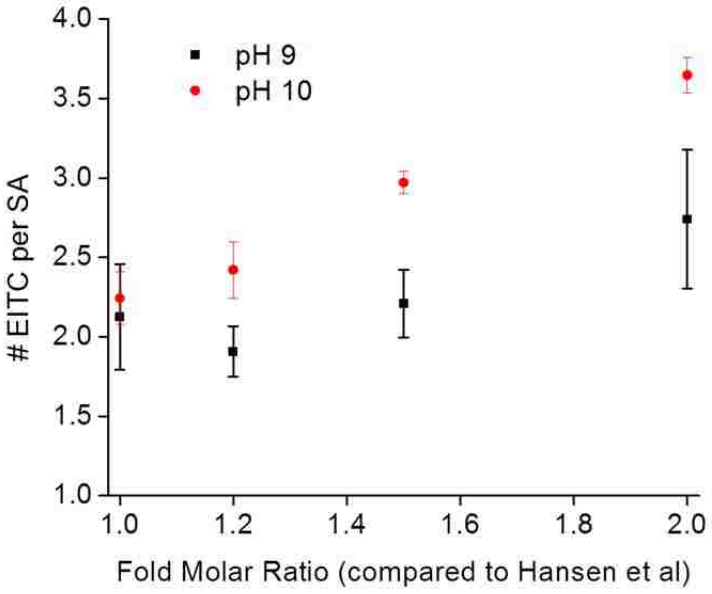

Figure A-3.2 Effect of reactant (free EITC to SA) molar ratio on DOS at pH 9 and 10 for a constant reaction time of 12 hours. "Fold Molar Ratio" refers to the fold increase in molar ratio over the original protocol that was adapted for this work found in Hansen et al. (2007) [98]. Data points are presented as mean, with error bars representing standard error for N=3.

A-4 General Orientation of Printed Protein Microarrays

Printed protein microarrays are used in the preceding chapters to investigate the gelation response to varied monomer formulations and photoinitiator surface densities. A general layout for these microarrays is shown below in **Figure A-4.1**. Pre-functionalized epoxy microscopy slides are purchased and washed once with 100% ethanol. Slides are loaded into an Affymetrix 417 Array Printer, where serial dilutions of biotinylated bovine serum albumin (bBSA) are printed identically on each slide. As shown below, each of the 12 concentrations are printed in duplicate on each array, with 4 replicate arrays printed on each slide. **Figure A-4.2** shows the bBSA print concetration corresponding to the array spotting configuration. In all printing scenarios, the total protein concentration is kept constant at 1000 μg/ml, with proportions of bBSA and BSA being prepared at varied ratios to serially modify the eventual biotin surface density on printed microarrays.

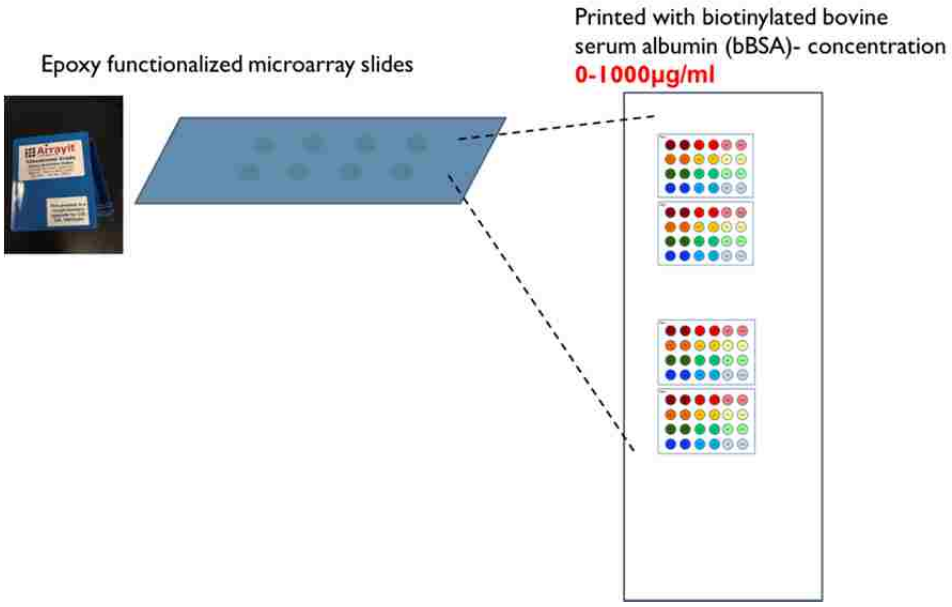

Figure A-4.1 General setup of biotinylated BSA protein microarrays. Array spot color indicates different concentrations.

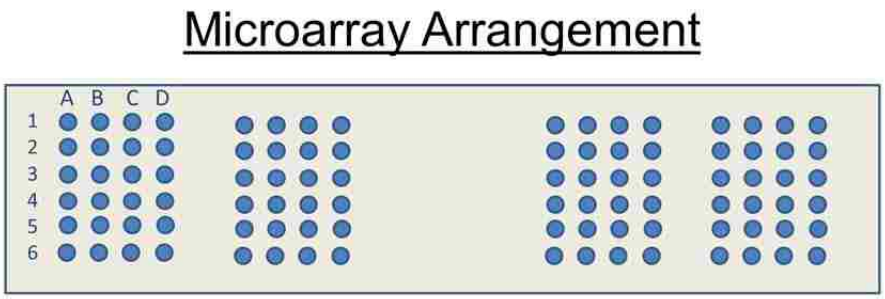

Row/Column	A	B	C	D
1	160 $\frac{\mu g}{mL}$	10.24 $\frac{\mu g}{mL}$	.655 $\frac{\mu g}{mL}$	0 $\frac{\mu g}{mL}$
2	160 $\frac{\mu g}{mL}$	10.24 $\frac{\mu g}{mL}$	.655 $\frac{\mu g}{mL}$	0 $\frac{\mu g}{mL}$
3	400 $\frac{\mu g}{mL}$	25.6 $\frac{\mu g}{mL}$	1.64 $\frac{\mu g}{mL}$	.105 $\frac{\mu g}{mL}$
4	400 $\frac{\mu g}{mL}$	25.6 $\frac{\mu g}{mL}$	1.64 $\frac{\mu g}{mL}$	.105 $\frac{\mu g}{mL}$
5	1000 $\frac{\mu g}{mL}$	64 $\frac{\mu g}{mL}$	4.09 $\frac{\mu g}{mL}$	.262 $\frac{\mu g}{mL}$
6	1000 $\frac{\mu g}{mL}$	64 $\frac{\mu g}{mL}$	4.09 $\frac{\mu g}{mL}$	.262 $\frac{\mu g}{mL}$

Figure A-4.2 Concentrations of biotinylated BSA corresponding to the designed microarray configuration.

A-5: Interfacial Polymerization for Colorimetric Labeling of Protein Expression in Cells

The following section is adapted with minor changes from work previously published:

> Jacob L. Lilly, Philip R. Sheldon, Liv J. Hoversten, Gabriela Romero, Vivek Balasubramaniam, Brad J. Berron. Interfacial Polymerization for Colorimetric Labeling of Protein Expression in Cells. PLOS ONE. 9(12): e115630, 2014.

A-5.1 Introduction

The determination of spatial patterns of protein expression in biological samples is a cornerstone of modern clinical diagnostic and biological research. Protein identification and localization is typically achieved through incubation of the sample with labeled antibodies against the protein of interest. While direct labeling of the target antibody is sufficient for localization of abundant proteins in fluorescent imaging, amplification of the signal is typically required to label proteins for brightfield observation of samples where dilute proteins can be difficult to observe colorimetrically. Horseradish peroxidase (HRP) amplification is a common method for amplifying the label of a poorly expressed protein in cells and tissues. The basic concept uses the incubation of HRP enzyme coupled to antibody location, typically through biotinylated antibodies and HRP-avidin conjugates [174]. The specificity of the antibody binds the enzyme to regions expressing the protein of interest. When the sample is subsequently immersed in a solution of hydrogen peroxide and diaminobenzidine, the HRP rapidly converts the diaminobenzidine to yield an insoluble brown product. Under ideal conditions, the presence of the brown product is isolated to regions of expression of the target protein. Unfortunately, nonspecific HRP signal is common from endogenous

peroxidases naturally residing in the tissue [175]. The presence of these active enzymes in the sample tissue requires additional sample processing to quench their activity [176]. Incomplete quenching can lead to false positives or inconclusive staining. Further, fine localization of HRP staining is an empirical process, where over-amplification commonly results in significant diffusion of the signal away from the targeted protein expression.

Polymerization based amplification (PBA) recently emerged as a signal amplification approach which does not suffer from diffusional loss of localization or endogenous signal [96, 177]. PBA uses interfacial polymerization as the basis for depositing a large amount of label at the site of a biological recognition event (e.g. antibody/antigen) [141, 178-180]. Both the presence of a polymerization initiator and reactive monomers are required for the formation of polymer. The PBA approach couples the spatial localization of the polymerization initiator to that of a specific protein recognition event (**Figure A-5.1**). Wherever the antibody recognizes the target protein, a polymerization initiator is immobilized. Upon addition of monomer and the appropriate excitation energy, a polymer coating is formed through the deposition of many monomers at the site of an initiation event. The process has been previously demonstrated on microarrays to specifically form polymer films from as few as 3 binding events per square micron allowing great sensitivity and specificity at antibody concentrations that will limit non-specific background staining [97]. PBA has limitations with respect to sample archival. On cells, PBA has exclusively utilized fluorescent visualization of polymerization events [97, 100]. While PBA has shown strong stability of fluorescent signal during standard imaging conditions, a colorimetric stain would be advantageous for long-term sample storage and archiving.

Here, we seek to adapt PBA to serve as a colorimetric, signal-amplification scheme. Our general approach, termed Polymer Dye Labeling involves the specific loading of the interfacial polymer with dyes. The interfacial polymer typically used in PBA is Polyethylene glycol diacrylate (PEG diacrylate), which has been demonstrated to have specific staining with common dyes [80, 124, 141, 181]. Literature shows both Evans Blue[80] and eosin[180] to be effective in staining PEG diacrylate polymers. In particular, the Sikes group has established the use of eosin stained microarrays for colorimetric assays of oligonucleotide and protein expression, with strong signal to noise [141, 180, 182]. Critically, the ability of eosin to non-specifically stain many cellular components present in biological samples[183] precludes its use in Polymer Dye Labeling to detect specific targeted cellular substrates. We seek to develop a dye system of comparable staining intensity to the eosin dye, but with reduced affinity for common cellular components in biological cells. In all, Polymer Dye Labeling is expected to draw from the advantages of PBA (large signal, excellent localization, and specificity of action) while adding colorimetric capability to allow improved sample archiving.

Our evaluation of Polymer Dye Labeling builds on prior PBA technology [94, 96, 97, 99, 100, 124, 178, 179, 184-186]. We first confirm the expected process of PBA through quantifying the deposition of initiator and polymer on control glass surfaces. We then examine the loading of eosin and Evans Blue dyes into these interfacial coatings through quantification of color change. We then extend this work to the labeling of cells by Polymer Dye Labeling. On a culture of human dermal fibroblast samples, we confirm the stability of the Polymer Dye Labeling signal over 200 days, and also demonstrate the

compatibility of the Polymer Dye Labeling technology with conventional mounting media used in sample archiving.

A-5.2 Materials and Methods

A-5.2.1 Materials

Epoxy functionalized slides were purchased from CEL Associates. Biotinylated bovine serum albumin (bio-BSA), streptavidin, eosin-isothiocyanate, eosin-y, Monoclonal mouse IgG1 anti-vimentin (V9; catalogue #V6389), 10× phosphate-buffered saline (PBS), Triton-X 100, trypsin, hydrogen peroxide (30 wt% solution), PEG diacrylate (Mn = 575), triethanol amine, and 1-vinyl-2-pyrrolidinone were purchased from Sigma Aldrich (St Louis, MO). Monoclonal mouse IgG1 anti-NPC (MAb414) was purchased from Covance (Princeton, NJ; catalogue #MMS-120P). Biotinylated polyclonal goat IgG anti-mouse IgG (H+L; catalogue #BA-9200) and Vectashield hardset mounting medium was purchased from Vector Laboratories (Burlingame, CA). Bovine serum albumin (BSA), methanol, and ethanol (absolute) were purchased from Fisher Scientific (Waltham, MA). Paraformaldehyde was purchased from Electron Microscopy Sciences (Hatfield, PA). Streptavidin-Alexa488 conjugates were purchased from Life Technologies (Grand Island, NY). Rabbit antibodies against mouse pro-surfactant protein C was purchased from Seven Hills Bioreagents (Cincinnati, OH). Donkey antibodies against rabbit IgG were purchased from Invitrogen (Carlsbad, CA).

RPMI-1640 cell culture media was purchased from Cellgro and supplemented with 10% fetal bovine serum (FBS, Gibco, Carlsbad, CA), 100U/mL Penicillin, 10 mg/mL Streptomycin (Gibco) prior to use. Normal human dermal fibroblasts (#CC-2511) were purchased from Lonza (Basel, Switzerland). Streptavidin-eosin (SA-initiator) was

prepared as described previously [178]. PBSA was prepared by adding 1 mg/mL bovine serum albumin 1x PBS. Monomer mix was prepared immediately prior to use and consists of 25 wt% PEG diacrylate, 21 mM triethanolamine, 35 mM 1-vinyl-2-pyrrolidinone, and 0.05 wt% Nile red fluorescent nanoparticles in deionized water.

A-5.2.2 Biotin Microarray Printing

Epoxy functionalized glass slides were rinsed with ethanol, dried under a stream of nitrogen, and placed on the stage of the Affymetrix (Santa Clara, CA) GMS 417 Arrayer. BSA solutions were prepared keeping a constant 1 mg/mL concentration of BSA in PBS, and varying the fraction of BSA that is biotinylated . Twelve solutions were prepared at the following concentrations of biotinylated BSA: 1 mg/mL, 400 μg/mL, 160 μg/mL, 64 μg/mL, 26 μg/mL, 10 μg/mL, 4 μg/mL, 1.6 μg/mL, 650ng/mL, 260 ng/mL, 100 ng/mL, 0 ng/mL. Arrays consisted of 24 spots, where each solution was duplicated on each array, and four identical arrays were printed on each glass slide. Only the two centermost arrays were used, as the polymerization light source can only irradiate two arrays at a time. Slides were printed under 60% relative humidity in a single batch of 25 slides.

A-5.2.3 Microarray Polymerization, Staining, and Imaging

Slides were blocked in PBSA for 10 minutes, incubated in 1.0 μg/mL SA-initiator in PBSA for 20 minutes, and rinsed with PBSA. These initiator-labeled arrays were then scanned in an Affymetrix Microarray Scanner (Model 428) using 532 nm laser excitation and a 551 ± 7 nm band pass emission filter. Files were exported to ImageJ for analysis of array spot intensity. Fluorescent data are reported as the mean and standard deviation of

16 measurements (two duplicates spots per array, two arrays per slide, four independent preparations of a single slide).

Slides were then immediately placed in a Chip Clip (Whatman, Little Chalfont, UK) with a two well FAST slide (Whatman) with 400 μL of monomer mix in each well. Samples were purged with humidified nitrogen in a clear plastic bag for 5 minutes. Then, the slide was irradiated for 20 minutes with collimated, 10 mW/cm^2, 530 nm LED light (Thorlabs, Newton NJ, model M530L3) under a constant stream of humidified nitrogen. After irradiation, samples were rinsed with water. The samples were then incubated in a 1 mg/mL solution of the indicated dye for 20 minutes. Evans Blue was prepared in PBS, while eosin was prepared in an aqueous solution of 50% methanol to promote solubility. Slides were dried under a stream of nitrogen, and imaged using an Epson Perfection 4490 Photo flat-bed document scanner at a resolution of 2400 dpi. Only the two arrays most-centered under the LED irradiation were analyzed owing to radial non-uniformities in the irradiation intensity. Greyscale values of the fractional darkness of each spot were collected for each spot using ImageJ. Fractional darkness is defined as 1.00 minus the fractional greyscale value of spot brightness. The thickness of each polymer spot was measured with a Dektak 6M stylus profilometer. Limit of detection is defined as the lowest concentration of biotinylated BSA of a different mean when compared to the lower concentrations with at least 95% confidence by student t-test. The saturation range is defined as the high concentration range of biotinylated-BSA where the mean measurement is not different from each other with at least 95% confidence by a student t-test. The dynamic range is defined as the concentration range between the limit of detection to the saturation region.

A-5.2.4 Immunolabeling of Cells

Dermal fibroblasts were cultured on 8 well chamber slides in media at 37 C in 5% CO_2 until ~80% confluent. The cells were rinsed with cold PBS, and fixed in 4% paraformaldehyde in PBS for 10 minutes. Fixed cells on chamber slides were stored in PBS at 4 ºC for up to 30 days prior to use with no observed change in staining intensity. Cells were permeablized with 0.1% Triton X-100 in PBS for 5 minutes and blocked with PBSA for 10 minutes. Then, slides were incubated in the appropriate primary antibody at the appropriate dilution in PBSA (anti-NPC at 1:1,000 or anti-vimentin at a 1:5,000) for 40 minutes and rinsed with PBSA. The cells were contacted with biotinylated antibodies against mouse IgG at 1:400 dilution in PBSA for 4 minutes and rinsed with PBSA. These samples were then ready for either Polymer Dye Labeling or control labeling with Alexa488.

For Polymer Dye Labeling, the cells were incubated in a 25 μg/mL solution of SA-initiator in PBSA for 20 minutes and rinsed with PBS. 80 μL of monomer mix was added to each well, and the slides were polymerized for 20 minutes with collimated, 10 mW/cm^2, 530 nm LED light (Thorlabs model M530L3) under a constant stream of humidified nitrogen. After irradiation, samples were rinsed with water, and incubated in a 1 mg/mL solution of Evans Blue dye in PBS for 20 minutes. Samples were briefly rinsed with PBS, and then imaged on a Nikon (Tokyo, Japan) Ti-U inverted microscope using a 60x oil immersion objective with a Nikon DS-Ri1 12 MP cooled color CCD camera.

For control experiments, cells labeled with biotinylated secondary antibodies were contacted with 1 μg/mL streptavidin-Alexa488 in PBSA for 20 minutes and were

immediately imaged on a Nikon Ti-U inverted microscope as before except with epifluorescent imaging in the FITC channel.

Greyscale values of the fractional darkness of each spot were collected for each spot using ImageJ. Fractional darkness is defined as 1.00 minus the fractional greyscale value of spot brightness. Background (non-cell region) darkness was subtracted from both the signal (nucleus region) and noise (cytoplasm region). Signal to noise is defined by the division of the signal value by the noise value.

A-5.3 Results and Discussion

Our goal is to develop a colorimetric alternative to enzymatic amplification which is not hampered by non-specific amplification by endogenous enzymes or through diffusional loss of signal localization. Our approach, "Polymer Dye Labeling," is a multi-step process where 1) polymerization initiator is localized to the site of antigen expression, 2) an interfacial polymer coating is grown from the surface-grafted initiator, and 3) dye is loaded into the polymer. Our approach is to first study the fundamental relationship between initiator binding and the intensity of Polymer Dye Labeling. Then, we investigate the comprehensive Polymer Dye Labeling process when applied to the labeling of protein expression in cultured human dermal fibroblasts.

A-5.3.1 Characterization of Recognition, Polymerization, and Dye Association

Bio-BSA was printed into microarrays on an epoxy coated slide, and blocked with PBSA. Recognition of the SA-initiator with the biotin of the bio-BSA, was quantified through measuring the fluorescence of the eosin initiator in biotin-expressing regions. A solution of the SA-initiator conjugate at 1 μg/mL in PBSA was contacted with each microarray for 20 minutes, and excess conjugate was rinsed briefly with PBSA prior to

capturing a fluorescent image with a microarray scanner (**Figure A-5.2.a**). The fluorescence of each spot was measured using ImageJ, and plotted against the corresponding concentration of Bio-BSA in the printing solution (**Figure A-5.2.b**). The relative initiator concentration is indistinguishable from the background at printed solution concentrations less than 10^{-3} g/L of Bio-BSA (limit of detection, $p=10^{-14}$). There is a two log fluorescent dynamic range, and saturation above 10^{-1} g/L of Bio-BSA ($p=.043$). Initiator binding is restricted to printed regions, and printed spots containing only BSA did not exhibit fluorescence greater than that of non-printed regions. The specificity of binding in this study is consistent with previous reports of initiator binding based on antibody-antigen [97, 100, 185] or Streptavidin-biotin interactions [178, 184].

Interfacial polymerization is accomplished through the immersion of an initiator-primed surface in a PEG diacrylate monomer solution. Polymerization proceeded with a 20 minute exposure to 10 mW/cm^2, 530 nm irradiation under a nitrogen atmosphere. The resulting arrays of polymer spots were measured by profilometry to determine the sensitivity and magnitude of the polymerization reaction (**Figure A-5.2.c**). As expected, polymer growth was restricted to regions of initiator-labeling, supporting the specificity of the polymerization process. The limit of detection was identical to that of the fluorescence arrays (10^{-3} g/L of Bio-BSA, $p= .001$). The dynamic range of polymer thickness extended to 10^{-1} g/L of Bio-BSA ($p=.01$), and was identical to that of the dynamic range of initiator concentration on the surface, supporting prior reports of the polymerization reaction being limited by the initiator concentration [141].

Incubation of the PEG diacrylate hydrogels in a dye is expected to alter the color of the polymer. We are investigating Evans Blue as a candidate dye for strong specific

staining of the polymer with minimal nonspecific staining of cellular material. Arrays of PEG diacrylate polymer films were incubated in 1 mg/mL Evans Blue for 20 minutes, and upon removal, the polymer spots were darkened, while the surrounding glass slide remained unstained (**Figure A-5.3.a**). The darkness of the spots was quantified and plotted against the printed concentration of bio-BSA (**Figure A-5.3.c**). Again, the limit of detection was identical to that of the polymer thickness and the initiator concentration (10^{-3} g/L of Bio-BSA, p=0.0004). Critically, the dynamic range of the staining was negligible, and saturation range began at the next data point ($4x10^{-3}$ g/L of Bio-BSA, p= 0.008). As a result, the colorimetric response was largely binary. When compared to the use of 1 mg/mL eosin as the polymer dye (**Figure A-5.3.b, A-5.3.d**), Evans Blue has a greater magnitude of colorimetric labeling ($p= 10^{-63}$) of the polymer stained regions but different levels of background staining ($p= 10^{-5}$). The limit of detection (10^{-3} g/L of Bio-BSA, p= 0.0008) and beginning of the saturation range (10^{-2} g/L of Bio-BSA, p= 0.0008) for eosin are similar to the Evans Blue labeling. This indicates Evans Blue is a potential alternative to eosin in colorimetric staining of PEG diacrylate hydrogels in microarray settings. The use of eosin dyes on hydrogel microarrays has already demonstrated effectiveness in a colorimetric detection of biological species [141], and the use of a blue dye may improve ease of use over the pink color associated with eosin-dyed hydrogels.

To directly compare the effectiveness of the dye-labeling step, we related the darkness of each spot to the thickness of the hydrogel at that location, providing a relationship of how much dye is absorbed per unit thickness by the PEG diacrylate hydrogels. Applying a linear relationship (slope =$1.78x10^{-4}$ darkness units per nm) to the Evans Blue data is consistent with the expected increase in spot darkness with a longer

path length through the dyed polymer (**Figure A-5.4.a**), yet this fit is statistically different than the data (p=.01), indicating a poor fit. A linear relationship ($2.7x10^{-4}$ darkness units per nm) is observed for the eosin-dyed polymer spots (Figure 4b), without a statistical difference between the data and the linear fit (p=0.06). Additionally, the eosin associated with the initiator is not perceptible through visual observation prior to immersion of the hydrogel in eosin. All darkness of the spot is attributed to the post-polymerization dying. While the magnitude of the spot darkness is higher for the eosin dyed spots than the Evans Blue dyed spots, there is a comparable difference in nonspecific darkness on the glass slide. Here, we show the eosin labeling of the polymer is specific. In previous studies, greater signal to noise has been reported by others through the use of 20-fold higher concentrations of eosin [180]. Higher concentrations of eosin or Evans Blue were not used in the present study, in an effort to limit nonspecific staining in subsequent cell studies.

The diameter of the dye labeled polymer spots was determined by optical microscopy to be 340 ± 20 μm (**Figure A-5.3.a, A-5.3.b**), and this value was within measurement error of the spot size of the original initiator labeled arrays of 350 ± 20μm (**Figure A-5.2.a**). The lack of detectible polymer overgrowth is promising for the localization of the polymer to the site of protein expression.

A-5.3.2 Labeling of Protein Expression in Cells

The transition from a controlled microarray environment to a biological substrate introduces additional challenges to label specificity. Every step in the amplification process must be specific to the region of antibody/antigen recognition. For the localization of the initiator, the specificity is dictated by specific binding of the antibodies

and the SA-initiator complex [96]. When antibodies against nuclear pore complex (NPC) are used on a fixed, permeabilized, and blocked dermal fibroblast, the initiator fluorescence is isolated to the nuclear membrane (**Figure A-5.5.c**). When the NPC primary antibodies are replaced with antibodies against vimentin, the initiator fluorescence is localized to vimentin, a fibrous structural component which stretches across the cytoplasm (**Figure A-5.5.d**). Control experiments using standard streptavidin-Alexa488 instead of the SA-initiator show identical patterns of expression (**Figure A-5.5.a, A-5.5.b**), supporting the appropriate protein specificity of the initiator localization. The signal intensity from labeling with SA-initiator (signal to noise 4.53 ± 0.36) and streptavidin-Alexa488 (signal to noise 4.23 ± 0.80) are fully described in **Table A-5.2**. These findings are consistent with prior work in polymerization amplification [100, 178].

Upon addition of the PEG diacrylate monomer mix to the initiator-labeled cells and irradiation with 10 mW/cm^2, 530 nm (green) light, an interfacial polymer is formed on only surfaces expressing the target protein. Unreacted monomer is rinsed away with PBS, and the polymer-labeled cells are immersed in 1 mg/ mL Evans Blue in PBS. While both eosin and Evans Blue are capable of specific staining in a microarray setting, the non-specific staining of eosin for cytoplasmic proteins and collagen precludes its use for Polymer Dye Labeling on most biological substrates [183]. As such, only Evans Blue was used in the cell staining studies. In the case of NPC labeled cells, the blue staining of the Polymer Dye Labeling (**Figure A-5.5.e**) is consistent with the fluorescent control NPC staining, where the nuclear membrane is labeled. Similarly, the Polymer Dye Labeling of vimentin is specific to these cytoskeletal components, with appropriate alignment of fibers towards cellular extensions (**Figure A-5.5.f**). Taken together, the

cellular labeling studies are supportive of the specificity of Polymer Dye Labeling in biological environments. Further, the intensity of staining is consistent with the expected amplification resulting from the reaction of many monomers at the site of initiation.

In the context of biological research, colorimetric staining allows independence from fluorescent analysis and associated costs. Colorimetric staining is almost exclusively accomplished with enzymatic amplification of the label and enzymatic labeling has the fundamental challenge of nonspecific labeling from endogenous enzymes and diffusion. Importantly, our work was performed in the absence of any additional steps to quench endogenous enzyme activity, as the routes for nonspecific polymerization initiation are currently undetected. A limitation of the current embodiment of polymer dye labeling is the need for a photopolymerization light source. The light source utilized here (Thorlabs LED, <$1000 US) is significantly less expensive than a fluorescent microscope which requires additional filters and optics. Further, other modes of polymerization based amplification are based on non-light driven polymerizations [124, 177, 186-190]. The future incorporation of ATRP or other modes of polymerization would further reduce the capital cost of polymer dye labeling.

A-5.3.3 Suitability for Sample Archiving

Signal stability is a major advantage of a colorimetric staining over a fluorescent approach. We challenged the stability of cells polymer dye labeled cells with storage at ambient conditions. Specifically, the samples were imaged immediately after Polymer Dye Labeling for nuclear pore complex and again after being stored in a drawer for 208 days (**Figure A-5.6**). The darkness of the nucleus when stained (0.363 ± 0.088) is comparable to the darkness of the nucleus 208 days after the staining (0.343 ± 0.091).

The only observable differences between the images were a slight reorientation of the frame and an increase in small optical aberrations attributed to environmental contaminants (dust, bacteria, etc.). The storage had no significant impact on the intensity or localization of staining, indicating promise for the application of Polymer Dye Labeling to long term sample archiving.

We also evaluated the stability of Polymer Dye Labeling signal when using a mounting medium. Prior studies using fluorescent PBA to label proteins has been exclusively executed in the absence of mounting medium, as the fluorescence is completely quenched in the presence of mounting media [100]. This is a significant limitation, as mounting medium is commonly integrated into conventional imaging and archiving protocols to improve image quality and to preserve signal.

NPC expression was stained through four variants of Polymer Dye Labeling: dry with Evans Blue, mounted with Evans Blue, dry without Evans Blue, and mounted without Evans Blue. Images are presented in **Figure A-5.7**, while the darkness of the stain in these images was measured with ImageJ and compiled in **Table A-5.1**. For dry imaging of Polymer Dye Labeling, a blue nucleus is clearly observed (signal / noise ~7) in contrast to minimal nonspecific signal in the cytoplasm (**Figure A-5.7.a**). Vectashield hardset mounting medium was added to the sample according to manufacturer's instructions, coverslipped and imaged (**Figure A-5.7.b**). While the overall darkness of the stain decreased, the signal/noise almost tripled that of the dry Polymer Dye Labeling. This is attributed to a large decrease in the nonspecific staining of the cytoplasm.

The most striking change with sample mounting was the change in color of the Polymer Dye Labeling from blue to violet. To verify this different color of labeling is

attributed to the use of the Evans Blue dye, we polymerized in response to NPC with the omission of the Evans Blue dye (**Figure A-5.7.c**). This dry, undyed sample shows negligible signal yet did impart some contrast in the image, owing to the change in refractive index between the polymerized nucleus and the background. Upon addition of mounting medium to this sample, a slight violet tint is imparted on the interfacial polymer covering the nucleus (**Figure A-5.7.d**). The magnitude of the mounting medium's contribution to the signal is low (signal/noise ~1), supporting the Evans Blue dye as the dominant mechanism for staining. As the dark violet color of the polymer is only observed when both Evans Blue and mounting medium are used, it is likely the change in the chemical environment of the dye is altering the absorption characteristics. Similar shifts in absorption peak position are commonly observed in many light-absorbing molecules (photoinitiators [191], fluorophores [192, 193], etc.) with a change in solvent.

While enzymatic amplification methods are also stable over prolonged times and are compatible with modern sample archiving methods, polymerization based methods have greater site-specificity than enzymatic amplification [100]. The present findings clearly address the prior limitations in archiving of polymerization amplification samples, delivering a plausible path forward for a new colorimetric technique with all of the positive attributes of both enzymatic and polymerization techniques.

A-5.4 Conclusions

Polymer Dye Labeling is based on interfacial polymerization which is specific to the site of the targeted protein, and these target-specific polymer coatings are then stained with Evans Blue dye. As a result, a dye-loaded polymer is isolated to regions of protein

expression. In microarray studies, the use of Evans Blue provides a comparable contrast to an unstained background as eosin dyes. Application of Polymer Dye Labeling to immunostaining of cultured cells allowed bright field observation of both the spatial protein expression and cell morphology. The labeling of protein expression is stable over several months. Prior polymerization labeling approaches were incompatible with mounting medium, but Polymer Dye Labeling maintains signal intensity and localization in common mounting media. We conclude that Polymer Dye Labeling will allow colorimetric visualization of the spatial localization of targets within a cell to leverage the highly sensitive and specific aspects of Polymerization Based Amplification.

Table A-5.1: Staining intensity for Polymer Dye Labeling of nuclear pore complex.

Sample	Signal [a,c]		Noise [b,c]		Signal / Noise	
	Mean	Standard Deviation	Mean	Standard Deviation	Mean	Standard Deviation
Polymer Dye Labeling dry	0.333	0.009	0.049	0.004	6.9	0.7
Polymer Dye Labeling Mounted	0.191	0.016	0.010	0.003	20.9	8.2
Polymer Dry	-0.001	0.001	-0.004	0.002	0.2	0.6
Polymer Mounted	0.016	0.006	0.005	0.014	1.2	2.3

[a] - Signal is defined as the darkness of the nucleus.
[b] - Noise is defined as the darkness of the cytoplasm.
[c] - Values are relative increase over empty region of slide.

Table A-5.2: Staining intensity for immunofluorescent labeling of nuclear pore complex.

Sample	Signal [a,c]		Noise [b,c]		Signal / Noise	
	Mean	Standard Deviation	Mean	Standard Deviation	Mean	Standard Deviation
Streptavidin-488 Labeling	0.146	0.028	0.035	0.006	4.23	0.80
Streptavidin-eosin Labeling	0.101	0.008	0.022	0.007	4.53	0.36

[a] - Signal is defined as the brightness of the nucleus.
[b] - Noise is defined as the brightness of the cytoplasm.
[c] - Values are relative increase over empty region of slide.

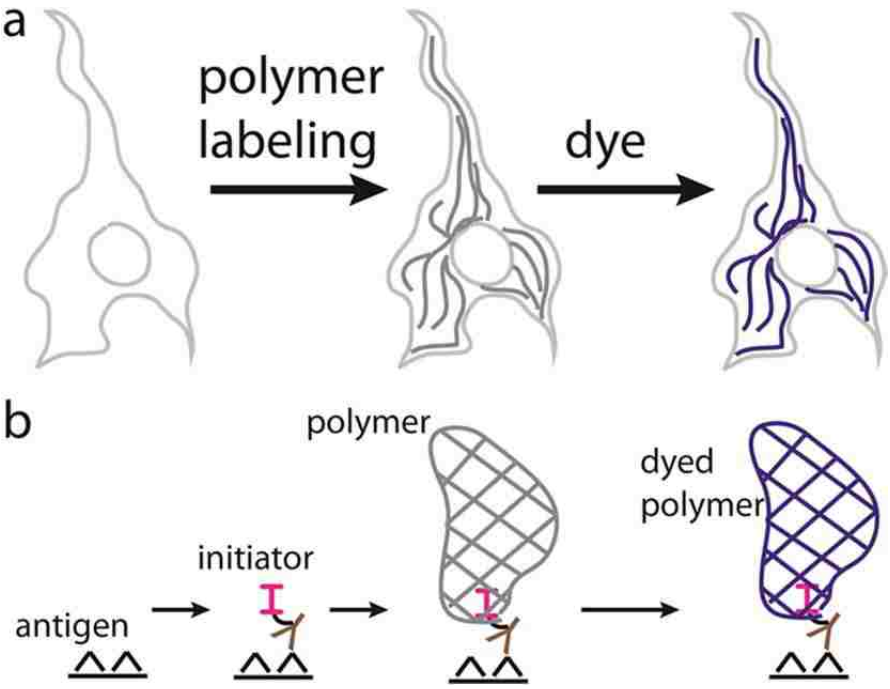

Figure A-5.1: Polymer Dye Labeling concept at the (a) cellular level and (b) molecular level. A polymerization initiator is localized to site of antigen through antibody and biotin-streptavidin labeling. Interfacial hydrogel polymerization occurs only at regions labeled with initiator. The hydrogel is colorimetrically labeled through an affinity dye.

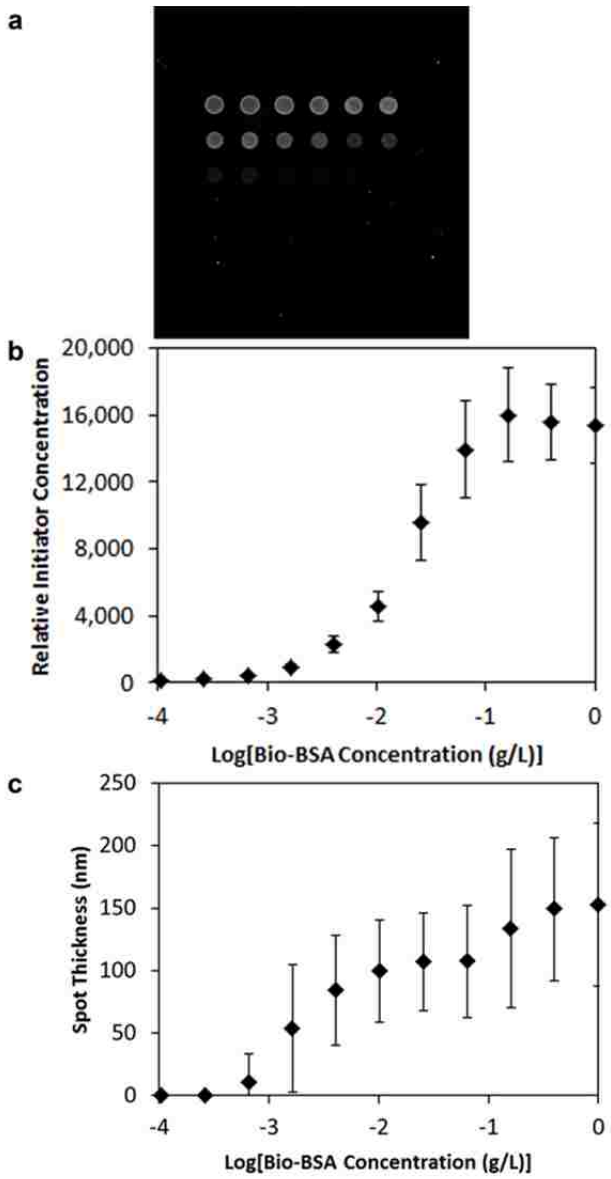

Figure A-5.2: Imaging of initiator concentration for microarray. a) Fluorescent microarray scanner measuring relative abundance of initiator prior to polymerization labeling. Scale bar = 1 mm. b) Relative initiator concentration on surface for spots printed from the indicated concentration of biotinylated-BSA and reacted with the SA-initiator complex. Measurements based on initiator fluorescence (ex/em = 525/545 nm). c) Thickness of spots of indicated Bio-BSA concentration. Data are mean ± standard deviation. n=16.

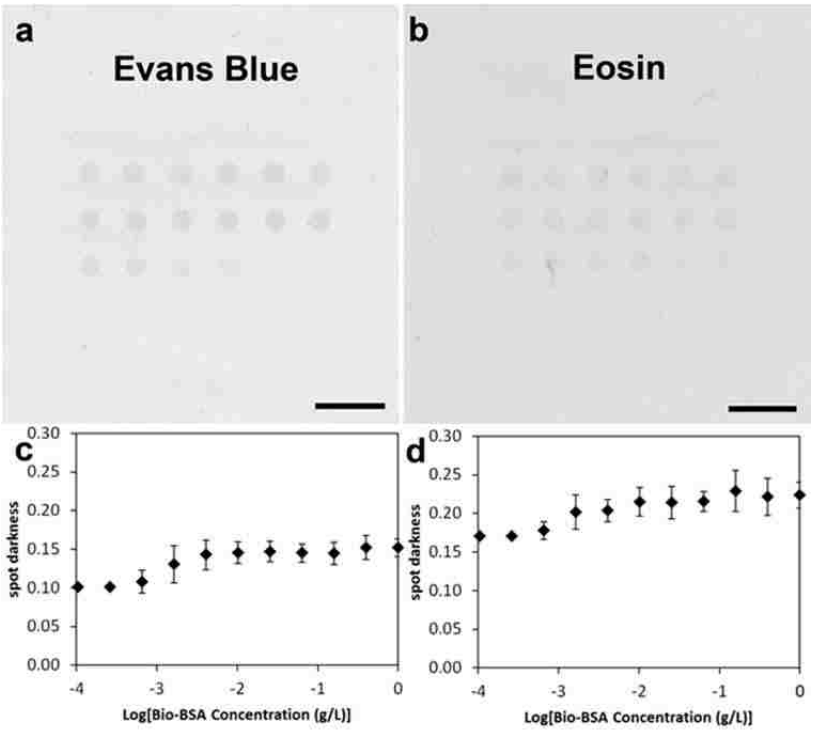

Figure A-5.3: Colorimetric imaging of Polymer Dye Labeling. a) Greyscale image from optical document scanner after Polymer Dye Labeling with Evans Blue dye. b) Greyscale image from optical document scanner after Polymer Dye Labeling with eosin dye. Scale bars = 1 mm. c) darkness of Evans Blue dyed spots of indicated Bio-BSA concentration. d) Darkness of eosin dyed spots of indicated Bio-BSA concentration. Data in c) and d) are mean ± standard deviation. n=12.

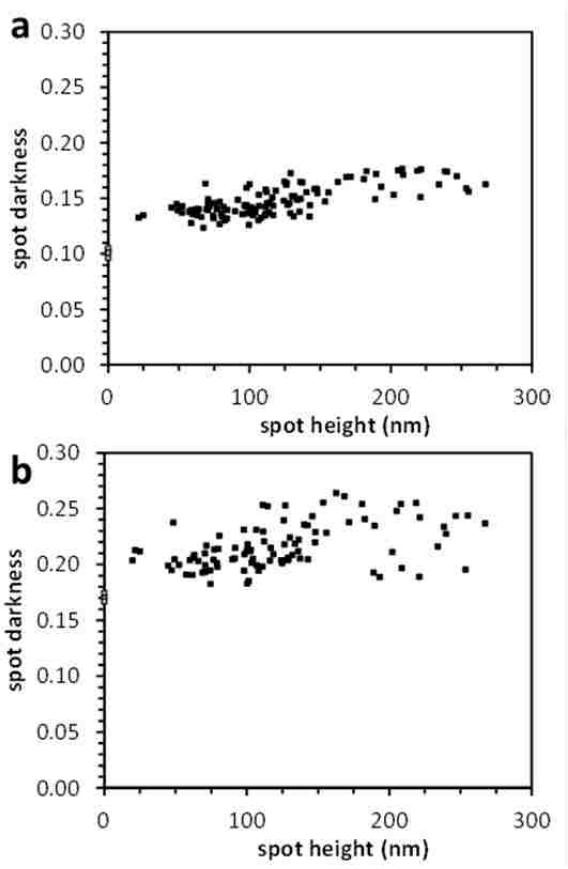

Figure A-5.4: Relationship between polymer spot thickness and spot darkness after Polymer Dye Labeling. a) Polymer Dye Labeling with Evans Blue dye. b) Polymer Dye Labeling with eosin dye. Each data set includes at least 6 microarrays from 3 independent experiments. Black squares indicate array data. Grey squares indicate mean value of non-specific regions for each experiment.

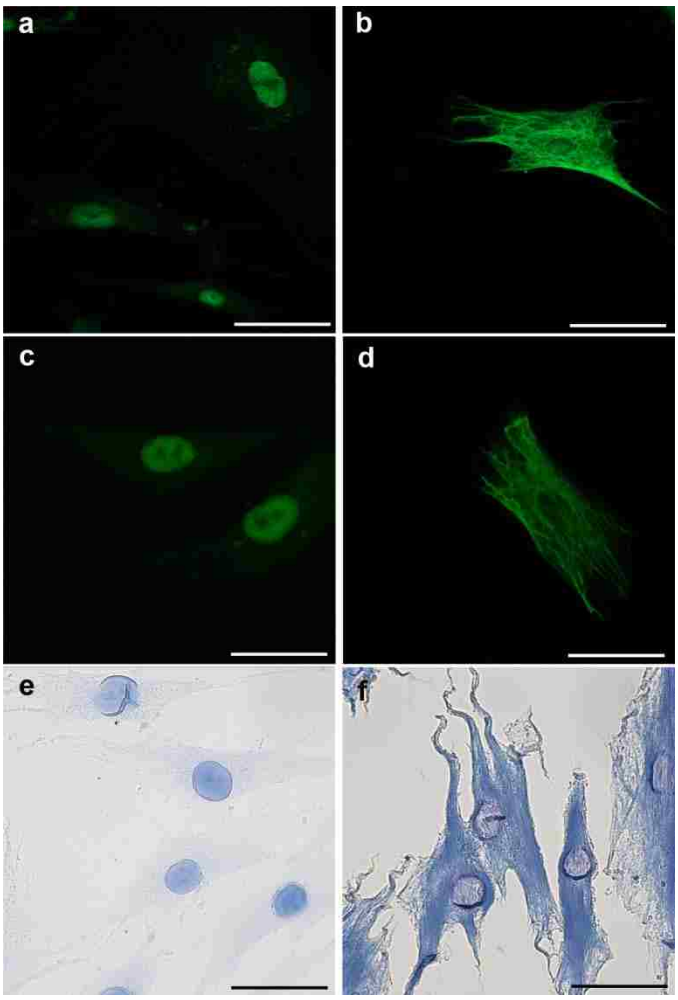

Figure A-5.5: Comparison of Polymer Dye Labeling with immunofluorescent labeling in human dermal fibroblasts. Control fluorescent staining of nuclear pore complex (a) and vimentin (b) using Streptavidin-Alexa488. Initiator localization when using antibodies against nuclear pore complex (c) and vimentin (d). Dyed Polymer localization when using antibodies against nuclear pore complex (e) and vimentin (f). Scale bars are 50 μm.

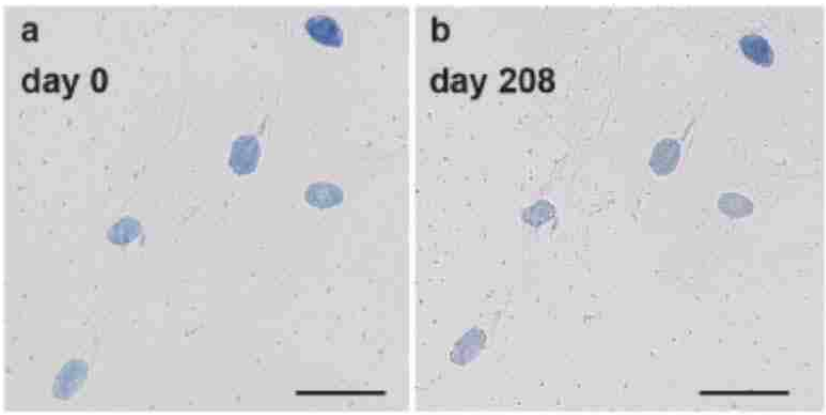

Figure A-5.6: Labeling Stability of Polymer Dye Labeling. Polymer Dye Labeling of nuclear pore complex immediately after staining (a) and 208 days after staining (b). Scale bars are 50 μm.

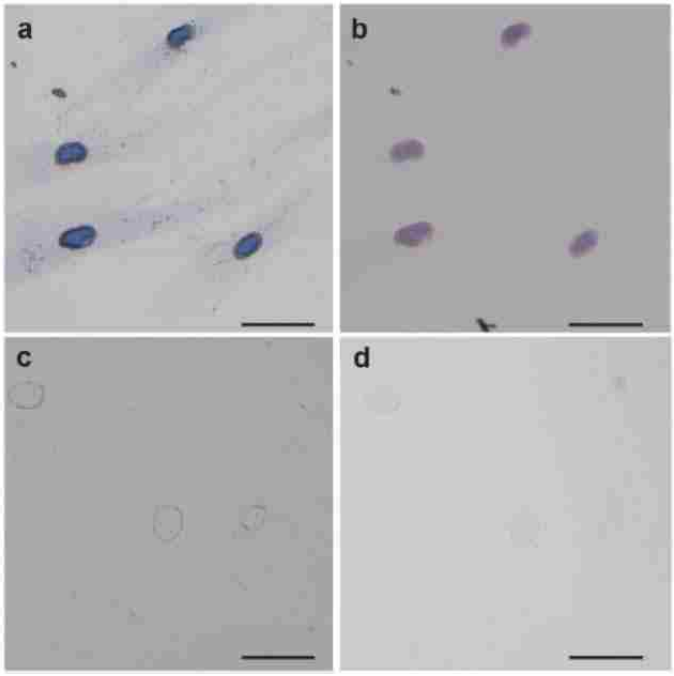

Figure A-5.7: Compatibility of Polymer Dye Labeling with Vectashield mounting medium. Polymer Dye Labeling of nuclear pore complex imaged (a) dry or (b) in Vectashield hardset mounting medium. Polymer coated nuclei without Evans Blue dye imaged (c) dry or (d) in Vectashield hardset mounting medium. Scale bars are 50 µm.

List of Abbreviations

AC	Acryloyl chloride
ASL	Antigen specific lysis
bBSA	Biotinylated bovine serum albumin
BP	Bandpass
BSA	Bovine serum albumin
CK	Cytokeratin
CTC	Circulating tumor cell
DAPI	4',6-diamidino-2-phenylindole
DCM	Dichloromethane
DNA	Deoxyribonucleic acid
DOS	Degree of substitution
DPBS	Dulbecco's phosphate buffered saline
ECM	Extracellular matrix
EDC	1-Ethyl-3-(3-dimethylaminopropyl)carbodiimide
EDTA	Ethylenediaminetetraacetic acid
EGF	Epidermal growth factor
EGFR	Epidermal growth factor receptor
EIA	Enzyme immunoassay
EITC	Eosin-5-isothiocyanate
ELISA	Ezymed-linked immunosorbent assay
EMT	Epithelial-mesenchymal transition
EpCAM	Epithelial cell adhesion molecule
ER-α	Estrogen receptor-α
FACS	Fluorescence activated cell sorting
FBS	Fetal bovine serum
FD	Fluorescein-5-isothiocyanate labeled dextran
FITC	Fluorescein-5-isothiocyanate
GFP	Green fluorescent protein
1H-NMR	Proton nuclear magnetic resonance
HEPES	2-[4-(2-hydroxyethyl)piperazin-1-yl]ethanesulfonic acid
HER1	Human epidermal growth factor receptor 1
HER2	Human epidermal growth factor receptor 2
HGF	Hepatocyte growth factor
ICAM-1	Inflammatory cell adhesion molecule 1
IgG	Immunoglobulin
IHC	Immunohistochemical
LAP	Lithium acylphosphinate
LED	Light emitting diode
MACS	Magnetic activated cell sorting
MEHQ	Monomethyl ether hydroquinone
MW	Molecular weight

MWBC	molecular weight between crosslinks
NHS	*N*-hydroxysuccinimide
NPC	Nuclear pore complex
NSCLC	Non-small cell lung cancer
PBA	Polymer-based amplification
PBMC	Peripheral blood mononuclear cell
PBS	Phosphate buffered saline
PBSA	Phosphate buffered saline with 1 mg/ml bovine serum albumin
PCL	Poly(caprolactone)
PDGF	Platelet derived growth factor
PE	Phycoerythrin
PEG	Poly(ethylene glycol)
PEGDA	Poly(ethylene glycol) diacrylate
PLA	Poly(lactic acid)
PLGA	Poly(lactic-co-glycolic acid)
PLL	Poly(L-lysine)
PVA	Poly(vinyl alcohol)
SA	Streptavidin
SDS	Sodium dodecyl sulfate
SEM	Scanning electron microscopy
TEA	Triethanolamine
TEM	Transmission electron microscopy
TGF-β	Transforming growth factor β
UV	Ultraviolet
VP	1-vinyl-2-pyrrolidinone
ZEB	Zing finger E-box binding homeobox

References

[1] Kalluri R, Weinberg RA. The basics of epithelial-mesenchytnal transition (vol 119, pg 1420, 2009). Journal of Clinical Investigation. 2010;120:1786-.

[2] Ifkovits JL, Burdick JA. Review: photopolymerizable and degradable biomaterials for tissue engineering applications. Tissue Engineering. 2007;13:2369-85.

[3] Nguyen DX, Bos PD, Massagué J. Metastasis: from dissemination to organ-specific colonization. Nature Reviews Cancer. 2009;9:274-84.

[4] Wicha MS, Hayes DF. Circulating tumor cells: not all detected cells are bad and not all bad cells are detected. Journal of Clinical Oncology. 2011;29:1508-11.

[5] Cohen S, Punt C, Iannotti N, Saidman B, Sabbath K, Gabrail N, et al. Prognostic significance of circulating tumor cells in patients with metastatic colorectal cancer. Annals of Oncology. 2009;20:1223-9.

[6] Cristofanilli M, Budd GT, Ellis MJ, Stopeck A, Matera J, Miller MC, et al. Circulating tumor cells, disease progression, and survival in metastatic breast cancer. New England Journal of Medicine. 2004;351:781-91.

[7] de Bono JS, Scher HI, Montgomery RB, Parker C, Miller MC, Tissing H, et al. Circulating tumor cells predict survival benefit from treatment in metastatic castration-resistant prostate cancer. Clinical Cancer Research. 2008;14:6302-9.

[8] Miller MC, Doyle GV, Terstappen LW. Significance of circulating tumor cells detected by the CellSearch system in patients with metastatic breast colorectal and prostate cancer. Journal of oncology. 2009;2010.

[9] Riethdorf S, Fritsche H, Müller V, Rau T, Schindlbeck C, Rack B, et al. Detection of circulating tumor cells in peripheral blood of patients with metastatic breast cancer: a validation study of the CellSearch system. Clinical Cancer Research. 2007;13:920-8.

[10] van de Stolpe A, Pantel K, Sleijfer S, Terstappen LW, den Toonder JM. Circulating tumor cell isolation and diagnostics: toward routine clinical use. Cancer research. 2011;71:5955-60.

[11] Pantel K, Alix-Panabières C. Circulating tumour cells in cancer patients: challenges and perspectives. Trends in Molecular Medicine. 2010;16:398-406.

[12] Gorges TM, Tinhofer I, Drosch M, Röse L, Zollner TM, Krahn T, et al. Circulating tumour cells escape from EpCAM-based detection due to epithelial-to-mesenchymal transition. BMC cancer. 2012;12:178.

[13] Osta WA, Chen Y, Mikhitarian K, Mitas M, Salem M, Hannun YA, et al. EpCAM is overexpressed in breast cancer and is a potential target for breast cancer gene therapy. Cancer research. 2004;64:5818-24.

[14] Hanahan D, Weinberg RA. Hallmarks of cancer: the next generation. Cell. 2011;144:646-74.

[15] Aktas B, Tewes M, Fehm T, Hauch S, Kimmig R, Kasimir-Bauer S. Stem cell and epithelial-mesenchymal transition markers are frequently overexpressed in circulating tumor cells of metastatic breast cancer patients. Breast cancer res. 2009;11:R46.

[16] Krohn A, Ahrens T, Yalcin A, Plönes T, Wehrle J, Taromi S, et al. Tumor Cell Heterogeneity in Small Cell Lung Cancer (SCLC): Phenotypical and Functional Differences Associated with Epithelial-Mesenchymal Transition (EMT) and DNA Methylation Changes. PloS one. 2014;9:e100249.

[17] Bonnomet A, Brysse A, Tachsidis A, Waltham M, Thompson EW, Polette M, et al. Epithelial-to-mesenchymal transitions and circulating tumor cells. Journal of mammary gland biology and neoplasia. 2010;15:261-73.

[18] Yang J, Weinberg RA. Epithelial-mesenchymal transition: at the crossroads of development and tumor metastasis. Developmental cell. 2008;14:818-29.

[19] Hanahan D, Weinberg RA. The hallmarks of cancer. Cell. 2000;100:57-70.

[20] Mantovani A, Allavena P, Sica A, Balkwill F. Cancer-related inflammation. Nature. 2008;454:436-44.

[21] Lin W-W, Karin M. A cytokine-mediated link between innate immunity, inflammation, and cancer. The Journal of clinical investigation. 2007;117:1175-83.

[22] Karnoub AE, Dash AB, Vo AP, Sullivan A, Brooks MW, Bell GW, et al. Mesenchymal stem cells within tumour stroma promote breast cancer metastasis. Nature. 2007;449:557-63.

[23] Strutz F, Zeisberg M, Ziyadeh FN, Yang C-Q, Kalluri R, Müller GA, et al. Role of basic fibroblast growth factor-2 in epithelial-mesenchymal transformation. Kidney international. 2002;61:1714-28.

[24] Xu J, Lamouille S, Derynck R. TGF-β-induced epithelial to mesenchymal transition. Cell research. 2009;19:156-72.

[25] Peinado H, Olmeda D, Cano A. Snail, Zeb and bHLH factors in tumour progression: an alliance against the epithelial phenotype? Nature Reviews Cancer. 2007;7:415-28.

[26] Polyak K, Weinberg RA. Transitions between epithelial and mesenchymal states: acquisition of malignant and stem cell traits. Nature Reviews Cancer. 2009;9:265-73.

[27] Thiery JP, Acloque H, Huang RY, Nieto MA. Epithelial-mesenchymal transitions in development and disease. Cell. 2009;139:871-90.

[28] Yilmaz M, Christofori G. EMT, the cytoskeleton, and cancer cell invasion. Cancer and Metastasis Reviews. 2009;28:15-33.

[29] Hermann PC, Huber SL, Herrler T, Aicher A, Ellwart JW, Guba M, et al. Distinct populations of cancer stem cells determine tumor growth and metastatic activity in human pancreatic cancer. Cell Stem Cell. 2007;1:313-23.

[30] Brabletz T, Jung A, Reu S, Porzner M, Hlubek F, Kunz-Schughart LA, et al. Variable β-catenin expression in colorectal cancers indicates tumor progression driven by the tumor environment. Proceedings of the National Academy of Sciences. 2001;98:10356-61.

[31] Yu M, Bardia A, Wittner BS, Stott SL, Smas ME, Ting DT, et al. Circulating breast tumor cells exhibit dynamic changes in epithelial and mesenchymal composition. Science. 2013;339:580-4.

[32] Hanash SM, Baik CS, Kallioniemi O. Emerging molecular biomarkers—blood-based strategies to detect and monitor cancer. Nature reviews Clinical oncology. 2011;8:142-50.

[33] Alix-Panabières C, Pantel K. Circulating tumor cells: liquid biopsy of cancer. Clinical chemistry. 2013;59:110-8.

[34] Yu M, Stott S, Toner M, Maheswaran S, Haber DA. Circulating tumor cells: approaches to isolation and characterization. Journal of Cell Biology. 2011;192:373-82.

[35] Hyun K-A, Jung H-I. Advances and critical concerns with the microfluidic enrichments of circulating tumor cells. Lab on a chip. 2014;14:45-56.

[36] Zheng S, Lin HK, Lu B, Williams A, Datar R, Cote RJ, et al. 3D microfilter device for viable circulating tumor cell (CTC) enrichment from blood. Biomedical microdevices. 2011;13:203-13.

[37] Tchikov V, Fritsch J, Kabelitz D, Schuetze S. Immunomagnetic Isolation of Subcellular Compartments. In: Kabelitz DKSHE, editor. Immunology of Infection, Third Edition2010. p. 21-33.

[38] Chalmers JJ, Xiong Y, Jin X, Shao M, Tong X, Farag S, et al. Quantification of Non-Specific Binding of Magnetic Micro- and Nanoparticles Using Cell Tracking Velocimetry: Implication for Magnetic Cell Separation and Detection. Biotechnology and Bioengineering. 2010;105:1078-93.

[39] Zborowski M, Chamers JJ. Rare Cell Separation and Analysis by Magnetic Sorting. Analytical Chemistry. 2011;83:8050-6.

[40] Virgo PF, Gibbs GJ. Flow cytometry in clinical pathology. Annals of Clinical Biochemistry. 2012;49:17-28.

[41] Geens M, de Velde HV, De Block G, Goossens E, Van Steirteghem A, Tournaye H. The efficiency of magnetic-activated cell sorting and fluorescence-activated cell sorting in the decontamination of testicular cell suspensions in cancer patients. Human Reproduction. 2007;22:733-42.

[42] Golden JP, Justin GA, Nasir M, Ligler FS. Hydrodynamic focusing-a versatile tool. Analytical and Bioanalytical Chemistry. 2012;402:325-35.

[43] Stott SL, Hsu CH, Tsukrov DI, Yu M, Miyamoto DT, Waltman BA, et al. Isolation of circulating tumor cells using a microvortex-generating herringbone-chip. Proceedings of the National Academy of Sciences of the United States of America. 2010;107:18392-7.

[44] Stott SL, Lee RJ, Nagrath S, Yu M, Miyamoto DT, Ulkus L, et al. Isolation and characterization of circulating tumor cells from patients with localized and metastatic prostate cancer. Science translational medicine. 2010;2:25ra3-ra3.

[45] Nagrath S, Sequist LV, Maheswaran S, Bell DW, Irimia D, Ulkus L, et al. Isolation of rare circulating tumour cells in cancer patients by microchip technology. Nature. 2007;450:1235-U10.

[46] Ozkumur E, Shah AM, Ciciliano JC, Emmink BL, Miyamoto DT, Brachtel E, et al. Inertial focusing for tumor antigen–dependent and–independent sorting of rare circulating tumor cells. Science translational medicine. 2013;5:179ra47-ra47.

[47] Aigner K, Dampier B, Descovich L, Mikula M, Sultan A, Schreiber M, et al. The transcription factor ZEB1 (δEF1) promotes tumour cell dedifferentiation by repressing master regulators of epithelial polarity. Oncogene. 2007;26:6979-88.

[48] Tokarev I, Minko S. Stimuli-responsive hydrogel thin films. Soft Matter. 2009;5:511-24.

[49] Klouda L, Mikos AG. Thermoresponsive hydrogels in biomedical applications. European Journal of Pharmaceutics and Biopharmaceutics. 2008;68:34-45.

[50] Santos E, Luis Pedraz J, Maria Hernandez R, Orive G. Therapeutic cell encapsulation: Ten steps towards clinical translation. Journal of Controlled Release. 2013;170:1-14.

[51] Uludag H, De Vos P, Tresco PA. Technology of mammalian cell encapsulation. Advanced Drug Delivery Reviews. 2000;42:29-64.

[52] Jagur-Grodzinski J. Polymeric gels and hydrogels for biomedical and pharmaceutical applications. Polymers for Advanced Technologies. 2010;21:27-47.

[53] Drury JL, Mooney DJ. Hydrogels for tissue engineering: scaffold design variables and applications. Biomaterials. 2003;24:4337-51.

[54] Cruise GM, Hegre OD, Lamberti FV, Hager SR, Hill R, Scharp DS, et al. In vitro and in vivo performance of porcine islets encapsulated in interfacially photopolymerized poly(ethylene glycol) diacrylate membranes. Cell Transplantation. 1999;8:293-306.

[55] Brandl F, Sommer F, Goepferich A. Rational design of hydrogels for tissue engineering: impact of physical factors on cell behavior. Biomaterials. 2007;28:134-46.

[56] Seidlits SK, Khaing ZZ, Petersen RR, Nickels JD, Vanscoy JE, Shear JB, et al. The effects of hyaluronic acid hydrogels with tunable mechanical properties on neural progenitor cell differentiation. Biomaterials. 2010;31:3930-40.

[57] Chen K, Merkel TJ, Pandya A, Napier ME, Luft JC, Daniel W, et al. Low modulus biomimetic microgel particles with high loading of hemoglobin. Biomacromolecules. 2012;13:2748-59.

[58] Merkel TJ, Jones SW, Herlihy KP, Kersey FR, Shields AR, Napier M, et al. Using mechanobiological mimicry of red blood cells to extend circulation times of hydrogel microparticles. Proceedings of the National Academy of Sciences. 2011;108:586-91.

[59] Bao G, Suresh S. Cell and molecular mechanics of biological materials. Nature Materials. 2003;2:715-25.

[60] Cruise GM, Scharp DS, Hubbell JA. Characterization of permeability and network structure of interfacially photopolymerized poly(ethylene glycol) diacrylate hydrogels. Biomaterials. 1998;19:1287-94.

[61] Kapur V, Charkoudian JC, Kessler SB, Anderson JL. Hydrodynamic permeability of hydrogels stabilized within porous membranes. Industrial & engineering chemistry research. 1996;35:3179-85.

[62] Weber LM, Lopez CG, Anseth KS. Effects of PEG hydrogel crosslinking density on protein diffusion and encapsulated islet survival and function. Journal of Biomedical Materials Research Part A. 2009;90:720-9.

[63] Reinhart CT, Peppas NA. Solute diffusion in swollen membranes. Part II. Influence of crosslinking on diffusive properties. Journal of membrane Science. 1984;18:227-39.

[64] Peppas NA, Reinhart CT. Solute diffusion in swollen membranes. Part I. A new theory. Journal of membrane Science. 1983;15:275-87.

[65] Nafea E, Marson A, Poole-Warren L, Martens P. Immunoisolating semi-permeable membranes for cell encapsulation: focus on hydrogels. Journal of Controlled Release. 2011;154:110-22.

[66] Nicodemus GD, Bryant SJ. Cell encapsulation in biodegradable hydrogels for tissue engineering applications. Tissue Engineering Part B-Reviews. 2008;14:149-65.

[67] Hong Y, Song H, Gong Y, Mao Z, Gao C, Shen J. Covalently crosslinked chitosan hydrogel: properties of in vitro degradation and chondrocyte encapsulation. Acta Biomaterialia. 2007;3:23-31.

[68] Yeo Y, Geng W, Ito T, Kohane DS, Burdick JA, Radisic M. Photocrosslinkable hydrogel for myocyte cell culture and injection. Journal of Biomedical Materials Research Part B: Applied Biomaterials. 2007;81:312-22.

[69] Kim J, Kim IS, Cho TH, Lee KB, Hwang SJ, Tae G, et al. Bone regeneration using hyaluronic acid-based hydrogel with bone morphogenic protein-2 and human mesenchymal stem cells. Biomaterials. 2007;28:1830-7.

[70] Nguyen KT, West JL. Photopolymerizable hydrogels for tissue engineering applications. Biomaterials. 2002;23:4307-14.

[71] Branch DW, Wheeler BC, Brewer GJ, Leckband DE. Long-term stability of grafted polyethylene glycol surfaces for use with microstamped substrates in neuronal cell culture. Biomaterials. 2001;22:1035-47.

[72] Lim GJ, Zare S, Van Dyke M, Atala A. Cell microencapsulation. Therapeutic Applications of Cell Microencapsulation: Springer; 2010. p. 126-36.

[73] Karoubi G, Ormiston ML, Stewart DJ, Courtman DW. Single-cell hydrogel encapsulation for enhanced survival of human marrow stromal cells. Biomaterials. 2009;30:5445-55.

[74] Murua A, Portero A, Orive G, Hernández RM, de Castro M, Pedraz JL. Cell microencapsulation technology: towards clinical application. Journal of Controlled Release. 2008;132:76-83.

[75] Canaple L, Rehor A, Hunkeler D. Improving cell encapsulation through size control. Journal of Biomaterials Science, Polymer Edition. 2002;13:783-96.

[76] Mumaw J, Jordan ET, Sonnet C, Olabisi RM, Olmsted-Davis EA, Davis AR, et al. Rapid heterotrophic ossification with cryopreserved poly (ethylene glycol-) microencapsulated BMP2-expressing MSCs. International journal of biomaterials. 2012;2012.

[77] Koh W-G, Revzin A, Pishko MV. Poly (ethylene glycol) hydrogel microstructures encapsulating living cells. Langmuir : the ACS journal of surfaces and colloids. 2002;18:2459-62.

[78] Chabert M, Viovy J-L. Microfluidic high-throughput encapsulation and hydrodynamic self-sorting of single cells. Proceedings of the National Academy of Sciences. 2008;105:3191-6.

[79] Khademhosseini A, Langer R. Microengineered hydrogels for tissue engineering. Biomaterials. 2007;28:5087-92.

[80] Cruise GM, Hegre OD, Scharp DS, Hubbell JA. A sensitivity study of the key parameters in the interfacial photopolymerization of poly(ethylene glycol) diacrylate upon porcine islets. Biotechnology and Bioengineering. 1998;57:655-65.

[81] Fairbanks BD, Schwartz MP, Bowman CN, Anseth KS. Photoinitiated polymerization of PEG-diacrylate with lithium phenyl-2, 4, 6-trimethylbenzoylphosphinate: polymerization rate and cytocompatibility. Biomaterials. 2009;30:6702-7.

[82] Fisher JP, Dean D, Engel PS, Mikos AG. Photoinitiated polymerization of biomaterials. Annual review of materials research. 2001;31:171-81.

[83] Fouassier J, Allonas X, Burget D. Photopolymerization reactions under visible lights: principle, mechanisms and examples of applications. Progress in Organic Coatings. 2003;47:16-36.

[84] Williams CG, Malik AN, Kim TK, Manson PN, Elisseeff JH. Variable cytocompatibility of six cell lines with photoinitiators used for polymerizing hydrogels and cell encapsulation. Biomaterials. 2005;26:1211-8.

[85] Kizilel S, Perez-Luna VH, Teymour F. Photopolymerization of poly(ethylene glycol) diacrylate on eosin-functionalized surfaces. Langmuir : the ACS journal of surfaces and colloids. 2004;20:8652-8.

[86] Avens HJ, Bowman CN. Mechanism of Cyclic Dye Regeneration During Eosin-Sensitized Photoinitiation in the Presence of Polymerization Inhibitors. Journal of Polymer Science Part a-Polymer Chemistry. 2009;47:6083-94.

[87] Encinas M, Rufs A, Bertolotti S, Previtali C. Xanthene dyes/amine as photoinitiators of radical polymerization: A comparative and photochemical study in aqueous medium. Polymer. 2009;50:2762-7.

[88] Bahney C, Lujan TJ, Hsu C, Bottlang M, West J, Johnstone B. Visible light photoinitiation of mesenchymal stem cell-laden bioresponsive hydrogels. Eur Cell Mater. 2011;22:43-55.

[89] Cruise GM, Hegre OD, Hager S, Hill R, Scharp D, Hubbell JP. Poly(ethylene glycol) based encapsulation of islets of Langerhans. Cell Transplantation. 1996;5:52-.

[90] Shih H, Lin C-C. Visible-Light-Mediated Thiol-Ene Hydrogelation Using Eosin-Y as the Only Photoinitiator. Macromolecular Rapid Communications. 2013;34:269-73.

[91] Kizilel S, Sawardecker E, Teymour F, Perez-Luna VH. Sequential formation of covalently bonded hydrogel multilayers through surface initiated photopolymerization. Biomaterials. 2006;27:1209-15.

[92] Avens HJ, Randle TJ, Bowman CN. Polymerization behavior and polymer properties of eosin-mediated surface modification reactions. Polymer. 2008;49:4762-8.

[93] Kızılel S, Pérez-Luna VH, Teymour F. Mathematical Model for Surface-Initiated Photopolymerization of Poly (ethylene glycol) Diacrylate. Macromolecular Theory and Simulations. 2006;15:686-700.

[94] Johnson LM, Avens HJ, Hansen RR, Sewell HL, Bowman CN. Characterization of the Assaying Methods in Polymerization-Based Amplification of Surface Biomarkers. Australian Journal of Chemistry. 2009;62:877-84.

[95] Avens HJ, Bowman CN. Development of fluorescent polymerization-based signal amplification for sensitive and non-enzymatic biodetection in antibody microarrays. Acta Biomaterialia. 2010;6:83-9.

[96] Sikes HD, Hansen RR, Johnson LM, Jenison R, Birks JW, Rowlen KL, et al. Using polymeric materials to generate an amplified response to molecular recognition events. Nat Mater. 2008;7:52-6.

[97] Avens HJ, Chang EL, May AM, Berron BJ, Seedorf GJ, Balasubramaniam V, et al. Fluorescent polymeric nanocomposite films generated by surface-mediated photoinitiation of polymerization. Journal of Nanoparticle Research. 2011;13:331-46.

[98] Hansen RR, Sikes HD, Bowman CN. Visual detection of labeled oligonucleotides using visible-light-polymerization-based amplification. Biomacromolecules. 2007;9:355-62.

[99] Hansen RR, Johnson LM, Bowman CN. Visual, base-specific detection of nucleic acid hybridization using polymerization-based amplification. Anal Biochem. 2009;386:285-7.

[100] Avens HJ, Berron BJ, May AM, Voigt KR, Seedorf GJ, Balasubramaniam V, et al. Sensitive Immunofluorescent Staining of Cells via Generation of Fluorescent Nanoscale Polymer Films in Response to Biorecognition. J Histochem Cytochem. 2011;59:76-87.

[101] Hamidi M, Azadi A, Rafiei P. Hydrogel nanoparticles in drug delivery. Advanced Drug Delivery Reviews. 2008;60:1638-49.

[102] Lin CC, Anseth KS. PEG Hydrogels for the Controlled Release of Biomolecules in Regenerative Medicine. Pharmaceutical Research. 2009;26:631-43.

[103] Fedorovich NE, Alblas J, de Wijn JR, Hennink WE, Verbout AJ, Dhert WJA. Hydrogels as extracellular matrices for skeletal tissue engineering: state-of-the-art and novel application in organ printing. Tissue Engineering. 2007;13:1905-25.

[104] Avens HJ, Berron BJ, May AM, Voigt KR, Seedorf GJ, Balasubramaniam V, et al. Sensitive immunofluorescent staining of cells via generation of fluorescent nanoscale polymer films in response to biorecognition. The journal of histochemistry and cytochemistry : official journal of the Histochemistry Society. 2011;59:76-87.

[105] Kizilel S, Perez-Luna VH, Teymour F. Modeling of PEG Hydrogel Membranes for Biomedical Applications. Macromolecular Reaction Engineering. 2009;3:271-87.

[106] Mohr D, Frey S, Fischer T, Guttler T, Gorlich D. Characterisation of the passive permeability barrier of nuclear pore complexes. Embo Journal. 2009;28:2541-53.

[107] Baroli B. Photopolymerization of biomaterials: issues and potentialities in drug delivery, tissue engineering, and cell encapsulation applications. Journal of Chemical Technology and Biotechnology. 2006;81:491-9.

[108] Bryant SJ, Nuttelman CR, Anseth KS. Cytocompatibility of UV and visible light photoinitiating systems on cultured NIH/3T3 fibroblasts in vitro. Journal of Biomaterials Science-Polymer Edition. 2000;11:439-57.

[109] Romero G, Estrela-Lopis I, Zhou J, Rojas E, Franco A, Espinel CS, et al. Surface Engineered Poly (lactide-co-glycolide) Nanoparticles for Intracellular Delivery: Uptake and Cytotoxicity・ A Confocal Raman Microscopic Study. Biomacromolecules. 2010;11:2993-9.

[110] Schmid-Schonbein G, Shih YY, Chien S. Morphometry of human leukocytes. Blood. 1980;56:866-75.

[111] Browning M, Cereceres S, Luong P, Cosgriff-Hernandez E. Determination of the in vivo degradation mechanism of PEGDA hydrogels. Journal of Biomedical Materials Research Part A. 2014.

[112] Naim B, Brumfeld V, Kapon R, Kiss V, Nevo R, Reich Z. Passive and facilitated transport in nuclear pore complexes is largely uncoupled. Journal of Biological Chemistry. 2007;282:3881-8.

[113] Adam SA, Sternemarr R, Gerace L. NUCLEAR-PROTEIN IMPORT USING DIGITONIN-PERMEABILIZED CELLS. Methods in Enzymology. 1992;219:97-110.

[114] Armstrong J, Wenby R, Meiselman H, Fisher T. The hydrodynamic radii of macromolecules and their effect on red blood cell aggregation. Biophysical journal. 2004;87:4259-70.

[115] Shenoy R, Bowman CN. A Comprehensive Kinetic Model of Free-Radical-Mediated Interfacial Polymerization. Macromolecular Theory and Simulations. 2013;22:115-26.

[116] Cuchiara MP, Allen AC, Chen TM, Miller JS, West JL. Multilayer microfluidic PEGDA hydrogels. Biomaterials. 2010;31:5491-7.

[117] Canal T, Peppas NA. Correlation between mesh size and equilibrium degree of swelling of polymeric networks. Journal of Biomedical Materials Research. 1989;23:1183-93.

[118] Chatterjee A, Moulik S, Sanyal S, Mishra B, Puri P. Thermodynamics of micelle formation of ionic surfactants: a critical assessment for sodium dodecyl sulfate, cetyl pyridinium chloride and dioctyl sulfosuccinate (Na salt) by microcalorimetric, conductometric, and tensiometric measurements. The Journal of Physical Chemistry B. 2001;105:12823-31.

[119] Cohen SJ, Punt CJ, Iannotti N, Saidman BH, Sabbath KD, Gabrail NY, et al. Relationship of circulating tumor cells to tumor response, progression-free survival, and overall survival in patients with metastatic colorectal cancer. Journal of clinical oncology. 2008;26:3213-21.

[120] Arnold LW, Lannigan J. Practical Issues in High-Speed Cell Sorting. Current Protocols in Cytometry. 2010:1.24. 1-1.. 30.

[121] Stott SL, Hsu C-H, Tsukrov DI, Yu M, Miyamoto DT, Waltman BA, et al. Isolation of circulating tumor cells using a microvortex-generating herringbone-chip. Proc Natl Acad Sci U S A. 2010;107:18392-7.

[122] Shah AM, Yu M, Nakamura Z, Ciciliano J, Ulman M, Kotz K, et al. Biopolymer System for Cell Recovery from Microfluidic Cell Capture Devices. Analytical Chemistry. 2012;84:3682-8.

[123] Kloxin AM, Kasko AM, Salinas CN, Anseth KS. Photodegradable Hydrogels for Dynamic Tuning of Physical and Chemical Properties. Science. 2009;324.

[124] Berron BJ, May AM, Zheng Z, Balasubramaniam V, Bowman CN. Antigen-Responsive, Microfluidic Valves for Single Use Diagnostics. Lab Chip. 2012;12:708-10.

[125] Lilly JL, Sheldon PR, Hoversten LJ, Romero G, Balasubramaniam V, Berron BJ. Interfacial Polymerization for Colorimetric Labeling of Protein Expression in Cells. PLoS ONE. 2014;9:e115630.

[126] Lilly JL, Romero G, Xu W, Shin HY, Berron BJ. Characterization of Molecular Transport in Ultrathin Hydrogel Coatings for Cellular Immunoprotection. Biomacromolecules. 2015;16:541-9.

[127] Brown RB, Audet J. Journal of the Royal Society Interface2008.

[128] Griffin DR, Kasko AM. Photodegradable Macromers and Hydrogels for Live Cell Encapsulation and Release. Journal of the American Chemical Society. 2012;134:13103-7.

[129] DeForest CA, Anseth KS. Cytocompatible click-based hydrogels with dynamically tunable properties through orthogonal photoconjugation and photocleavage reactions. Nat Chem. 2011;3:925-31.

[130] Ki CS, Lin T-Y, Korc M, Lin C-C. Thiol-ene hydrogels as desmoplasia-mimetic matrices for modeling pancreatic cancer cell growth, invasion, and drug resistance. Biomaterials. 2014;35:9668-77.

[131] Lin C-C, Anseth KS. Cell–cell communication mimicry with poly(ethylene glycol) hydrogels for enhancing β-cell function. Proceedings of the National Academy of Sciences. 2011;108:6380-5.

[132] Harrison RG, Todd P, Rudge SR, Petrides DP. Bioseparations Science and Engineering. Oxford University Press New York. 2003.

[133] Barzilai A, Yamamoto K-I. DNA damage responses to oxidative stress. DNA Repair. 2004;3:1109-15.

[134] Martin OA, Pilch DR, Redon C, Bonner WM. Involvement of H2AX in the DNA Damage and Repair Response. Cancer Biology & Therapy. 2003;2:233-5.

[135] Rogakou EP, Pilch DR, Orr AH, Ivanova VS, Bonner WM. DNA Double-stranded Breaks Induce Histone H2AX Phosphorylation on Serine 139. Journal of Biological Chemistry. 1998;273:5858-68.

[136] Hansen R, Avens H, Shenoy R, Bowman C. Quantitative evaluation of oligonucleotide surface concentrations using polymerization-based amplification. Analytical and Bioanalytical Chemistry. 2008;392:167-75.

[137] Asahara T, Murohara T, Sullivan A, Silver M, van der Zee R, Li T, et al. Isolation of Putative Progenitor Endothelial Cells for Angiogenesis. Science. 1997;275:964-6.

[138] Lee J-H, Bhang Dong H, Beede A, Huang Tian L, Stripp Barry R, Bloch Kenneth D, et al. Lung Stem Cell Differentiation in Mice Directed by Endothelial Cells via a BMP4-NFATc1-Thrombospondin-1 Axis. Cell. 2014;156:440-55.

[139] Warkiani ME, Guan G, Luan KB, Lee WC, Bhagat AAS, Kant Chaudhuri P, et al. Slanted spiral microfluidics for the ultra-fast, label-free isolation of circulating tumor cells. Lab on a Chip. 2014;14:128-37.

[140] Hou HW, Warkiani ME, Khoo BL, Li ZR, Soo RA, Tan DS-W, et al. Isolation and retrieval of circulating tumor cells using centrifugal forces. Sci Rep. 2013;3.

[141] Lee JK, Heimer BW, Sikes HD. Systematic Study of Fluorescein-Functionalized Macrophotoinitiators for Colorimetric Bioassays. Biomacromolecules. 2012;13:1136-43.

[142] Gan SD, Patel KR. Enzyme immunoassay and enzyme-linked immunosorbent assay. Journal of Investigative Dermatology. 2013;133:e12.

[143] Paulie S, Perlmann H, Perlmann P. Enzyme-linked Immunosorbent Assay. eLS. 2003.

[144] Konecny G, Pauletti G, Pegram M, Untch M, Dandekar S, Aguilar Z, et al. Quantitative association between HER-2/neu and steroid hormone receptors in hormone receptor-positive primary breast cancer. Journal of the National Cancer Institute. 2003;95:142-53.

[145] McCabe A, Dolled-Filhart M, Camp RL, Rimm DL. Automated quantitative analysis (AQUA) of in situ protein expression, antibody concentration, and prognosis. Journal of the National Cancer Institute. 2005;97:1808-15.

[146] Dewitt S, Hallett M. Leukocyte membrane "expansion": a central mechanism for leukocyte extravasation. Journal of leukocyte biology. 2007;81:1160-4.

[147] Chavez KJ, Garimella SV, Lipkowitz S. Triple negative breast cancer cell lines: one tool in the search for better treatment of triple negative breast cancer. Breast disease. 2010;32:35-48.

[148] Holliday DL, Speirs V. Choosing the right cell line for breast cancer research.

[149] Livasy CA, Karaca G, Nanda R, Tretiakova MS, Olopade OI, Moore DT, et al. Phenotypic evaluation of the basal-like subtype of invasive breast carcinoma. Modern Pathology. 2006;19:264-71.

[150] Liu S, Li N, Yu X, Xiao X, Cheng K, Hu J, et al. Expression of intercellular adhesion molecule 1 by hepatocellular carcinoma stem cells and circulating tumor cells. Gastroenterology. 2013;144:1031-41. e10.

[151] Maheswaran S, Sequist LV, Nagrath S, Ulkus L, Brannigan B, Collura CV, et al. Detection of mutations in EGFR in circulating lung-cancer cells. New England Journal of Medicine. 2008;359:366-77.

[152] Lecharpentier A, Vielh P, Perez-Moreno P, Planchard D, Soria J, Farace F. Detection of circulating tumour cells with a hybrid (epithelial/mesenchymal) phenotype in patients with metastatic non-small cell lung cancer. British Journal of Cancer. 2011;105:1338-41.

[153] Ali S, Coombes RC. Estrogen receptor alpha in human breast cancer: occurrence and significance. Journal of mammary gland biology and neoplasia. 2000;5:271-81.

[154] Thiery JP, Lim CT. Tumor dissemination: an EMT affair. Cancer cell. 2013;23:272-3.

[155] Jin H, Varner J. Integrins: roles in cancer development and as treatment targets. British Journal of Cancer. 2004;90:561-5.

[156] Yang J, Huang Y, Wang X, Wang X-B, Becker FF, Gascoyne PR. Dielectric properties of human leukocyte subpopulations determined by electrorotation as a cell separation criterion. Biophysical journal. 1999;76:3307-14.

[157] Evans E, Yeung A. Apparent viscosity and cortical tension of blood granulocytes determined by micropipet aspiration. Biophysical journal. 1989;56:151.

[158] Kawata M, Koinuma D, Ogami T, Umezawa K, Iwata C, Watabe T, et al. TGF-β-induced epithelial-mesenchymal transition of A549 lung adenocarcinoma cells is

enhanced by pro-inflammatory cytokines derived from RAW 264.7 macrophage cells. Journal of biochemistry. 2012;151:205-16.

[159] Liu X. Inflammatory cytokines augments TGF-β1-induced epithelial-mesenchymal transition in A549 cells by up-regulating TβR-I. Cell motility and the cytoskeleton. 2008;65:935-44.

[160] Sun J-J, Zhou X-D, Liu Y-K, Tang Z-Y, Feng J-X, Zhou G, et al. Invasion and metastasis of liver cancer: expression of intercellular adhesion molecule 1. Journal of cancer research and clinical oncology. 1999;125:28-34.

[161] Sununliganon L, Singhatanadgit W. Highly osteogenic PDL stem cell clones specifically express elevated levels of ICAM1, ITGB1 and TERT. Cytotechnology. 2012;64:53-63.

[162] Strakova Z, Livak M, Krezalek M, Ihnatovych I. Multipotent properties of myofibroblast cells derived from human placenta. Cell and tissue research. 2008;332:479-88.

[163] Lustberg MB, Balasubramanian P, Miller B, Garcia-Villa A, Deighan C, Wu Y, et al. Heterogeneous atypical cell populations are present in blood of metastatic breast cancer patients. Breast cancer res. 2014;16:R23.

[164] Joosse SA, Pantel K. Biologic challenges in the detection of circulating tumor cells. Cancer research. 2013;73:8-11.

[165] Muller V, Riethdorf S, Rack B, Janni W, Fasching PA, Solomayer E, et al. Prognostic impact of circulating tumor cells assessed with the CellSearch System and AdnaTest Breast in metastatic breast cancer patients: the DETECT study. Breast cancer res. 2012;14:R118.

[166] Mũnoz Z, Shih H, Lin C-C. Gelatin hydrogels formed by orthogonal thiol–norbornene photochemistry for cell encapsulation. Biomaterials Science. 2014;2:1063-72.

[167] Tomei AA, Manzoli V, Fraker CA, Giraldo J, Velluto D, Najjar M, et al. Device design and materials optimization of conformal coating for islets of Langerhans. Proceedings of the National Academy of Sciences. 2014;111:10514-9.

[168] Cheung CY, Anseth KS. Synthesis of immunoisolation barriers that provide localized immunosuppression for encapsulated pancreatic islets. Bioconjugate chemistry. 2006;17:1036-42.

[169] Lilly JL, Romero G, Xu W, Shin HY, Berron BJ. Characterization of Molecular Transport in Ultrathin Hydrogel Coatings for Cellular Immunoprotection. Biomacromolecules. 2015.

[170] Panda P, Ali S, Lo E, Chung BG, Hatton TA, Khademhosseini A, et al. Stop-flow lithography to generate cell-laden microgel particles. Lab on a chip. 2008;8:1056-61.

[171] Romero G, Lilly JJ, Abraham NS, Shin HY, Balasubramaniam V, Izumi T, et al. Protective Polymer Coatings for High-Throughput, High-Purity Cellular Isolation. Acs Applied Materials & Interfaces. 2015;7:17598-602.

[172] Cahall CF, Lilly JL, Hirschowitz EA, Berron BJ. A Quantitative Perspective on Surface Marker Selection for the Isolation of Functional Tumor Cells. Breast cancer: basic and clinical research. 2015;9:1.

[173] Lillemeier BF, Pfeiffer JR, Surviladze Z, Wilson BS, Davis MM. Plasma membrane-associated proteins are clustered into islands attached to the cytoskeleton. Proceedings of the National Academy of Sciences. 2006;103:18992-7.

[174] Adams JC. Biotin Amplification of Biotin and Horseradish-Peroxidase Signals in Histochemical Stains. J Histochem Cytochem. 1992;40:1457-63.

[175] Rojo MG, Bueno G, Slodkowska J. Review of imaging solutions for integrated quantitative immunohistochemistry in the Pathology daily practice. Folia Histochem Cyto. 2010;47:349-8.

[176] de Matos LL, Trufelli DC, de Matos MGL, da Silva Pinhal MA. Immunohistochemistry as an important tool in biomarkers detection and clinical practice. Biomarker insights. 2010;5:9.

[177] Wu YF, Liu SQ, He L. Electrochemical Biosensing Using Amplification-by-Polymerization. Analytical Chemistry. 2009;81:7015-21.

[178] Hansen RR, Sikes HB, Bowman CN. Visual detection of labeled oligonucleotides using visible-light-polymerization-based amplification. Biomacromolecules. 2008;9:355-62.

[179] Sikes HD, Jenison R, Bowman CN. Antigen detection using polymerization-based amplification. Lab Chip. 2009;9:653-6.

[180] Kaastrup K, Sikes HD. Polymerization-based signal amplification under ambient conditions with thirty-five second reaction times. Lab Chip. 2012;12:4055-8.

[181] Khire VS, Harant AW, Watkins AW, Anseth KS, Bowman CN. Ultrathin patterned polymer films on surfaces using thiol-ene polymerizations. Macromolecules. 2006;39:5081-6.

[182] Kaastrup K, Chan L, Sikes HD. Impact of Dissociation Constant on the Detection Sensitivity of Polymerization-Based Signal Amplification Reactions. Analytical Chemistry. 2013;85:8055-60.

[183] Singh I. Textbook of Human Histology:(with Colour Atlas & Practical Guide): JP Medical Ltd; 2011.

[184] Hansen RR, Avens HJ, Shenoy R, Bowman CN. Quantitative evaluation of oligonucleotide surface concentrations using polymerization-based amplification. Analytical and Bioanalytical Chemistry. 2008;392:167-75.

[185] Avens HJ, Bowman CN. Polymerization for signal amplification of antibody-based biodetection. Abstracts of Papers of the American Chemical Society. 2009;237.

[186] Berron BJ, Ba X, Johnson LM, Bowman CN. Glucose Oxidase Mediated Radical Chain Polymerization for Detection of Biorecognition Events in Microtiter Assays. Biotechnol Bioeng. 2011;108:1521-8.

[187] Lou XH, Lewis MS, Gorman CB, He L. Detection of DNA point mutation by atom transfer radical polymerization. Analytical Chemistry. 2005;77:4698-705.

[188] Okelo GO, He L. Cu(0) as the reaction additive in purge-free ATRP-assisted DNA detection. Biosensors & Bioelectronics. 2007;23:588-92.

[189] Qian H, He L. Detection of Protein Binding Using Activator Generated by Electron Transfer for Atom Transfer Radical Polymerization. Analytical Chemistry. 2009;81:9824-7.

[190] Qian H, He L. Surface-Initiated Activators Generated by Electron Transfer for Atom Transfer Radical Polymerization in Detection of DNA Point Mutation. Analytical Chemistry. 2009;81:4536-42.

[191] Moss L, Rueggeberg F, Stansbury J. Effect of solvent type on absorption profile of camphoroquinone. Journal of Dental Research. 2002;81.

[192] Woo HY, Liu B, Kohler B, Korystov D, Mikhailovsky A, Bazan GC. Solvent effects on the two-photon absorption of distyrylbenzene chromophores. Journal of the American Chemical Society. 2005;127:14721-9.

[193] Lakowicz JR. Effects of solvents on fluorescence emission spectra. Principles of Fluorescence Spectroscopy: Springer; 1983. p. 187-215.

Jacob Louis Lilly Vita

EDUCATION

B.S. Chemical Engineering, Purdue University, Dec 2010
Minor: Economics

RESEARCH EXPERIENCE

University of Kentucky, Chemical and Materials Engineering, Lexington, KY
Graduate Research Assistant, Nov 2011 – May 2016

FELLOWSHIPS

NCI Cancer Nanotechnology Training Center Traineeship , March 2014 – Nov 2015
Kentucky Opportunity Academic Fellowship, Aug 2012 – May 2013

PUBLICATIONS

Gabriela Romero, **Jacob Lilly**, Nathan S. Abraham, Hainsworth Y. Shin, Vivek Balasubramaniam, Tadahide Izumi, Brad J. Berron. Protective Polymer Coatings for High-Throughput, High-Purity Cellular Isolation. *ACS Applied Materials & Interfaces* **2015**.

Calvin F. Cahall*, **Jacob L. Lilly***, Edward Hirschowitz, Brad J. Berron. A Quantitative Perspective on Surface Marker Selection for the Isolation of Functional Tumor Cells. *Breast Cancer: Basic and Clinical Research* **2015**. (*co-first authors)

Jacob L. Lilly, Gabriela Romero, Weijie Xu, Hainsworth Y. Shin, Brad J. Berron. Characterization of Molecular Transport in Ultrathin Hydrogel Coatings for Cellular Immunoprotection. *Biomacromolecules* **2015**.

Jacob L. Lilly, Phillip R. Sheldon, Liv J. Hoversten, Gabriela Romero, Vivek Balasubramaniam, Brad J. Berron. Interfacial Polymerization for Colorimetric Labeling of Protein Expression in Cells and Tissue. *PLoS one* **2014**.

Jacob L. Lilly, Brad J. Berron. The Role of Surface Receptor Density in Surface-Initiated Polymerizations for Cancer Cell Isolation. *Langmuir,* **2016.**

Jacob L. Lilly, Mohamed Agoub, Calvin F Cahall, Brad J. Berron. Xanthene Photoinitiator Systems to Form Surface Initiated Hydrogel Films in Mammalian Cell Compatible Environments. *In preparation for submission in 2016.*

PRESENTATIONS

Jacob Lilly, Gabriela Romero Uribe, Vivek Balasubramaniam, Brad J. Berron. Hydrogel Coatings for Rapid Sorting of Circulating NSCLC cells. Society for Biomaterials Annual Conference, Charlotte, NC. April 2015.

Jacob Lilly, Gabriela Romero Uribe, Vivek Balasubramaniam, Brad J. Berron. Hydrogel Coatings for Sorting CTCs. Gordon Research Conference: Rare Cells in Circulation, South Hadley, MA. Aug 2014.

Jacob Lilly, Gabriela Romero Uribe, Vivek Balasubramaniam, Brad J. Berron. Hydrogel Coatings for Sorting Stem-like CTCs. Markey Cancer Center Research Day, Lexington, KY. May 2014.

Jacob Lilly, Gabriela Romero Uribe, Vivek Balasubramaniam, Brad J. Berron. Hydrogel Coatings for High-Speed Cell Sorting Applications for Cell-Based Therapies. Society for Biomaterials Annual Conference, Denver, CO. April 2014.

Jacob Lilly, Gabriela Romero Uribe, Weijie Xu, Naveed Bakh, Roberto Arreaza, Vivek Balasubramaniam, Brad J. Berron. Antigen Specific Lysis: High-Throughput, High-Purity Cell Sorting Through Polymer Design Applications for Cell-Based Therapies. AIChE Annual Conference, San Francisco, CA. Nov 2013.

Jacob Lilly, Roberto Arreaza, Gabriela Romero Uribe, Brad J Berron. Micropatterning Cell Surface-Initiated Polymer Patches for Guided Drug Delivery with Highly Controllable Release. Presented at CME Department Symposium Sept 2013.

Jacob Lilly, Nathan Abraham, Gabriela Romero Uribe, Brad J Berron. Polymer Based Amplification for Antigen-Specific Sorting an Cell-Based Therapy Applications. Presented at Vanderbilt University for a chemical engineering symposium June 2013.

Jacob Lilly, Weijie Xu, Naveed Bakh, Hainsworth Shin, Brad J Berron. Interfacial Photopolymerization to Encapsulate T Lymphocytes By Biorecognition of the CD45 Surface Marker. Presented at CME Department Symposium Sept 2012.

AWARDS

2015 Outstanding Graduate Student Award, Chemical and Materials Engineering, University of Kentucky

3rd Place, 2015 Bionanotechnology Graduate Student Award, AIChE National Conference, Salt Lake City, UT